A HYDRODYNAMIC MODEL FOR GULFPORT HARBOR AND SHIP CHANNELS

Contract Number MASG-R/EN-1

Grant Number NA81AA-D-00050

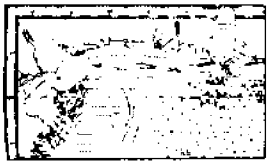

HYDRODYNAMICS OF MOBILE BAY AND MISSISSIPPI SOUND

by

Donald C. Raney
Professor of Engineering Mechanics

I. Huang
Post Doctoral Fellow

and

Hasan Urgun
Graduate Research Assistant

Prepared for
Mississippi-Alabama Sea Grant Consortium

April 1984

BER Report No. 295-183

MASGP-83-030

The University of Alabama
College of Engineering
Bureau of Engineering Research
P.O. Box 1968
University, Alabama 35486
Telephone: (205) 348-6400

MASGP-83-030

THE UNIVERSITY OF ALABAMA
COLLEGE OF ENGINEERING

The College of Engineering at The University of Alabama has an undergraduate enrollment of more than 2,300 students and a graduate enrollment exceeding 180. There are approximately 100 faculty members, a significant number of whom conduct research in addition to teaching.

Research is an integral part of the educational program, and research interests of the faculty parallel academic specialities. A wide variety of projects are included in the overall research effort of the College, and these projects form a solid base for the graduate program which offers fourteen different master's and five different doctor of philosophy degrees.

Other organizations on the University campus that contribute to particular research needs of the College of Engineering are the Charles L. Seebeck Computer Center, Geological Survey of Alabama, Marine Environmental Sciences Consortium, Mineral Resources Institute—State Mine Experiment Station, Mineral Resources Research Institute, Natural Resources Center, School of Mines and Energy Development, Tuscaloosa Metallurgy Research Center of the U.S. Bureau of Mines, and the Research Grants Committee.

This University community provides opportunities for interdisciplinary work in pursuit of the basic goals of teaching, research, and public service.

BUREAU OF ENGINEERING RESEARCH

The Bureau of Engineering Research (BER) is an integral part of the College of Engineering of The University of Alabama. The primary functions of the BER include: 1) identifying sources of funds and other outside support bases to encourage and promote the research and educational activities within the College of Engineering; 2) organizing and promoting the research interests and accomplishments of the engineering faculty and students; 3) assisting in the preparation, coordination, and execution of proposals, including research, equipment, and instructional proposals; 4) providing engineering faculty, students, and staff with services such as graphics and audiovisual support and typing and editing of proposals and scholarly works; 5) promoting faculty and staff development through travel and seed project support, incentive stipends, and publicity related to engineering faculty, students, and programs; 6) developing innovative methods by which the College of Engineering can increase its effectiveness in providing high quality educational opportunities for those with whom it has contact; and 7) providing a source of timely and accurate data that reflect the variety and depth of contributions made by the faculty, students, and staff of the College of Engineering to the overall success of the University in meeting its mission.

Through these activities, the BER serves as a unit dedicated to assisting the College of Engineering faculty by providing significant and quality service activities.

Contract Number MASG-R/ER-3

Grant Number NA81AA-D-00050

A HYDRODYNAMIC MODEL FOR GULFPORT HARBOR AND SHIP CHANNELS

by

Donald C. Raney
Professor of Engineering Mechanics

I. Huang
Post Doctoral Fellow

and

Hasan Urgun
Graduate Research Assistant

Prepared for

Mississippi-Alabama Sea Grant Consortium

April 1984

BER Report No. 295-183

TABLE OF CONTENTS

LIST OF SYMBOLS

C : Chezy frictional coefficient

c_0 : admittance coefficient

d : total water depth

d_H : depth of water over the crest of a barrier

f : Coriolis parameter

F_x, F_y : external forcing functions such as wind stress in the x and y directions

g : acceleration of gravity

h : still water elevation

k : time level

Q_n : normal component of transport

$\hat{R}$: rate at which additional water is introduced or taken from the system

t : time

u, v : vertically integrated velocities at time t in the x and y directions

x : axis of Cartesian coordinate system (north-south direction)

y : axis of Cartesian coordinate system (east-west direction)

Greek Letters:

Δx, Δy : vertical and horizontal spatial stepsize

δ_x, δ_y : centered difference operators

ε : generalized eddy viscosity coefficient

ε^* : minimum amount of water defining a dry cell or an exposed barrier

η : water surface elevation

η_a : hydrostatic elevation corresponding to atmospheric pressure

CHAPTER I

INTRODUCTION

1.1 General Background

During the last decade the field of numerical modeling has developed rapidly although it was virtually unknown before the 1950's. High speed, large memory digital computers have made possible the development of numerical models applicable to a wide range of disciplines. A general conference on numerical modeling will attract technical papers from the field of economics, agriculture, medicine, transportation, and others in addition to various scientific and engineering applications. Some of the earliest numerical modeling efforts were associated with weather forecasting and attempts to devise flood routing procedures for rivers.

Basically, a numerical model consists of a numerical algorithm which has been developed from equations describing the physical process. The method of formulation and the solution procedure for the model may vary widely. In engineering, a system of partial differential equations is normally required to describe the phenomenon being modeled. Two basic methods are in common usage for obtaining approximate numerical solutions; the finite difference and the finite element methods. Each of these methods starts

from identical governing equations and involve discretizing the system into small elements. However, the solution procedure differs significantly. In the finite difference procedure, variables and derivatives of variables are expressed directly in terms of nodal values at the individual cells. The finite difference equations for all cells in the system are solved subject to certain prescribed boundary conditions. In the finite element method variational principles are involved in transforming the differential equations for the finite element into finite element equations. Normally, this results in a global system of algebraic equations to be solved subject to appropriate boundary conditions.

The finite element method was originally developed by aircraft structural engineers in the 1950's to analyze large systems of structural elements in the aircraft. The finite difference method developed from work in fluid dynamics where the nonlinear governing equations are not very amenable to finite element analysis. This difference in approach has continued until the present; the finite element approach is used almost exclusively in solid mechanics applications and the finite difference approach predominates in the fluid mechanics area.

1.2 Hydrodynamic Modeling

Significant hydrodynamic modeling generally began in the mid-1960's with attempts at flood routing on rivers and with attempts to simulate flows in bays, estuaries, and

semi-enclosed seas. The early modeling efforts were complicated by computer hardware restrictions on the number of finite difference cells which could be considered. In addition, computer software development had not progressed to the point where many desired physical features could be represented satisfactorily.

Hydrodynamic systems are basically three-dimensional. The fluid motion is described by a system of four partial differential equations. The governing equations are the continuity equation derived from the conservation of mass principle and the Navier-Stokes equations derived from momentum principles. The hydrodynamic variables are the three components of velocity and the surface elevation. Because of difficulties associated with three-dimensional hydrodynamic models, researchers have devised a variety of numerical models of various degrees of simplification.

For many river applications, a one-dimensional formulation of the hydrodynamic equations may suffice. If the hydrodynamic variables of interest are surface elevation and flow rate then a model can be formulated with only the two dependent variables. The numerical model is based upon a system of two equations: the continuity equation and one momentum equation. This type model would have fewer finite difference cells and the operation costs would be relatively small. Of course, the river hydrodynamic problem can be formulated in two or three dimensions if information other than flow rate and surface elevation are of interest.

Tidal circulation in an estuary, harbor or bay can often be represented by a two-dimensional depth averaged model if the water body is unstratified. The vertical component of velocity for this situation is generally negligible and the hydrodynamic problem can be formulated in terms of the continuity equation and two momentum equations. The dependent variables are the water depth and two velocity components. The horizontal velocity components represent average values over the water depth. A two-dimensional grid of finite difference cells is used for this type model.

There are hydrodynamic flows which do not permit simplification to one or two-dimensional systems. For example, in most lakes there is little thruflow and the primary forcing function is wind. This leads to a situation where the fluid at the surface is moving generally in the same direction of the wind. However, there is a return flow which develops along the bottom of the lakes. The return flow is basically opposite in direction to the surface flow. The hydrodynamic variables change appreciably over the water depth and a three-dimensional finite difference array is required for the numerical model formulation.

1.3 Model Calibration and Verification

Numerical models must be calibrated and verified before they can be used with confidence as a predictive tool. The process of calibration consists of adjusting model parameters to bring the numerical model into agreement with actual measured prototype data. Once the model has been

calibrated these model parameters should not change significantly for generally similar operating conditions. Verification consists of applying the calibrated model for a second set of prototype data and demonstrating that the model correctly predicts the system behavior for this different set of boundary conditions. Once calibrated and verified, the model can be used to predict the system operating conditions for different sets of boundary conditions.

One of the difficulties associated with hydrodynamic modeling is the lack of availability of prototype data for model calibration and verification. Prototype data is very expensive to obtain and is often not available in the desired quality or quantity. The numerical modeler is often required to use models which have not been completely calibrated and verified. This should be done with great caution. Sound engineering judgement must be used in assessing the applicability of model results under these conditions.

CHAPTER II

OBJECTIVE

2.1 Problem Statement

Gulfport Harbor is a part of Mississippi Sound, formed by the barrier islands along the Mississippi-Alabama coastline. This is illustrated in Figures 1 and 2. There has been a great deal of industrial development in Mississippi Sound. A number of projects are planned or underway to improve harbor and navigation facilities in the region. Numerical models are generally applied to assess the environmental impact of proposed changes.

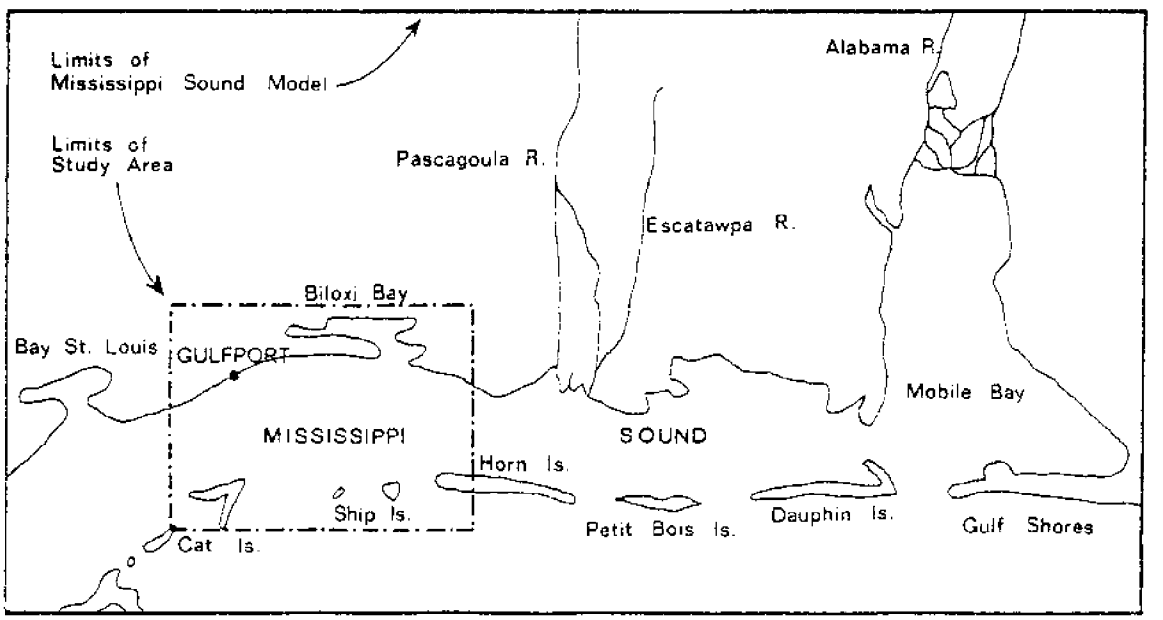

Figure 1. Areas Covered by Mississippi Sound Model and Gulfport Harbor Model

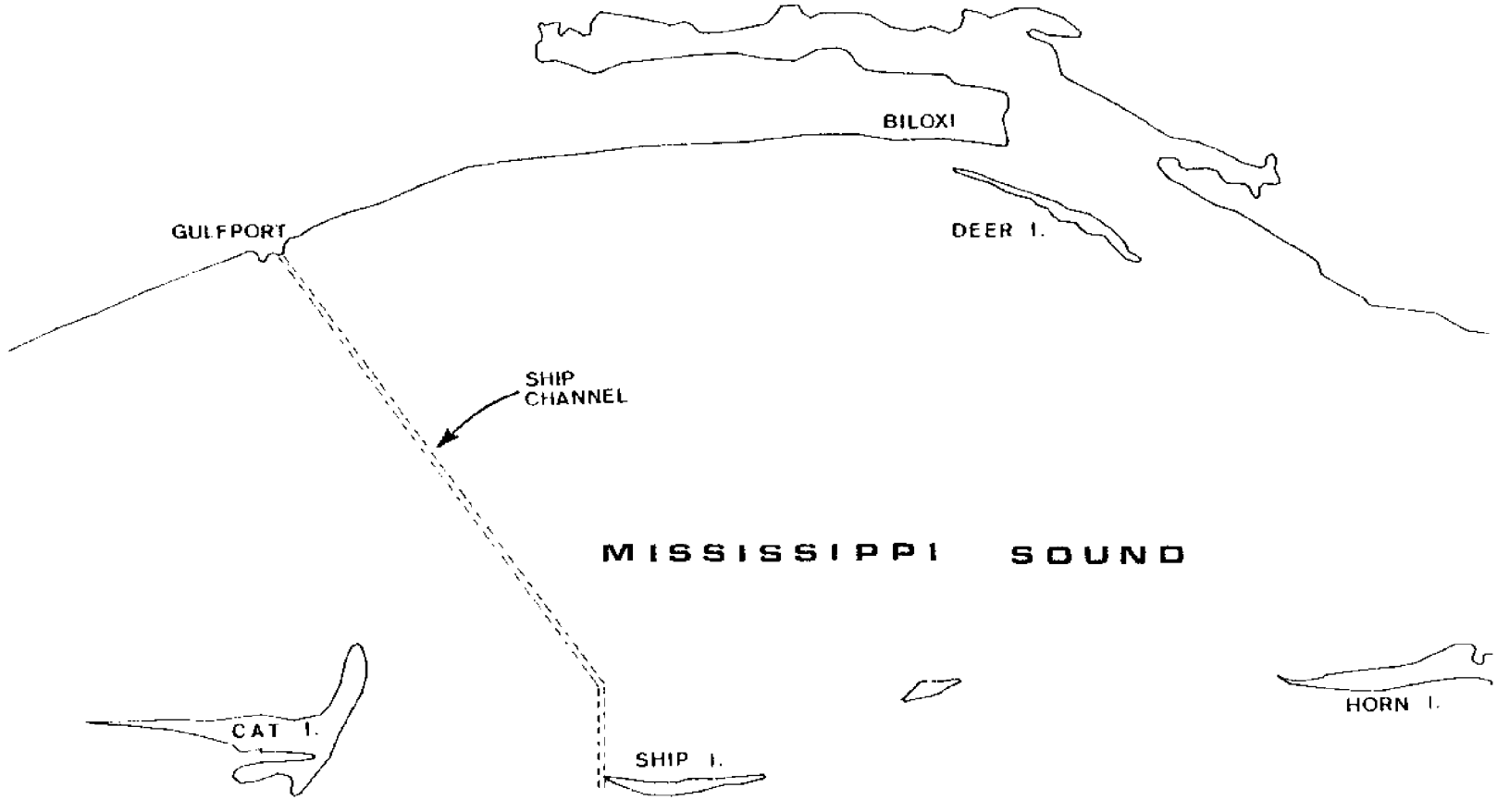

Figure 2. Gulfport Harbor and Ship Channels

The objective of this study was to develop a hydrodynamic model for investigating the hydrodynamics of Gulfport Harbor and Ship Channels when subjected to various meteorological and tidal conditions. The finite difference cells used in the model will be small enough to obtain the desired resolution of important hydrodynamic features of the region. The model will be calibrated using available prototype data and results from an earlier numerical model study of Mississippi Sound, conducted by the U. S. Army Corps of Engineers.

A properly designed and calibrated numerical model can be used to investigate alternative design proposals. In particular, the model can be used to investigate various dredge spoil disposal plans and various channel depths. Disposal areas can be selected where the hydrodynamics present the maximum potential for stable permanent disposal. Channel depths or configurations can be avoided which produce undesirable changes in circulation patterns.

2.2 Method of Approach

Mississippi Sound is generally shallow and relatively homogeneous. The velocity distribution is fairly constant over the water depth. These properties suggest that a two-dimensional depth averaged formulation of the hydrodynamic equations may be appropriate. The two-dimensional depth averaged hydrodynamic equations have been applied successfully to a variety of problems. Applications include: simulation of tidal circulation [2],

storm surge [3], open sea tsunami propagation [6,8], tsunami inundation [9], and landslide generated water waves [11,12].

A two-dimensional depth averaged finite difference model, WIFM, was selected as the basic numerical model. WIFM is a state-of-the-art model currently used by the U. S. Army Corps of Engineers (COE) for hydrodynamic modeling. The basic model has previously been used by the COE in an investigation of Mississippi Sound. Six months of prototype hydrodynamic and water quality data were taken in Mississippi Sound in connection with the previous study. The prototype data were used to calibrate and verify a numerical model for Mississippi Sound. The model was used to investigate overall circulation and salinity conditions in Mississippi Sound.

Sufficient prototype data were taken in Mississippi Sound by the COE to calibrate and verify an overall model of the region. Although adequate for the intended purpose, the Mississippi Sound model is not adequate for resolving detailed flows in a small restricted region of the Sound. Also, the density of prototype data collection points was not sufficient for calibration and verification of a numerical model for a small sub-region of Mississippi Sound.

For these reasons, the model for Gulfport Harbor and Ship Channels was developed as a sub-grid of the larger Mississippi Sound model. This is illustrated in Figure 1. The previously calibrated model for Mississippi Sound was used to establish boundary conditions for the smaller

sub-grid. In addition, a combination of prototype data and Mississippi Sound model results were used in calibration and verification of the Gulfport Harbor model.

CHAPTER III

THE NUMERICAL MODEL

3.1 Governing Equations

The basic numerical model used is WIFM developed by the U. S. Army Corps of Engineers at the Waterways Experiment Station (WES) in Vicksburg, Mississippi. Some changes have been made in the model for this particular application and additional graphical capabilities have been added.

The hydrodynamic equations used in WIFM are derived from the classical Navier-Stokes equations and the continuity equation in a Cartesian coordinate system [10,14]. For turbulent flow in a Cartesian coordinate system with the positive z-axis in the vertical, these equations take the form:

$$\rho\left(u\frac{\partial u}{\partial x} + v\frac{\partial u}{\partial y} + w\frac{\partial u}{\partial z} + \frac{\partial u}{\partial t}\right) - \rho f v = -\frac{\partial p}{\partial x} + \varepsilon\left(\frac{\partial^2 u}{\partial x^2} + \frac{\partial^2 u}{\partial y^2} + \frac{\partial^2 u}{\partial z^2}\right) \tag{1}$$

$$\rho\left(u\frac{\partial v}{\partial x} + v\frac{\partial v}{\partial y} + w\frac{\partial v}{\partial z} + \frac{\partial v}{\partial t}\right) + \rho f u = -\frac{\partial p}{\partial y} + \varepsilon\left(\frac{\partial^2 v}{\partial x^2} + \frac{\partial^2 v}{\partial y^2} + \frac{\partial^2 v}{\partial z^2}\right) \tag{2}$$

$$\rho\left(u\frac{\partial w}{\partial x} + v\frac{\partial w}{\partial y} + w\frac{\partial w}{\partial z} + \frac{\partial w}{\partial t}\right) = \rho g - \frac{\partial p}{\partial z} + \varepsilon\left(\frac{\partial^2 w}{\partial x^2} + \frac{\partial^2 w}{\partial y^2} + \frac{\partial^2 w}{\partial z^2}\right) \tag{3}$$

$$\frac{\partial \rho}{\partial t} + \frac{\partial}{\partial x}(\rho u) + \frac{\partial}{\partial y}(\rho v) + \frac{\partial}{\partial z}(\rho w) = 0 \tag{4}$$

The usual two-dimensional depth averaged equations are obtained by assuming: that the fluid is incompressible and homogeneous; that vertical accelerations of the fluid are negligible; and that the horizontal flow is reasonably uniform over the fluid depth. The three-dimensional equations are then integrated over the fluid depth from bottom to water surface and forced to satisfy the appropriate boundary conditions.

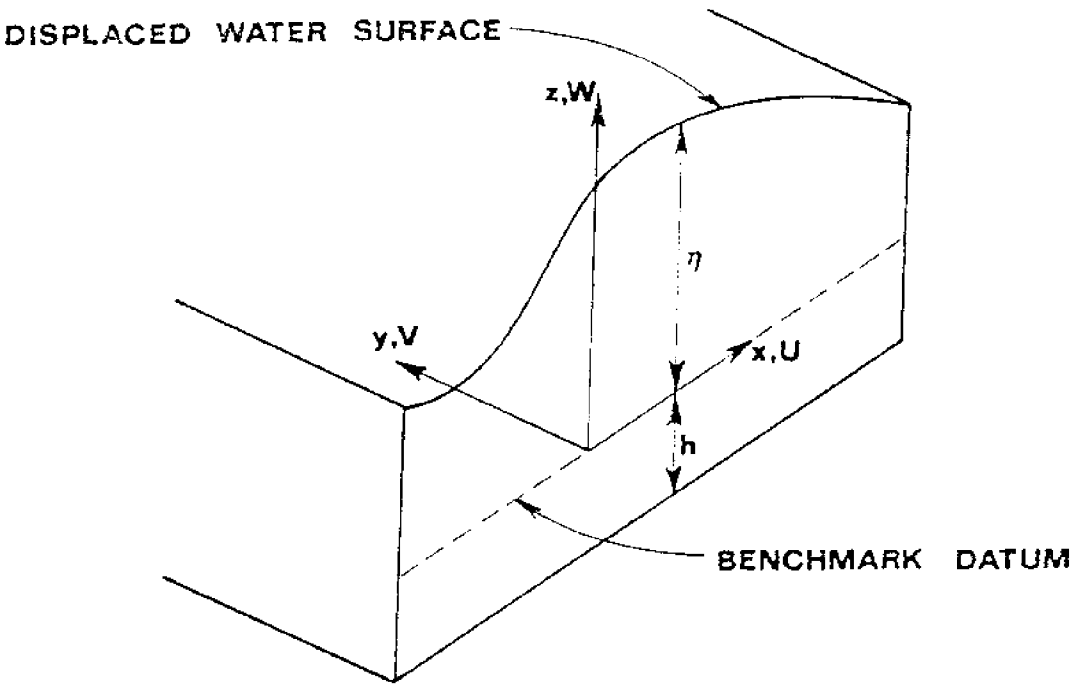

Figure 3. Cartesian Coordinate System for Problem Formulation

With reference to Figure 3, the model differential equations become:

Momentum Equations

$$\frac{\partial u}{\partial t} + u\frac{\partial u}{\partial x} + v\frac{\partial u}{\partial y} - fv + g\frac{\partial}{\partial x}(\eta - \eta_a)$$

$$+ \frac{gu}{C^2 d}(u^2 + v^2)^{\frac{1}{2}} - \varepsilon\left(\frac{\partial^2 u}{\partial x^2} + \frac{\partial^2 u}{\partial y^2}\right) + F_x = 0 \qquad (5)$$

$$\frac{\partial v}{\partial t} + u\frac{\partial v}{\partial x} + v\frac{\partial v}{\partial y} + fu + g\frac{\partial}{\partial y}(\eta - \eta_a)$$

$$+ \frac{gv}{C^2 d}(u^2 + v^2)^{\frac{1}{2}} - \varepsilon\left(\frac{\partial^2 v}{\partial x^2} + \frac{\partial^2 v}{\partial y^2}\right) + F_y = 0 \qquad (6)$$

Continuity Equation

$$\frac{\partial \eta}{\partial t} + \frac{\partial}{\partial x}(ud) + \frac{\partial}{\partial y}(vd) = \hat{R} \qquad (7)$$

The surface elevation (η) and the depth averaged velocity components (u,v) are the three unknowns in the model equations.

3.2 Stretched Coordinates

A major advantage of WIFM is the capability of applying a smoothly varying grid as shown in Figure 4 to the given study region permitting simulation of a complex landscape by locally increasing grid resolution and/or aligning coordinates along physical boundaries. Independently for each direction, a piecewise reversible transformation (analogous to that used by Wanstrath [16]) is used to map prototype or real space into computational space. The transformation takes the form

$$x = a + b\alpha^c \qquad (8)$$

where a, b, and c are arbitrary constants. The transformation is such that all derivatives are centered in α-space. Many stability problems commonly associated with variable grid schemes are eliminated via the continuity of the transformation procedure.

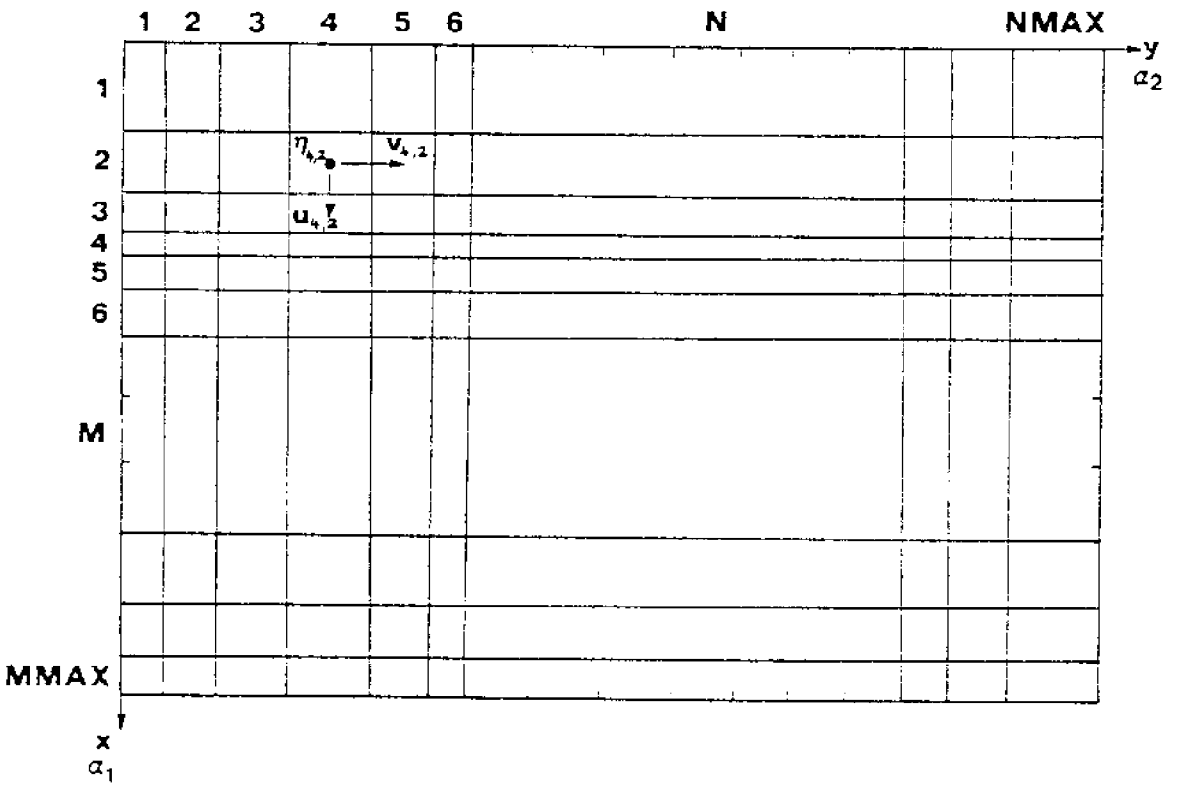

Figure 4. Computational Grid Index Coordinates

Introducing the transformation indicated in equation (8) the governing equations in α-space can be written as

Momentum Equations

$$u_t + \frac{1}{\mu_1} uu_{\alpha_1} + \frac{1}{\mu_2} vu_{\alpha_2} - fv$$

$$+ \frac{g}{\mu_1}(\eta - \eta_a)_{\alpha_1} + \frac{gu}{C^2 d}(u^2 + v^2)^{\frac{1}{2}}$$

$$- \varepsilon\Big[\Big(\frac{1}{\mu_1}\Big)^2 u_{\alpha_1\alpha_1} + \frac{1}{\mu_1}\Big(\frac{1}{\mu_1}\Big)_{\alpha_1} u_{\alpha_1} + \Big(\frac{1}{\mu_2}\Big)^2 u_{\alpha_2\alpha_2}$$

$$+ \frac{1}{\mu_2}\Big(\frac{1}{\mu_2}\Big)_{\alpha_2} u_{\alpha_2}\Big] + F_{\alpha_1} = 0 \qquad (9)$$

$$v_t + \frac{1}{\mu_1} uv_{\alpha_1} + \frac{1}{\mu_2} vv_{\alpha_2} + fu + \frac{g}{\mu_2}(\eta - \eta_a)_{\alpha_2}$$

$$+ \frac{gv}{C^2 d}(u^2 + v^2)^{\frac{1}{2}} - \varepsilon\Big[\Big(\frac{1}{\mu_1}\Big)^2 v_{\alpha_1\alpha_1} + \frac{1}{\mu_1}\Big(\frac{1}{\mu_1}\Big)_{\alpha_1} v_{\alpha_1}$$

$$+ \Big(\frac{1}{\mu_2}\Big)^2 v_{\alpha_2\alpha_2} + \frac{1}{\mu_2}\Big(\frac{1}{\mu_2}\Big)_{\alpha_2} v_{\alpha_2}\Big] + F_{\alpha_2} = 0 \qquad (10)$$

Continuity Equations

$$\eta_t + \frac{1}{\mu_1}(du)_{\alpha_1} + \frac{1}{\mu_2}(dv)_{\alpha_2} = \hat{R} \qquad (11)$$

where

$$u_t = \frac{\partial u}{\partial t} \quad , \quad uu_{\alpha_1} = u\frac{\partial u}{\partial \alpha_1} \quad , \quad \text{etc.}$$

$$\mu_1 = \frac{\partial x}{\partial \alpha_1} = b_1 c_1 \alpha^{c_1 - 1} \qquad (12)$$

$$\mu_2 = \frac{\partial y}{\partial \alpha_2} = b_2 c_2 \alpha^{c_2 - 1} \qquad (13)$$

Quantities μ_1 and μ_2 define the stretching of the regular-spaced computational grid in α-space to approximate a study region in real space (directions α_1 and α_2 correspond to x and y, respectively).

Many numerical modelers have found it difficult to obtain meaningful solutions to equations (9-11) when advective terms (single bar underlined terms of equations (9 and 10)) are included. These terms are included in WIFM using a formulation by Weare [17]. The double bar underlined last terms in the momentum equations are representative of equivalent internal stress resultants due to turbulent and dispersive momentum flux [15]. They provide a mechanism for dissipating wave energy of wavelength on the order of twice the spatial step by smoothing curvatures developing in the solution. Although the finite difference formulations used for these terms alleviate most problems encountered when including such effects, appropriate grid parameters (time and spatial step-sizes) for the phenomena being modeled must be chosen.

3.3 Model Formulation Schemes

The model partial differential equations are to be approximated by finite difference equations. There are many computational techniques that can be used as a solution scheme. Basically, solution schemes can be classified as explicit or implicit.

Explicit solutions are formulated such that each difference equation has only one unknown. To advance the

solution through time it is necessary only to cycle through the equations solving for the new variables at each finite difference cell. The solution scheme is simple; however, such solution procedures generally have stability problems which severely restrict the allowable computational time step.

Implicit solution schemes are formulated such that each finite difference equation may have many unknowns. The implicit scheme thus requires solution of a system of simultaneous equations. The implicit methods have more desirable stability characteristics; however, they are more difficult to formulate and present computational problems. This is especially true as the number of simultaneous equations increases.

Alternating Direction Implicit (ADI) methods represent an attempt to retain the desirable stability characteristics of the implicit scheme while utilizing a relatively simple solution algorithm. ADI schemes restrict the number of unknowns in each finite difference equation to three. In addition, the coefficient matrix must be tri-diagonal, only the coefficient on the diagonal and on either side of the diagonal may be present. This general procedure leads to a two part solution scheme in which the finite difference grid is traversed in the x-direction followed by a traverse in the y-direction to complete the procedure. This model formulation, while implicit, is relatively easy to formulate and has an efficient solution procedure. A large number of

hydrodynamic and water quality models are based upon ADI formulations.

3.4 WIFM Model

The partial differential equations (9-11) derived from physical laws are to be approximated by finite difference equations. In the program WIFM, a special form of the ADI method is used. This method is known as the Stabilizing Correction (SC) scheme.

To illustrate the SC scheme consider the simplified linearized matrix equation

$$U_t + AU_x + BU_y = 0 \tag{14}$$

where

$$U = \begin{pmatrix} \eta \\ u \\ v \end{pmatrix} \quad , \quad A = \begin{pmatrix} 0 & d & 0 \\ g & 0 & 0 \\ 0 & 0 & 0 \end{pmatrix} \quad , \text{ and } B = \begin{pmatrix} 0 & 0 & d \\ 0 & 0 & 0 \\ g & 0 & 0 \end{pmatrix}$$

Applying a standard Crank-Nickolson technique [1,4,5,7] to equation (14) yields

$$\frac{1}{\Delta t}\,(U^{k+1} - U^k) + \frac{1}{2}\,(\frac{A}{\Delta x}\delta x + \frac{B}{\Delta y}\delta y)(U^{k+1} + U^k) = 0 \tag{15}$$

This equation can be written in a simpler form

$$(1 + \lambda_x + \lambda_y)\,U^{k+1} = (1 - \lambda_x - \lambda_y)\,U^k \tag{16}$$

where

$$\lambda_x = \frac{1}{2}\,\frac{\Delta t}{\Delta x}\,A\delta_x$$

$$\lambda_y = \frac{1}{2}\,\frac{\Delta t}{\Delta y}\,b\delta_y$$

By adding the quantity $\lambda_x\lambda_y(U^{k+1} - U^k)$ of order $(\Delta x^2, \Delta t^2)$, the equation can be factorized as

$$(1 + \lambda_x)(1 + \lambda_y)U^{k+1} = (1 - \lambda_x)(1 - \lambda_y)U^k \tag{17}$$

Introducing an intermediate value, U*, and splitting the equation into a two-step operation results in the basic equations for the Stabilizing Correction (SC) scheme,

$$(1 + \lambda_x)U^* = (1 - \lambda_x - 2\lambda_y)U^k \tag{18}$$

$$(1 + \lambda_y)U^{k+1} = U^* + \lambda_y U^k \tag{19}$$

The first step is to compute η and u implicitly for the first $\frac{1}{2}$ time step by sweeping the grid in the x-direction, and the second step is to compute η and v implicitly for the second $\frac{1}{2}$ time step by sweeping the grid in the y-direction. Completing both sweeps constitutes a full time step, and advances the solution to the next time step.

The form of the difference equations for the x-sweep is given by

$$\frac{1}{2\Delta t}(\eta^* - \eta^{k-1}) + \frac{1}{2\Delta x}\delta_x(u^{k+1}{}_d + u^{k-1}{}_d) + \frac{1}{\Delta y}\delta_y(v^{k-1}{}_d) = 0 \tag{20}$$

$$\frac{1}{2\Delta t}(u^{k+1} - u^{k-1}) + \frac{g}{2\Delta x}\delta_x(\eta^* + \eta^{k-1}) = 0 \tag{21}$$

y-sweep

$$\frac{1}{2\Delta t}(\eta^{k+1} - \eta^*) + \frac{1}{2\Delta y}\delta_y(v^{k+1}{}_d - v^{k-1}{}_d) = 0 \tag{22}$$

$$\frac{1}{2\Delta t}(v^{k+1} - v^{k-1}) + \frac{g}{2\Delta y}\delta_y(\eta^{k+1} + \eta^{k-1}) = 0 \tag{23}$$

The SC scheme can be expanded to the full model equations. Appropriate variables on each grid cell in a space-staggered fashion are defined as shown in Figure 5. The difference equations for the x-sweep can then be written as

$$\frac{1}{2\Delta t}\,(\eta^{*} - \eta^{k-1}) + \frac{1}{2\mu_1\Delta\alpha_1}\,[\delta_{\alpha_1}(u^{k+1}\,\bar{d}^{k} + u^{k-1}\,\bar{d}^{k})]$$

$$+ \frac{1}{\mu_2\Delta\alpha_2}\,\delta_{\alpha_2}(v^{k-1}\,\bar{\bar{d}}^{k}) = R \qquad \text{at } (n,m) \tag{24}$$

$$\frac{1}{2\Delta t}\,(u^{k+1} - u^{k-1}) + \frac{1}{2\mu_1\Delta\alpha_1}\,u^{k}\delta_{2\alpha_1}(u^{k})$$

$$+ \frac{1}{2\mu_2\Delta\alpha_2}\,\bar{\bar{v}}^{k}\delta_{2\alpha_2}(u^{k}) - f\bar{\bar{v}}^{k}$$

$$+ \frac{g}{2\mu_1\Delta\alpha_1}\,[\delta_{\alpha_1}(\eta^{*} + \eta^{k-1} - 2\eta_a^{k})]$$

$$+ \frac{g}{(\bar{C}^{2}\bar{d})^{k}}\,u^{k+1}\,[(u^{k-1})^{2} + (\bar{\bar{v}}^{k-1})^{2}]^{\frac{1}{2}}$$

$$- \varepsilon\,[\frac{1}{(\mu_1\Delta\alpha_1)^{2}}\,\delta_{\alpha_1\alpha_1}(u^{k})$$

$$+ \frac{1}{(\mu_2\Delta\alpha_2)^{2}}\,\delta_{\alpha_2\alpha_2}(u^{k}) + \frac{1}{2\mu_1\Delta\alpha_1^{2}}\,\delta_{\alpha_1}(\frac{1}{\mu_1})\,\delta_{2\alpha_1}(u^{k})$$

$$+ \frac{1}{2\mu_2\Delta\alpha_2^{2}}\,\delta_{\alpha_2}(\frac{1}{\mu_2})\delta_{2\alpha_2}(u^{k})] + F_{\alpha_1}^{k} = 0 \quad (n, m+\tfrac{1}{2}) \tag{25}$$

The difference operator is defined as

$\delta_\alpha(Z) = Z_{\alpha+\frac{1}{2}} - Z_{\alpha-\frac{1}{2}}$ for any variable Z.

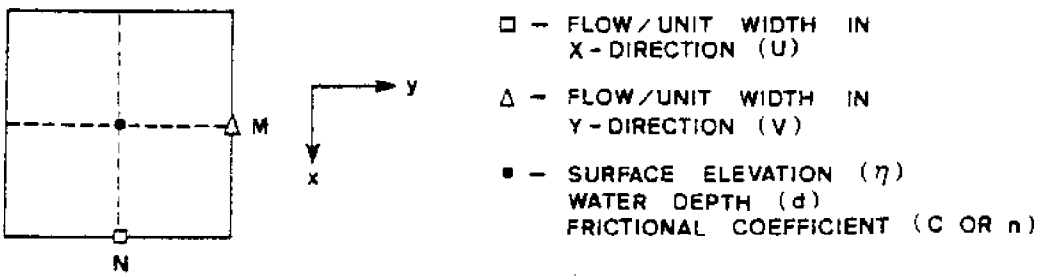

Figure 5. Grid Cell Definition

In addition a single bar over a variable (such as $\bar{d}$) represents a two point average and a double bar over a variable (such as $\bar{\bar{v}}$) represents a four-point average.

Applying these equations at each grid cell in a given direction results in a system of linear algebraic equations whose coefficient matrix is tridiagonal. It should be noted that the entire grid of finite difference equations is not solved simultaneously. The numerical procedure allows calculations of one row (or column) at a time. In fact, if there are more than two boundary conditions to be applied on the row (or column) then the row will be broken into separate computational segments. A computational segment is defined by a lower and upper boundary condition to be applied on the row (column). The numerical procedure actually solves each computational segment independently.

Gathering the terms to be computed along the x-direction at time level $(k+1)\Delta t$, equations 23 and 24 can be written as follows

$$-a_m \eta^*_{n,m} + \bar{a}_{m+\frac{1}{2}} u^{k+1}_{n,m+\frac{1}{2}} + a_{m+1} \eta^*_{n,m+\frac{1}{2}} = B_{m+\frac{1}{2}} \tag{26}$$

$$-a_{m-\frac{1}{2}} u^{k+1}_{m-\frac{1}{2}} + \eta^*_{n,m} + a_{m+\frac{1}{2}} u^{k+1}_{n,m+\frac{1}{2}} = A_m \tag{27}$$

where

$$A_m = \eta^{k-1}_{n,m} - \frac{\Delta t}{(\mu_1)_m \Delta\alpha_1} \delta_{\alpha_1}(u^{k-1}\, d^k)$$

$$- \frac{2\Delta t}{(\mu_2)_n \Delta\alpha_2} \delta_{\alpha_2}(v^{k-1}\, d^k)$$

$$+ 2\Delta t\, R^k_{n,m} \qquad \text{at } (n,m) \tag{28}$$

$$B_{m+\frac{1}{2}} = u^{k-1}_{n,m+\frac{1}{2}} + \Delta t \{ \bar{\bar{v}}^k_{n,m+\frac{1}{2}} \left(2f - \frac{\delta_{2\alpha_2}(u^k)}{(\mu_2)_n \Delta\alpha_2}\right)$$

$$- \frac{u^k_{n,m+\frac{1}{2}} \delta_{2\alpha_1}(u^k)}{(\mu_1)_{m+\frac{1}{2}} \Delta\alpha_1} - \frac{g}{(\mu_1)_{m+\frac{1}{2}} \Delta\alpha_1} \delta_{\alpha_1} (\eta^{k-1} - 2\eta^k_a)$$

$$+ 2\epsilon \Big[\frac{\delta_{\alpha_1\alpha_1}(u^k)}{((\mu_1)_{m+\frac{1}{2}} \Delta\alpha_1)^2} + \frac{\delta_{\alpha_2\alpha_2}(u^k)}{((\mu_2)_n \Delta\alpha_2)^2}$$

$$+ \frac{1}{2(\mu_1)_{m+\frac{1}{2}} \Delta\alpha_1^2} \delta_{\alpha_1}\left(\frac{1}{\mu_1}\right) \delta_{2\alpha_1}(u^k)$$

$$+ \frac{1}{2(\mu_2)_n \Delta\alpha_2^2} \delta_{\alpha_2}\left(\frac{1}{\mu_2}\right) \delta_{2\alpha_2}(u^k) \Big] + 2F^k_{\alpha_1} \} \qquad \text{at } (n, m+\tfrac{1}{2}) \tag{29}$$

$$\bar{\bar{v}}^k_{n,m+\frac{1}{2}} = \frac{1}{4} \left(v^k_{n+\frac{1}{2},m} + v^k_{n-\frac{1}{2},m} + v^k_{n+\frac{1}{2},m+1} + v^k_{n-\frac{1}{2},m+1}\right) \tag{30}$$

The coefficients are defined as

$$a_{m\pm\frac{1}{2}} = \frac{\Delta t}{(\mu_1)_m \Delta\alpha_1} \bar{d}_{n,m\pm\frac{1}{2}} \tag{31}$$

$$a_m = a_{m+1} = \frac{(\Delta t)g}{(\mu_1)_{m+\frac{1}{2}} \Delta\alpha_1} \tag{32}$$

$$\bar{a}_{m+\frac{1}{2}} = 1 + \frac{2g(\Delta t)}{(\bar{c}^2\bar{d})^k_{n,m+\frac{1}{2}}} [(u^{k-1}_{n,m+\frac{1}{2}})^2 + (\bar{v}^{k-1}_{n,m+\frac{1}{2}})^2]^{\frac{1}{2}} \tag{33}$$

For a finite difference cell adjacent to the model boundary, certain boundary conditions on velocity or surface elevation will be specified. For example, at a land boundary the velocity normal to the boundary is zero. At a river boundary, the velocity will be a specified function of time. At a tidal boundary, the surface elevation will be a prescribed function of time. For example, assuming that η_m is a specified water elevation at the lower boundary and that $u^{k+1}_{n,L+\frac{1}{2}}$ is a given velocity at the upper boundary, the equations for line n can be written in matrix form.

$$\begin{bmatrix} \bar{a}_{M+\frac{1}{2}} & a_{M+1} & & & \cdots & 0 \\ -a_{M+\frac{1}{2}} & 1 & a_{M+3/2} & 0 & \cdots & 0 \\ 0 & -a_{M+1} & \bar{a}_{M+3/2} & a_{M+2} & \cdots & 0 \\ & & & & \cdots & \\ & & & & \cdots & \\ & & & & \cdots & \\ 0 & 0 & 0 & \cdots & -a_{L-\frac{1}{2}} & 1 \end{bmatrix} \begin{bmatrix} u^{k+1}_{M+\frac{1}{2}} \\ \eta^*_{M+1} \\ u^{k+1}_{M+3/2} \\ 0 \\ 0 \\ 0 \\ \eta^*_L \end{bmatrix} = \begin{bmatrix} \hat{B}_{M+\frac{1}{2}} \\ A_{M+1} \\ B_{M+3/2} \\ 0 \\ 0 \\ 0 \\ \hat{A}_L \end{bmatrix}^k \tag{34}$$

By defining the process of elimination as a set of recursive formulas, the above tridiagonal equations can be solved with a minimum number of operations. Starting with equation (25)

$$u_{m+\frac{1}{2}}^{k+1} = -R_m \eta_{m+1}^* + S_m \tag{35}$$

where

$$R_m = \frac{a_{m+1}}{\bar{a}_{m+\frac{1}{2}}} \quad ; \quad S_m = \frac{\hat{B}_{m+\frac{1}{2}}}{\bar{a}_{m+\frac{1}{2}}} \tag{36}$$

and

$$\hat{B}_{m+\frac{1}{2}} = B_{m+\frac{1}{2}} + a_m \eta_M^* \tag{37}$$

By substituting equation (34) into equation (26) (evaluated at M+1), we obtain

$$-a_{m+\frac{1}{2}}(-R_m \eta_{m+1}^* + S_m) + \eta_{m+1}^* + a_{m+3/2}\, u_{m+3/2}^{k+1} = A_{m+1} \tag{38}$$

or

$$\eta_{m+1}^* = -P_{m+1} u_{m+3/2}^{k+1} + Q_{m+1} \tag{39}$$

where

$$P_{m+1} = \frac{a_{m+3/2}}{1 + a_{m+\frac{1}{2}} R_m} \quad ; \quad Q_{m+1} = \frac{A_{m+1} + a_{m+\frac{1}{2}} S_m}{1 + a_{m+\frac{1}{2}} R_m} \tag{40}$$

Also the velocity can be expressed as a function of the next water level

$$u_{m+3/2}^{k+1} = -R_{m+1} \eta_{m+2}^* + S_{m+1} \tag{41}$$

where

$$R_{m+1} = \frac{a_{m+2}}{\bar{a}_{m+3/2} + a_{m+1} R_{m+1}} \quad ; \quad S_{m+1} = \frac{B_{m+3/2} + a_{m+1} Q_{m+1}}{\bar{a}_{m+3/2} + a_{m+1} R_{m+1}} \tag{42}$$

The recursion formulas, in general, can be written as

$$\eta_m^* = -P_m u_{m+\frac{1}{2}}^{k+1} + Q_m \tag{43}$$

$$u_{m-\frac{1}{2}}^{k+1} = -R_{m-1}\eta_m^* + S_{m-1} \tag{44}$$

where

$$T1 = 1 + a_{m-\frac{1}{2}} R_{m-1} \qquad T2 = \bar{a}_{m+\frac{1}{2}} + a_m P_m$$

$$P_m = \frac{a_{m+\frac{1}{2}}}{T1} \qquad Q_m = \frac{A_m + a_{m-\frac{1}{2}} S_{m-1}}{T1} \tag{45}$$

$$R_m = \frac{a_{m+1}}{T2} \qquad S_m = \frac{B_{m+\frac{1}{2}} + a_m Q_m}{T2}$$

In the Fortran code the expanded form of the recursion formulas can be expressed by using a different index notation (N,M), respectively, for each direction (x,y). For the x-sweep:

Coefficient Equations

$$P_M = \frac{\Delta t\ \bar{d}_{N,M}^k}{(\mu_1)_{2M-1}\Delta\alpha_1} \Big/ \left[1 + \frac{\Delta t\ \bar{d}_{N,M-1}^k}{(\mu_1)_{2M-1}\Delta\alpha_1} R_{M-1}\right] \tag{46}$$

$$Q_M = \left[A_M + \frac{\Delta t\ \bar{d}_{N,M-1}^k}{(\mu_1)_{2M-1}\Delta\alpha_1} S_{M-1}\right] \Big/ \left[1 + \frac{\Delta t\ \bar{d}_{N,M-1}^k}{(\mu_1)_{2M-1}\Delta\alpha_1} R_{M-1}\right] \tag{47}$$

$$D1 = 1 + \frac{2\Delta t}{\bar{d}_{N,M}^k\ (C_{N,M+1} + C_{N,M})^2} \cdot \left[(u_{N,M}^{k-1})^2 + (\bar{v}_{N,M}^{k-1})^2\right]^{\frac{1}{2}}$$

$$+ \frac{g\Delta t}{(\mu_1)_{2M}\Delta\alpha_1} P_M \tag{48}$$

$$R_M = \frac{g\Delta t}{(\mu_1)_{2M}\Delta\alpha_1} \Big/ D1 \tag{49}$$

$$S_M = [B_M + \frac{g\Delta t}{(\mu_1)_{2M}\Delta\alpha_1} Q_m] \; / \; D1 \tag{50}$$

The solution for each computational segment in the x-direction can be expressed as:

$$\eta^*_{N,M} = -P_M \, u^{k+1}_{N,M} + Q_M \tag{51}$$

$$u^{k+1}_{N,M-1} = -R_{M-1} \, \eta^*_{N,M} + S_{M-1} \tag{52}$$

The recursion coefficients, P, Q, R, and S, can be computed in succession between boundaries on column N. Depending upon the types of boundary conditions that are applied, various approximations of these coefficients are required. Having calculated the set of coefficients, the solution equation can be solved for all surface elevations and velocities in descending order.

The second computation is done by a similar operation, but this time solving for η and v implicitly, and advancing the time level to $(k+1)\Delta t$.

For the y-sweep:

Coefficient Equations

$$P_N = \frac{\Delta t \; \bar{d}_{N,M}}{(\mu_2)_{2N-1}\Delta\alpha_2} \; / \; [1 + \frac{\Delta t \; \bar{d}_{N-1,M}}{(\mu_2)_{2N-1}\Delta\alpha_2} R_{N-1}] \tag{53}$$

$$Q_N = [A_N + \frac{\Delta t \; \bar{d}_{N-1,M}}{(\mu_2)_{2N-1}\Delta\alpha_2} S_{N-1}] \; / \; [1 + \frac{\Delta t \; \bar{d}_{N-1,M}}{(\mu_2)_{2N-1}\Delta\alpha_2} R_{N-1}] \tag{54}$$

$$D2 = 1 + \frac{2g\Delta t}{\bar{d}^k_{N,M} \; (C_{N+1,M} + C_{N,M})^2} \cdot [(\bar{u}^{k-1}_{N,M})^2 + (v^{k-1}_{N,M})^2]^{\frac{1}{2}}$$

$$+ \frac{g\Delta t}{(\mu_2)_{2N}\Delta\alpha_2} P_N \tag{55}$$

$$R_N = \frac{g\Delta t}{(\mu_2)_{2N}\Delta\alpha_2} \; / \; D2 \tag{56}$$

$$S_N = [B_N + \frac{g\Delta t}{(\mu_2)_{2N}\Delta\alpha_2} Q_W] \; / \; D2 \tag{57}$$

The solution for each computational segment in the y-direction can be expressed as:

$$\eta^{k+1}_{N,M} = -P_M \, v^{k+1}_{N,M} + Q_N \tag{58}$$

$$v^{k+1}_{N-1,M} = -R_{N-1} \, \eta^{k+1}_{N,M} + S_{N-1} \tag{59}$$

3.5 Boundary Conditions

The program WIFM is formulated to handle three different general types of boundary conditions. These boundary types are: open boundaries, water-land boundaries, and subgrid barriers.

3.5.1 Open Boundaries

These boundaries define the computational cell rows or columns exiting the grid. At these boundaries water levels or flow rates are prescribed as functions of location and time. This is usually in the form of a tidal gage output or a river hydrograph. The open boundaries are shown on the grid for Biloxi Bay in Figure 6.

3.5.2 Water-Land Boundaries

The assumption made at these boundaries is that of "no-flow" normal to the boundary. This condition is

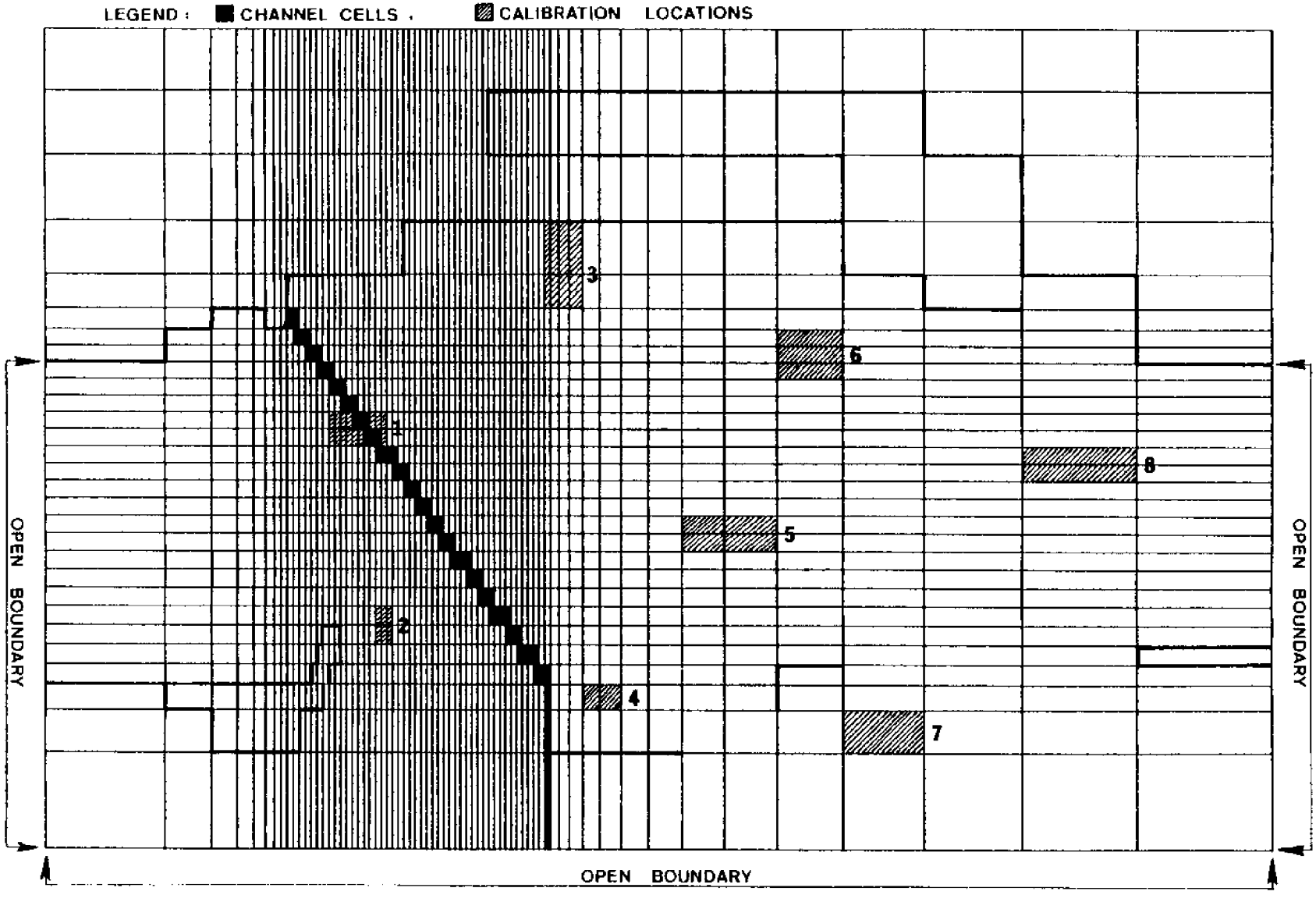

Figure 6. Finite Difference Grid for Study Area and Numerical Model Boundaries

satisfied by setting u=0 or v=0 at the appropriate cell face.

Since the program WIFM has a flooding capability, low-lying areas may dry and flood alternately several times within a tidal cycle depending on the flow conditions. Flooding and drying of a cell is controlled by checking the water levels in adjacent cells. The initial movement of water onto a dry cell is computed by a formula [13] given as

$$Q_n = \pm C_0 d_H \sqrt{d_H} \quad . \tag{60}$$

The closed boundary face is treated as open after the water level on the dry cell exceeds some small prescribed value (ε^*). Computations for water elevation (η), and velocities (u,v) are made for that cell as soon as the water level exceeds the value of ε^*. In equation (60), the admittance coefficient is taken less than 5.0 for controlling movement of water onto a dry cell. The drying of cells is inversely the same procedure as flooding. Figure 7 shows the graphic representation of flood cell treatment.

3.5.3 Subgrid Barriers

Subgrid barriers are defined along cell interfaces. The three types of subgrid barriers are shown in Figure 8.

The first type, namely exposed barrier, does not permit fluid flow across the appropriate flagged cell faces. As the water level increases the exposed barrier becomes an overtopping or submerged barrier. Overtopping barriers can

be submerged during one segment of the simulation and totally exposed in another.

For submerged and overtopping barriers the flow rate across the barrier is again computed by using the same transport formula, equation (60). The admittance coefficient (C_0) for the submerged and overtapping barriers will differ from that governing the initial movement of water onto a dry cell.

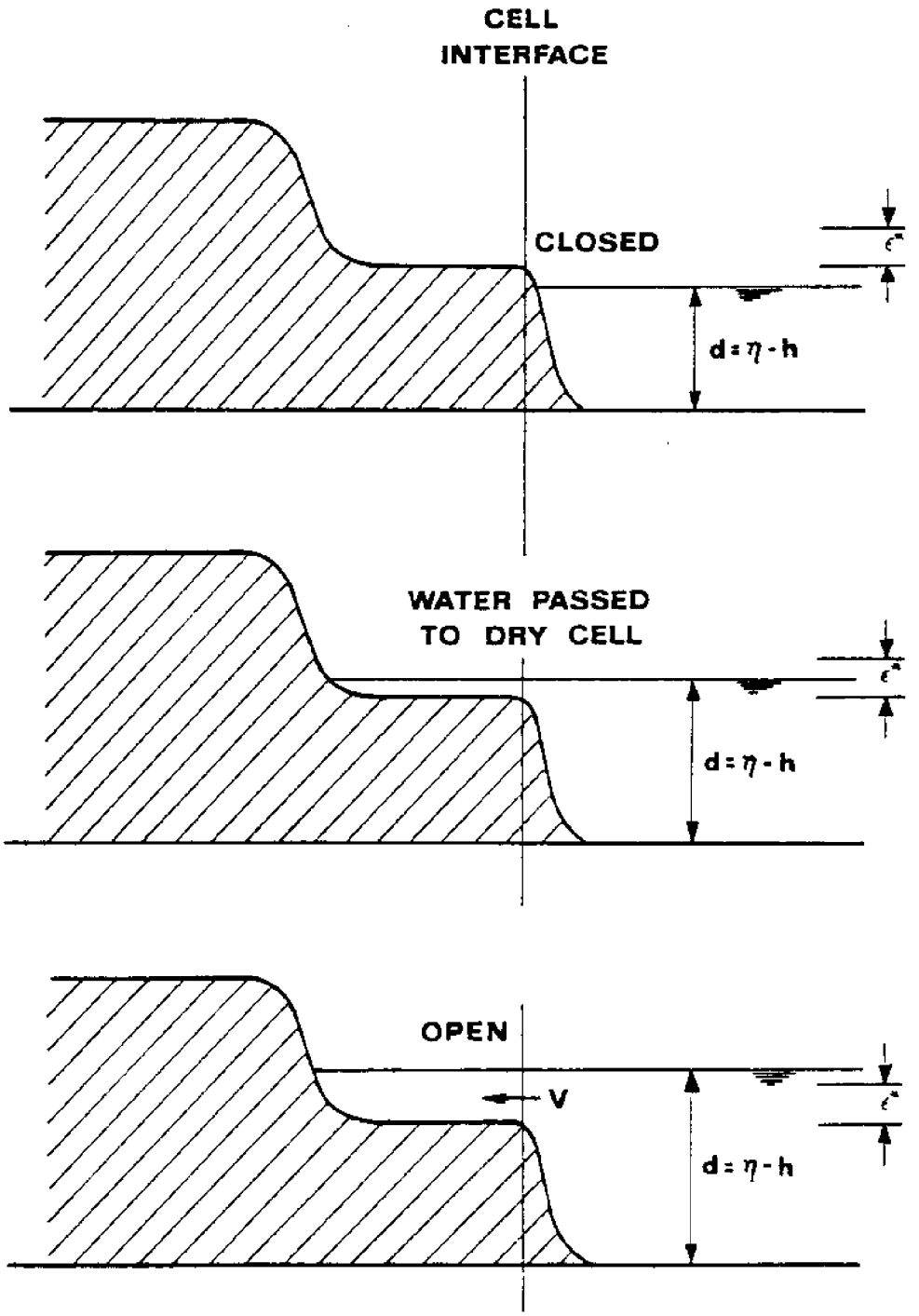

Figure 7. Flood Cell Treatment

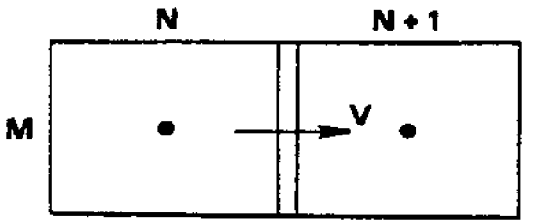

BARRIER AT CELL INTERFACE (HEIGHT b)

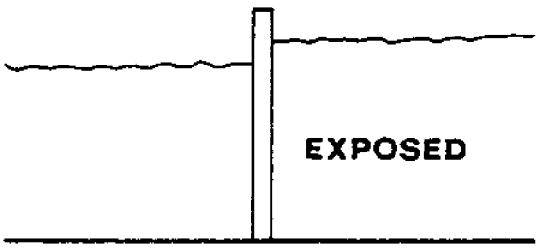

$V = 0$

$\eta_N < b + \epsilon^*$

$\eta_{N+1} < b + \epsilon^*$

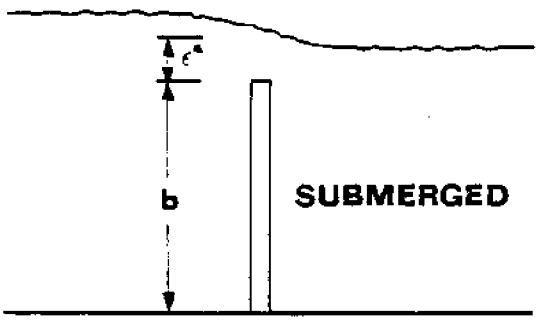

$\eta_N > b + \epsilon^*$

$\eta_{N+1} > b + \epsilon^*$

V CONTROLLED BY

SPECIAL CHEZY COEFFICIENT

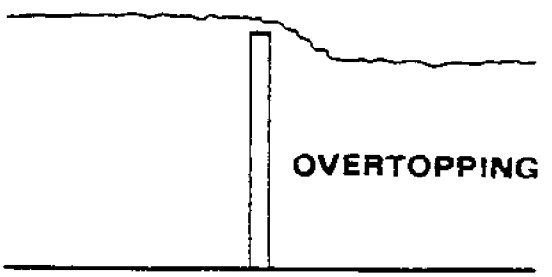

$\eta_N > b + \epsilon^*$

$\eta_{N+1} < b + \epsilon^*$

$V = C_o d_H \sqrt{d_H}$

WATER IS PASSED TO LOW SIDE

ACCORDING TO FLOW RATE V

Figure 8. Barrier Conditions Treated by WIFM

CHAPTER IV

THE STUDY AREA

Gulfport Harbor is located on the northeastern shoreline of the Gulf of Mexico, about 80 miles east of the Mississippi River Delta. The harbor and navigation channels are a part of Mississippi Sound, formed by the barrier islands along the Mississippi coastline. There has been a large amount of industrial development in the Mississippi Sound region. A number of federal, state and local projects are planned or underway to improve harbor and navigational facilities in the region.

The local area around Gulfport is shallow outside the ship channel. In Mississippi Sound, maximum water depths are approximately 15 feet while depths in the Gulfport area are generally 6 to 10 feet. The bottom material in Mississippi Sound is a combination of soft sand and mud. In some spots oyster shells can also be found.

A single ship channel connects Gulfport Harbor to the open sea as shown in Figure 2. The total length of the existing ship channel is 19 miles and the average channel depth is 26 feet. The ship channel must be maintained and possibly deepened to provide for commercial traffic into Gulfport Harbor.

CHAPTER V

FINITE DIFFERENCE GRID

The Gulfport Harbor area is to be represented by a variable size finite difference grid. Of particular interest is the navigation channel. It is desired to have good resolution of the navigation channel to ascertain the effect which deepening the channel would have on hydrodynamic variables.

The finite difference grid, Figure 9, was developed using a 1:80,000 scale nautical chart. As indicated previously the Gulfport Harbor grid represents a sub-grid of a finite difference model of Mississippi Sound. The relationship between the two models was shown in Figure 1. The finite difference cells were made smaller in areas where greater resolution is desired. Larger cells were used in areas where the bathymetry was reasonably constant and/or boundary geometry was relatively simple.

The dimension of the resulting grid is 68 by 29 or 1972 cells. The maximum depth in the region is 39 feet. The smallest cells are 672.4 feet in dimension corresponding to the approximate width of the navigation channel. A time step of 60 seconds will yield a reasonable Courant number for this combination of maximum depth and minimum cell size.

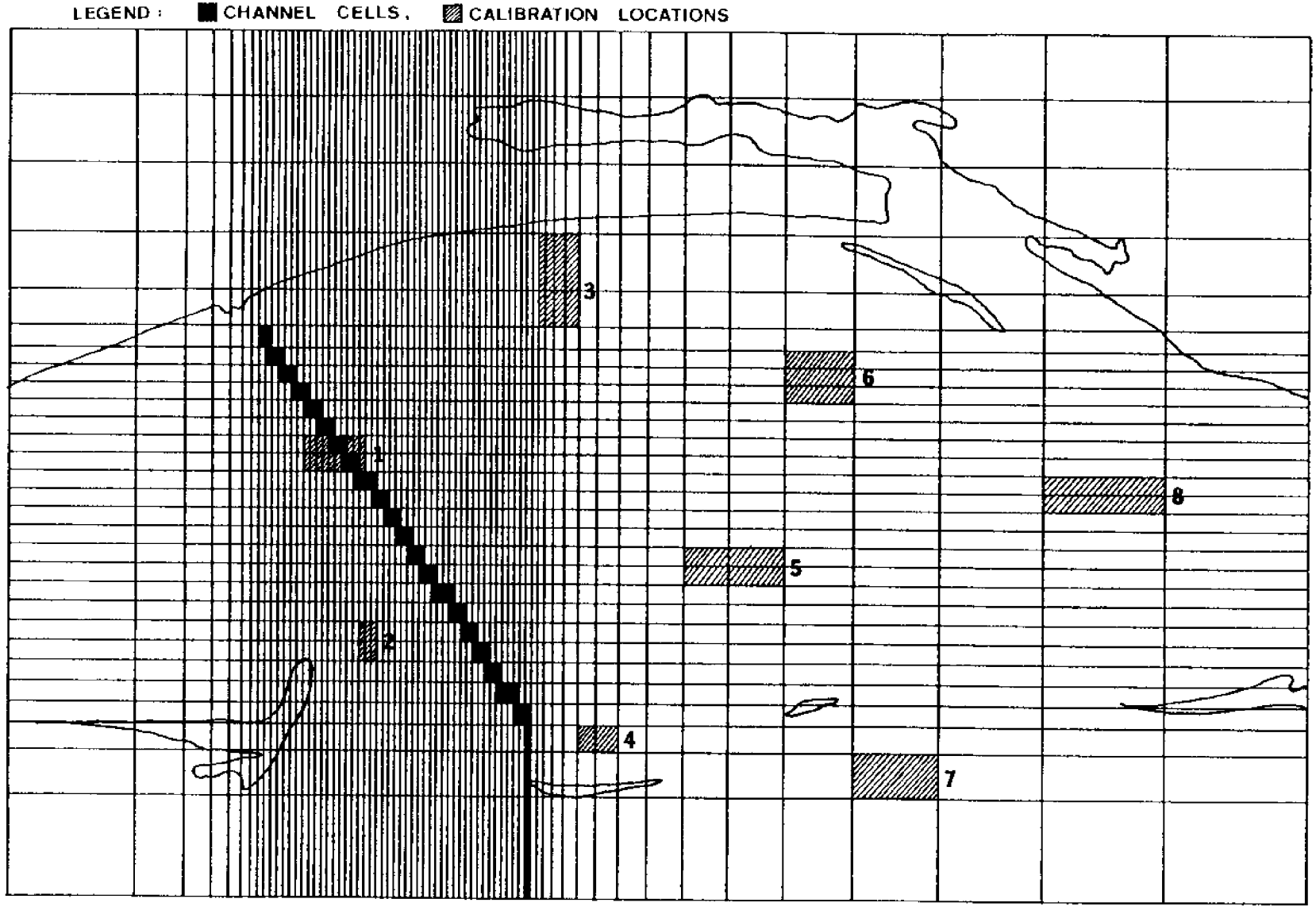

Figure 9. Finite Difference Grid for Study Area and Physical Boundaries

Depths were assigned to each water cell as delineated by the land boundary. The depth for each finite difference cell was determined as a weighted average of the charted depths within or adjacent to the cell. In areas where the finite difference water cell differs in size from the actual physical dimensions, cell depths were adjusted to make the cross-sectional areas approximately equal. Manning's n friction values for bottom roughness were assigned according to the bottom material specified by the nautical chart.

A tidal surface elevation boundary condition was applied at all computational boundaries. The imposed tidal condition was obtained from the Mississippi Sound model results and varies with location as well as time. There were no significant point source river inflow into the study region.

CHAPTER VI

MODEL CALIBRATION

Model calibration and verification consists of demonstrating that a numerical model can reproduce measured prototype data from the study area when the model is subjected to appropriate boundary conditions. Prototype data for estuarine systems are very expensive to obtain and are often not available in the desired quality or quantity. One of the conditions which a modeler (either physical or numerical) must often contend with is the use of a numerical model which has been only partially calibrated and verified.

In this case, 180 days of prototype data had previously been collected by the U. S. Army Corps of Engineers in Mississippi Sound. Water surface elevation, velocity, salinity, wind and other data were collected at a number of locations in the Sound. These data were used by the Mobile District, Corps of Engineers to calibrate and verify a numerical hydrodynamic and salinity model. The area covered by this model was shown in Figure 1. Unfortunately, the large finite difference cell size in this overall model of Mississippi Sound does not provide sufficient resolution to study small local regions.

Although a large amount of prototype data were available for Mississippi Sound, sufficient prototype data

were not available for the local Gulfport area to either establish model boundary conditions or to calibrate and verify the model. A combination of prototype data and results from the Mississippi Sound model were thus used in calibrating the Gulfport model. These data and numerical model results were provided by the Mobile District, Corps of Engineers. The Mississippi Sound model was previously calibrated to reproduce prototype data so this combination of prototype data and model data will be referred to as prototype data in the following discussions. Eight locations, shown in Figure 9, were used in a detailed comparison of results from the Gulfport Harbor model and prototype data. Model parameters were adjusted until satisfactory agreement was obtained at all points for the variables being considered.

The calibration results for water surface elevation are shown in Appendix A for the eight calibration locations. One observes an excellent agreement between the numerical model surface elevation results and prototype data.

Calibration results for velocity are presented in Appendix B. Velocity is a vector quantity, therefore, both magnitude and direction are indicated in the presentation of results. Velocity is a much more difficult quantity than surface elevation for a model to predict correctly. A very small gradient in surface elevation can result in significant velocity magnitudes. However, one observes a

satisfactory agreement between the model results and prototype data.

CHAPTER VII

RESULTS

In this study, the main objective was to observe the effects of the dredged ship channel on the hydrodynamics of Gulfport Harbor and Ship Channel. Several channel depths and dredge disposal plans have been investigated and their influence on circulation patterns considered.

The volume of dredged material from the deepened channel is calculated and distributed according to a specified dredge spoil disposal plan. Disposal areas are selected where the system hydrodynamics present the maximum potential for stable permanent disposal. Regions where large velocity gradients present opportunity for movement of the dredge spoil are avoided.

The results for one particular channel depth and dredge spoil disposal plan are presented to illustrate model usage. The navigation channel was deepened to 45 feet. For the deeper (45 foot) channel, changes were made in the data set by assigning new depth values to the cells corresponding to the ship channel locations. The disposal area for the dredged material is shown in Figure 10.

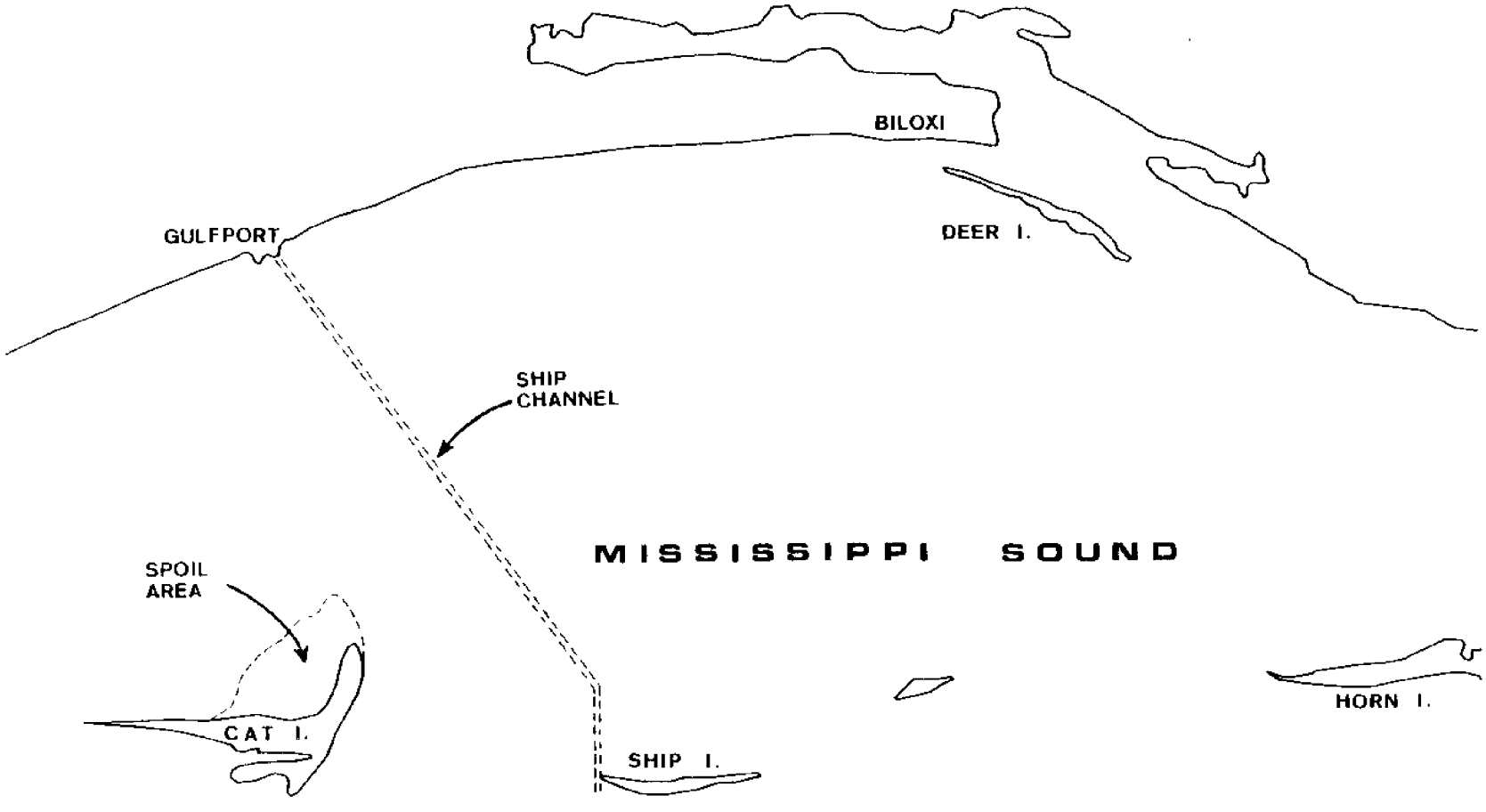

Figure 10. Disposal Area for Gulfport Channel Dredged Material

Water surface elevations for the deeper channel are presented in Appendix C and compared with water surface elevations for existing conditions. Velocity results for the deeper channel are presented in Appendix D and compared with existing conditions. The deeper channel is observed to change only slightly the overall hydrodynamics in the area. Measurable changes are very localized near the channel or the dredge disposal area.

Overall circulation patterns for existing conditions (26 foot channel) are presented in Appendix E. The length and direction of the plotted vectors represent the magnitude and direction of the water velocity. Appendix F presents the overall circulation patterns with the deeper channel (45 feet). The difference in circulation patterns which can be attributed to the deeper navigation channel are presented in Appendix G. These plots are obtained from the difference in velocity (both magnitude and direction) between the deeper channel results and existing condition results. Velocity difference plots are an excellent method for determining the "influence zone" for a particular modification to an estuarine system. In this case, the velocity difference plots clearly illustrate the local nature of changes. Hydrodynamic variables are changed significantly only in the immediate neighborhood of the channel or the dredge disposal area.

CHAPTER VIII

CONCLUSIONS AND RECOMMENDATIONS

A properly calibrated numerical model can be a valuable tool in the investigation of environmental changes in coastal regions. Various alternatives can be examined and potential environment effects evaluated. In this case, the numerical model for Gulfport Harbor and Ship Channels has been used to consider the effects of deepening navigational channels and considering alternative dredge disposal areas. Graphical presentation of results clearly indicate the extent and magnitude of hydrodynamic changes produced in the system.

Using prototype data combined with results from a numerical model covering a larger region appears to be a satisfactory model calibration procedure where limited prototype data are available. The numerical model data from the larger region is of particular value in establishing boundary conditions at the computational boundaries of the smaller model.

LIST OF REFERENCES

1. Ames, William F., "Numerical Methods for Partial Differential Equations," Academic Press, Second Edition, 1977.

2. Butler, H. L., "Numerical Circulation Study for Coos Bay - South Slough Bay Complex Oregon," Technical Report in publication, U. S. Army Engineer Waterways Experiment Station, CE, Vicksburg, MS, 1978a.

3. Butler, H. Lee, "Coastal Flood Simulation in Stretched Coordinates," 16th International Conference on Coastal Engineering, proc. to be published, Hamburg, Germany, 27 August - 1 September, 1978b.

4. Carnahan, Brice, Luther, H. A., and Wilkes, James O., "Applied Numerical Methods," John Wiley and Sons, Inc., 1969.

5. Ferziger, Joel H., "Numerical Methods for Engineering Application," John Wiley and Sons, 1981.

6. Garcia, A. W. and Butler, H. L., "Numerical Simulation of Tsunamis Originating in the Peru-Chile Trench," Proceedings, 15th International Conference on Coastal Engineering, Vol. 1, Chapter 61, pp. 1025-1043, Honolulu, HI, 11-17 July 1976.

7. Greenspan, Donald, "Discrete Numerical Methods in Physics and Engineering," Vol. 107 in Mathematics in Science and Engineering Series, Academic Press, Inc., 1974.

8. Houston, J. R., Whalin, R. W., Garcia, A. W., and Butler, H. L., "Effect of Source Orientation and Location in the Aleutian Trench on Tsunami Amplitude Along the Pacific Coast of the Continental United States," Research Report H-75-4, U. S. Army Engineer Waterways Experiment Station, CE, Vicksburg, MS, July 1975.

9. Houston, J. R., and Butler, H. L., "A Numerical Model for Tsunami Inundation," Technical Report HL-79-2, U. S. Army Engineer Waterways Experiment Station, CE, Vicksburg, MS, February 1979.

10. Pao, Richard H. F., "Fluid Dynamics," Charles E. Merrill Books, Inc. 1967.

11. Raney, D. C., and Butler, H. L., "A Numerical Model for Predicting the Effects of Landslide-Generated Water Waves," Research Report H-75-1, U. S. Army Engineer Waterways Experiment Station, CE, Vicksburg, MS, February 1975.

12. Raney, D. C., and Butler, H. L., "Landslide Generated Water Wave Model," Journal, Hydraulics Division, ASCE, Vol. 102, No. HY 9, Proc. Paper 12425, pp. 1269-1282, September 1976.

13. Reid, R. O., and Bodine, B. R., "Numerical Model for Storm Surges in Galveston Bay," Journal of Waterways and Harbors Division, ASCE, Vol. 94, No. WW 1, February 1968, Proc. Paper 5805, pp. 33-57.

14. Shames, Irving H., "Mechanics of Fluids," McGraw Hill Book Company, Inc., Second Edition, 1982.

15. Vreugdenhil, C. B., "Secondary Flow Computations," Delft Hydraulics Laboratory, Publication No. 114, November 1973.

16. Wanstrath, J. J., Whitaker, R. E., Reid, R. O., and Vastano, A. C., "Storm Surge Simulation in Transformed Coordinates, Vol. I - Theory and Application," Technical Report 76-3, U. S. Army Coastal Engineering Research Center, CE, Fort Belvoir, VA, November 1976.

17. Weare, T. John, "Errors Arising from Irregular Boundaries in ADI Solutions of the Shallow-Water Equations," International Journal for Numerical Methods in Engineering, Vol. 14, pp. 921-931, 1980.

APPENDIX A

Surface Elevation Calibration Curves for Gulfport Model

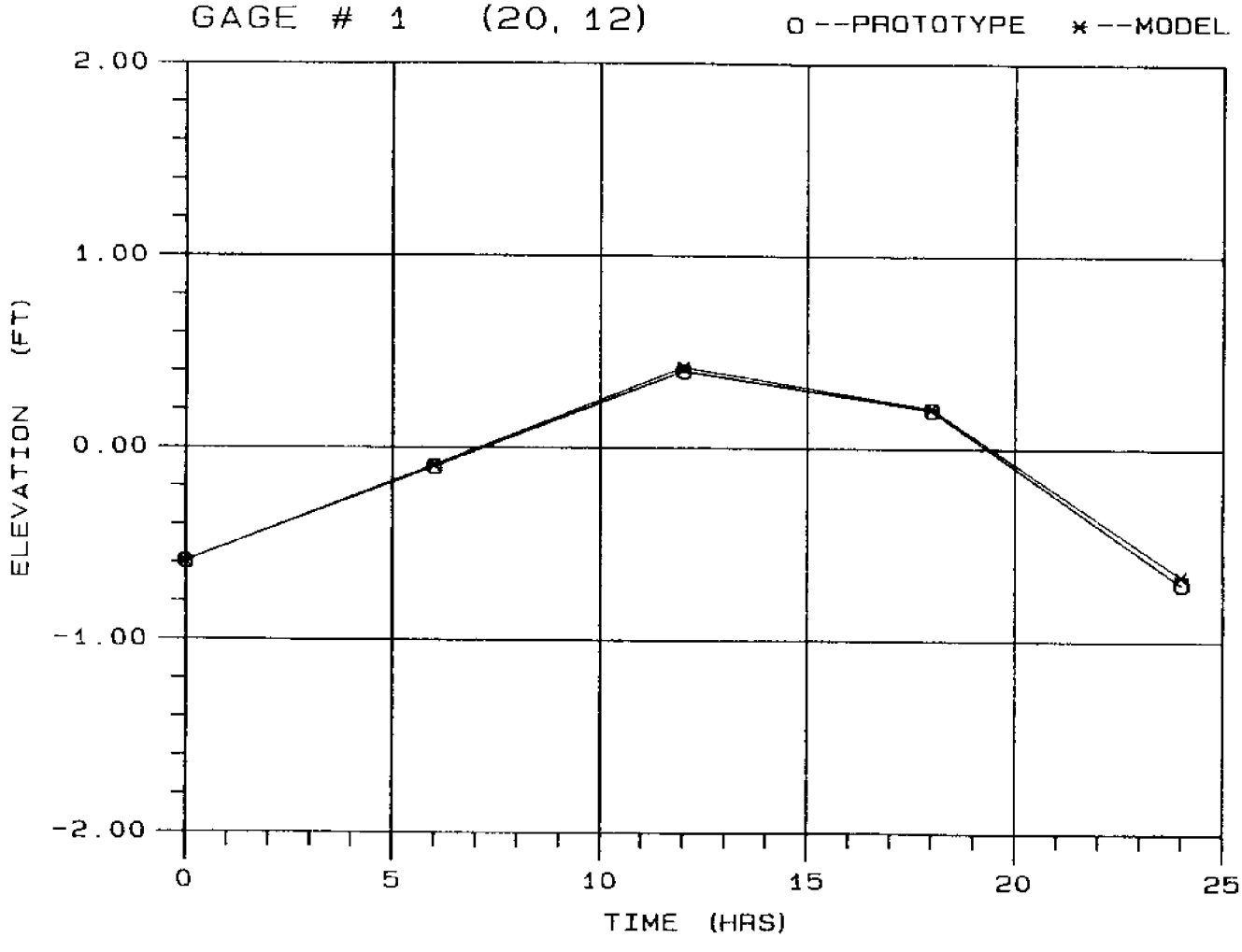

Figure A.1. Calibration Curve for Water Surface Elevation at Gage #1 for Existing Conditions

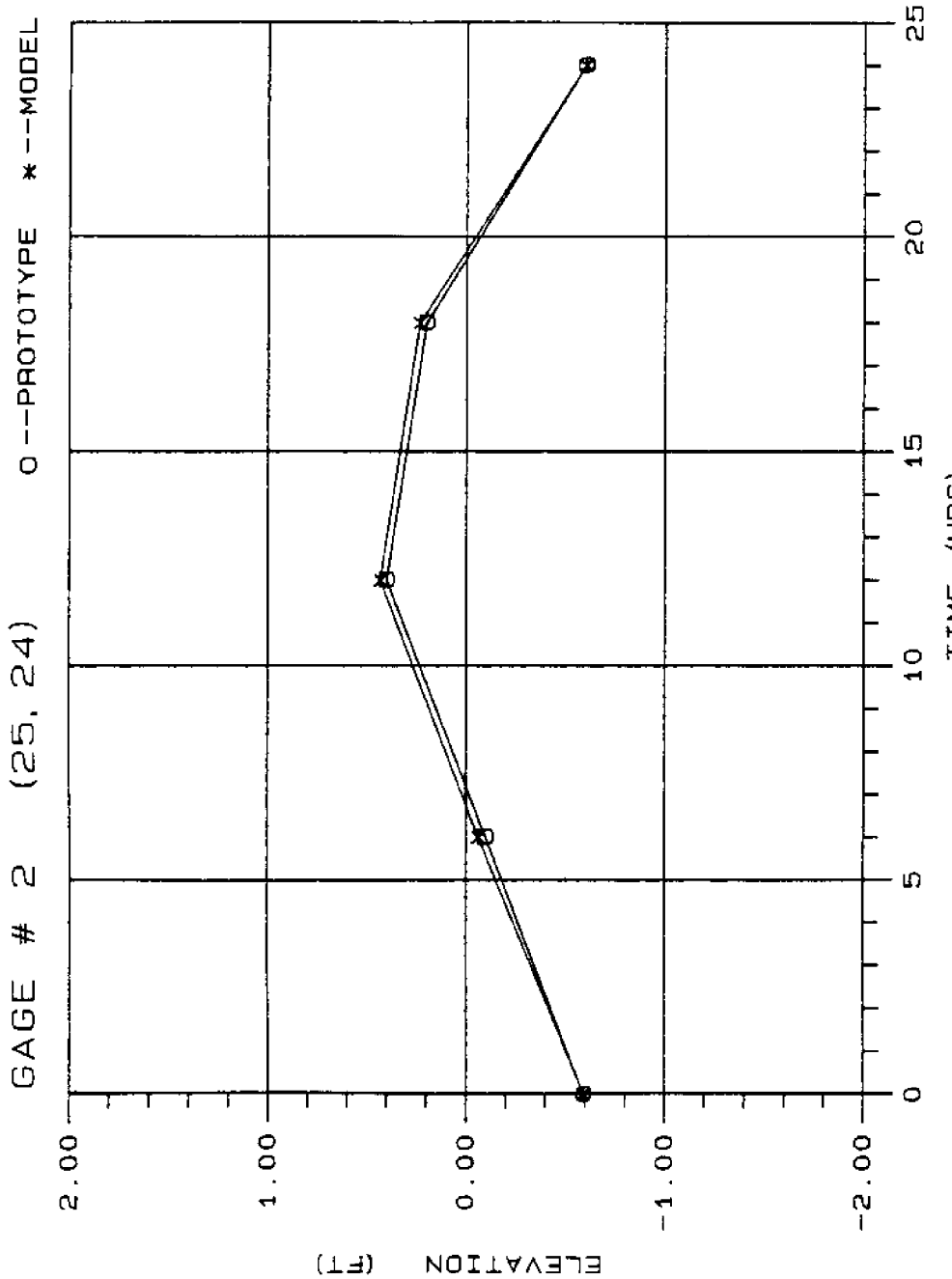

Figure A.2. Calibration Curve for Water Surface Elevation at Gage #2 for Existing Conditions

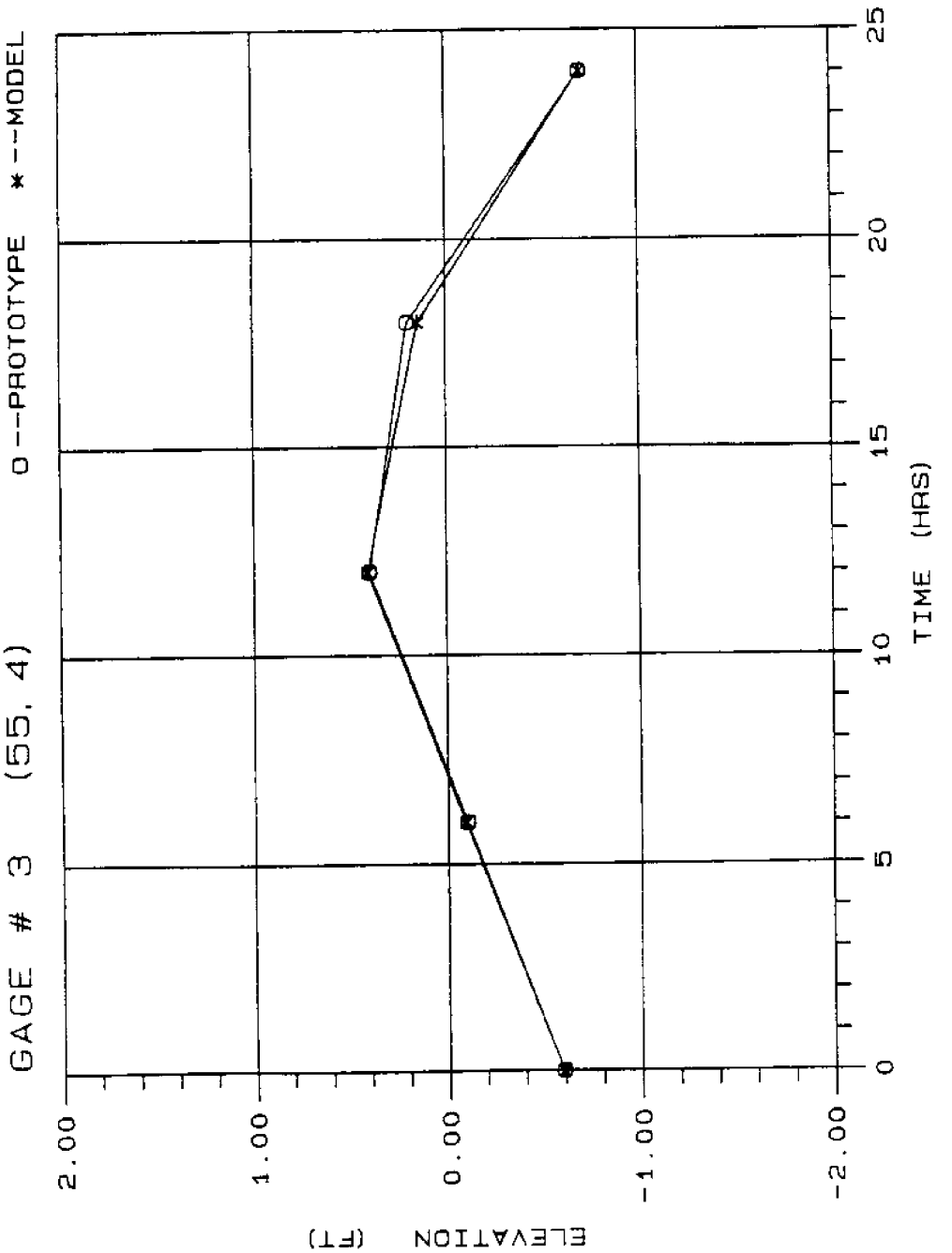

Figure A.3. Calibration Curve for Water Surface Elevation at Gage #3 for Existing Conditions

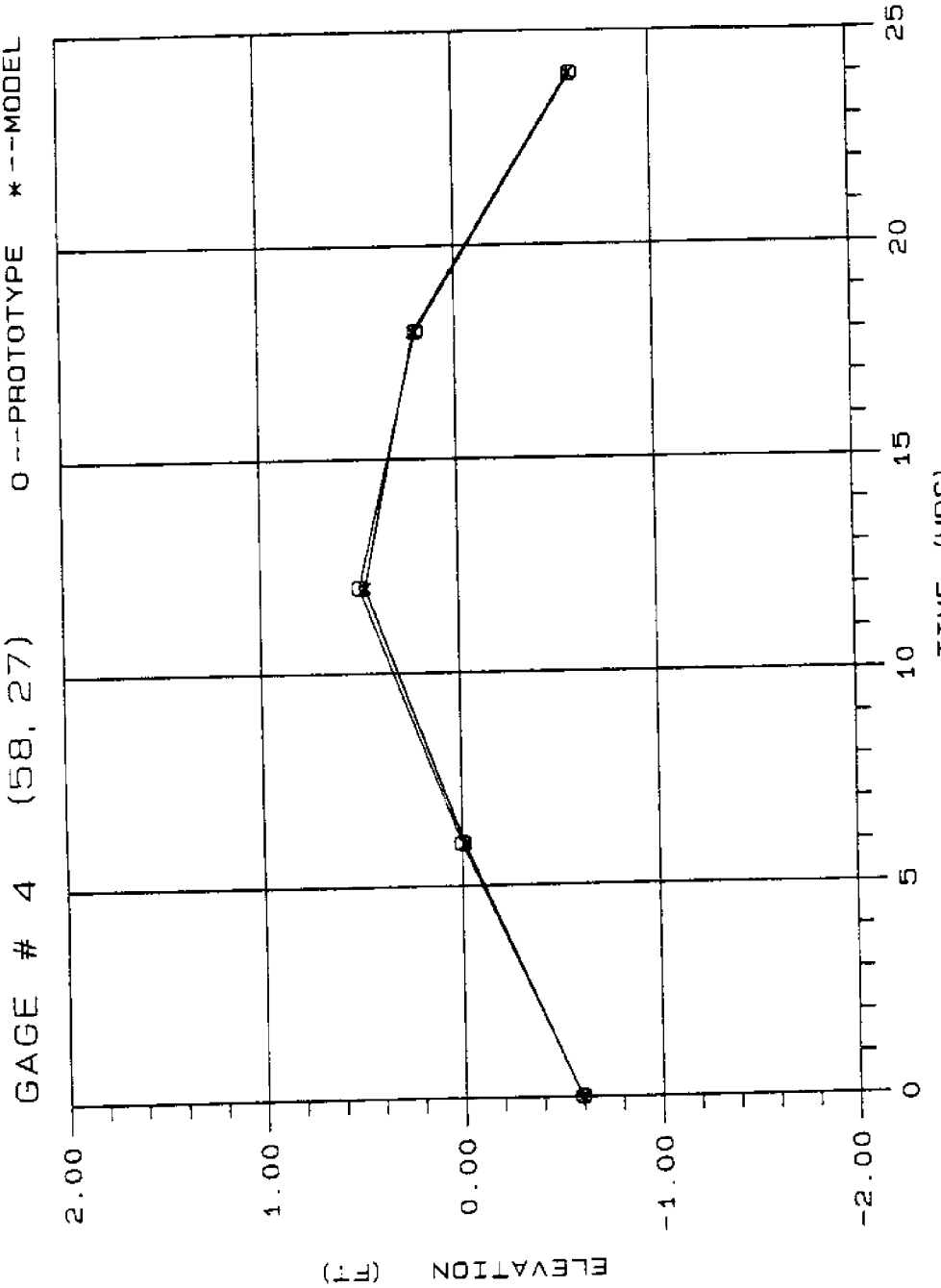

Figure A.4. Calibration Curve for Water Surface Elevation at Gage #4 for Existing Conditions

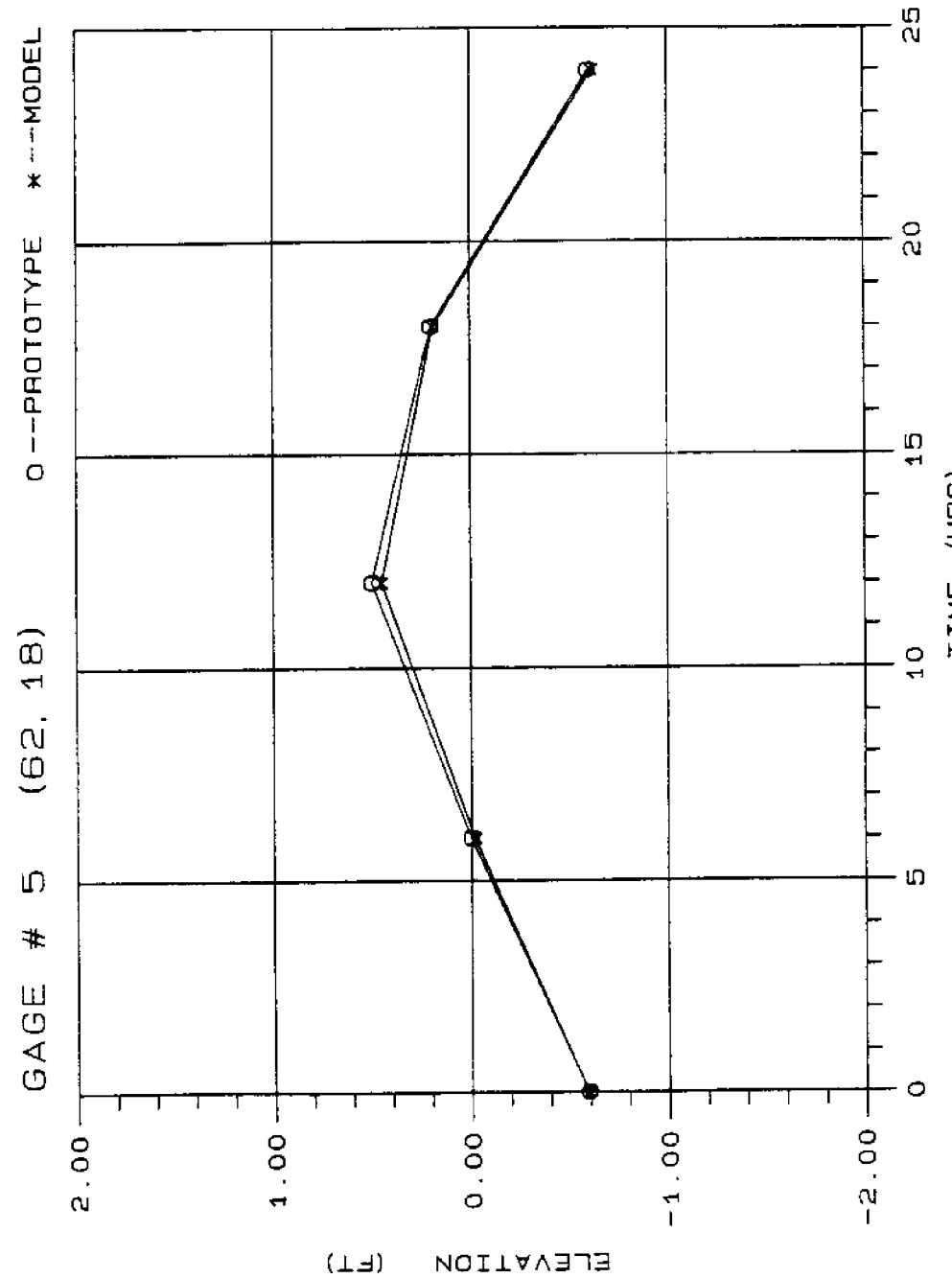

Figure A.5. Calibration Curve for Water Surface Elevation at Gage #5 for Existing Conditions

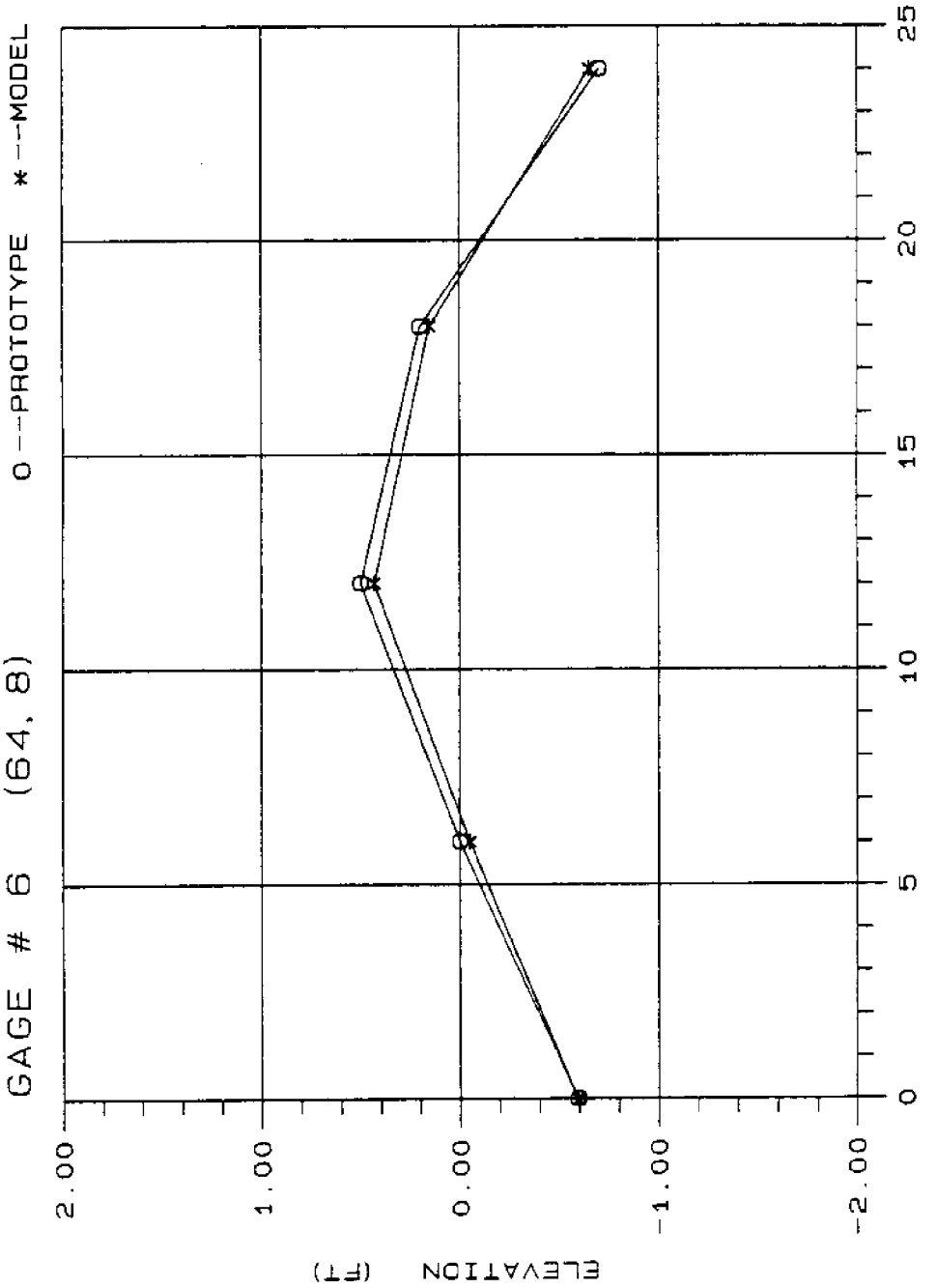

Figure A.6. Calibration Curve for Water Surface Elevation at Gage #6 for Existing Conditions

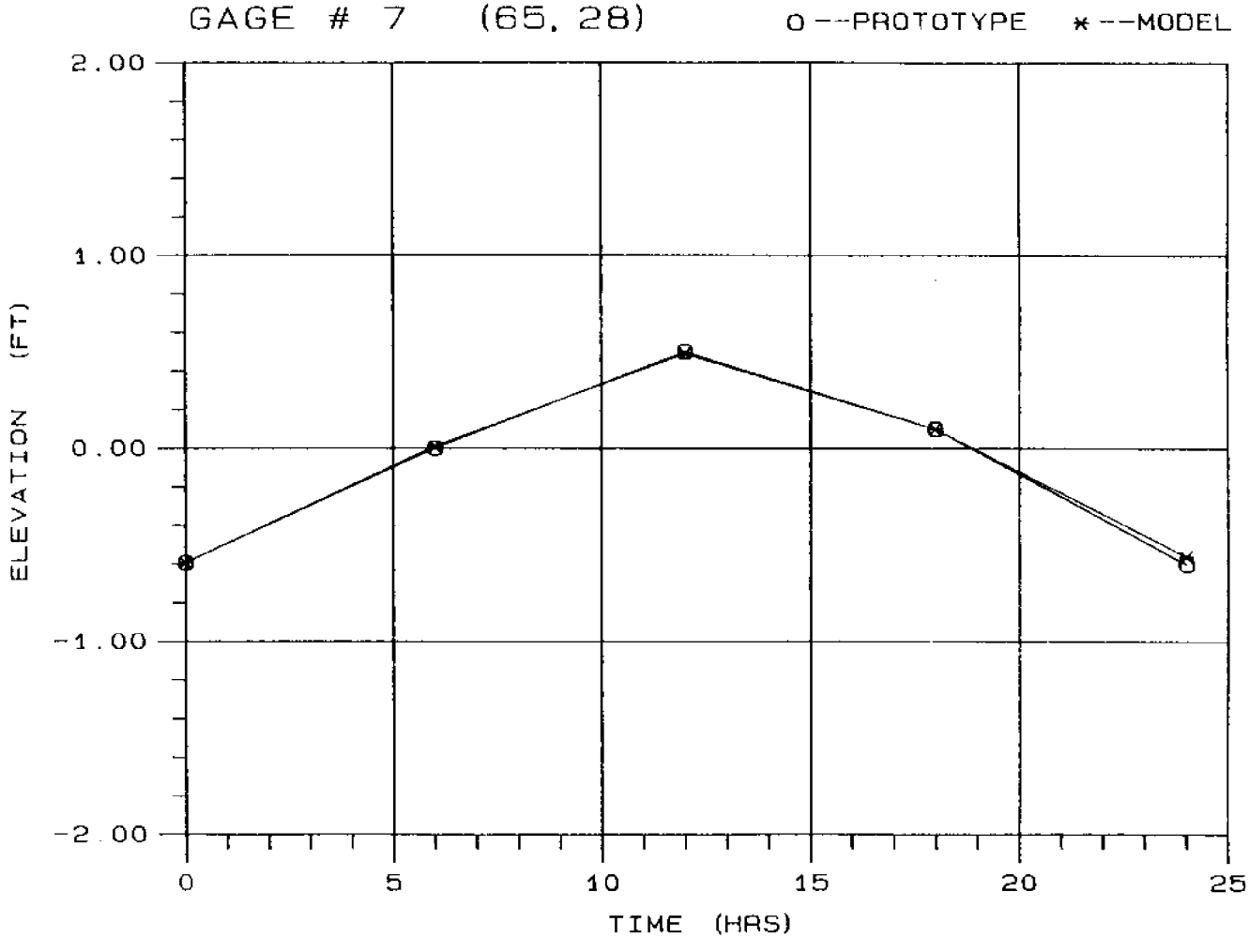

Figure A.7. Calibration Curve for Water Surface Elevation at Gage #7 for Existing Conditions

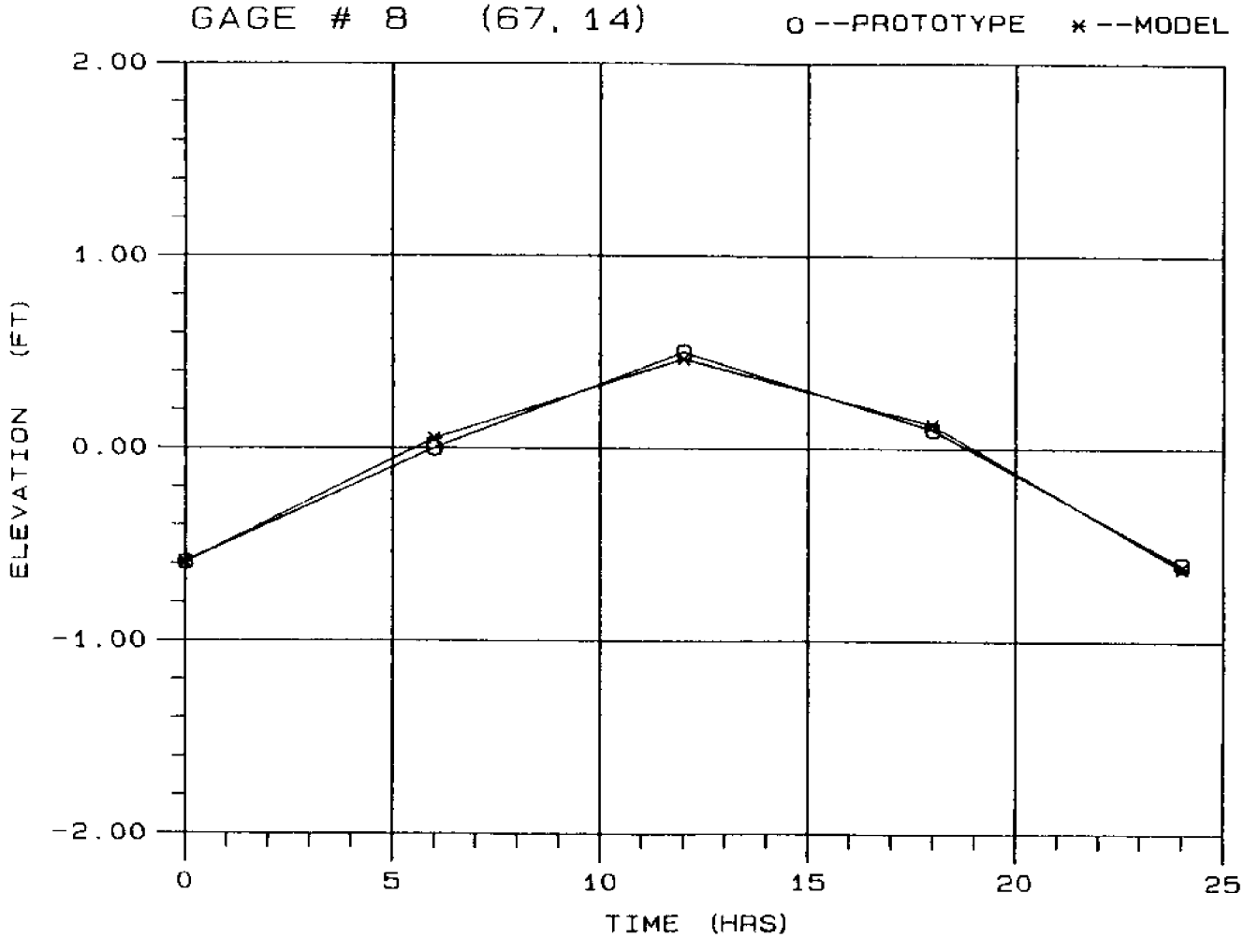

Figure A.8. Calibration Curve for Water Surface Elevation at Gage #8 for Existing Conditions

APPENDIX B

Velocity Calibration Curves for Gulfport Model

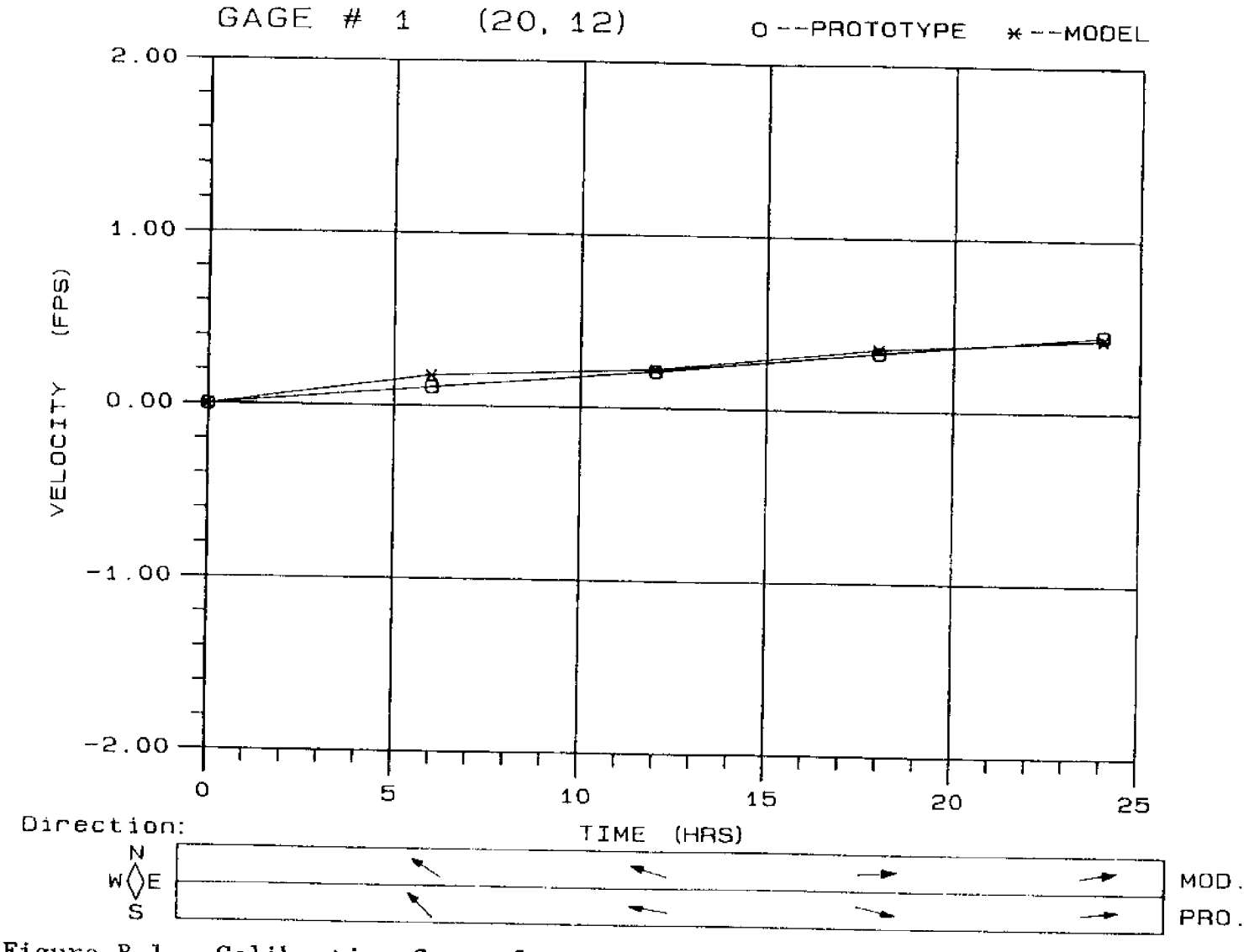

Figure B.1. Calibration Curve for Velocity at Gage #1 for Existing Conditions

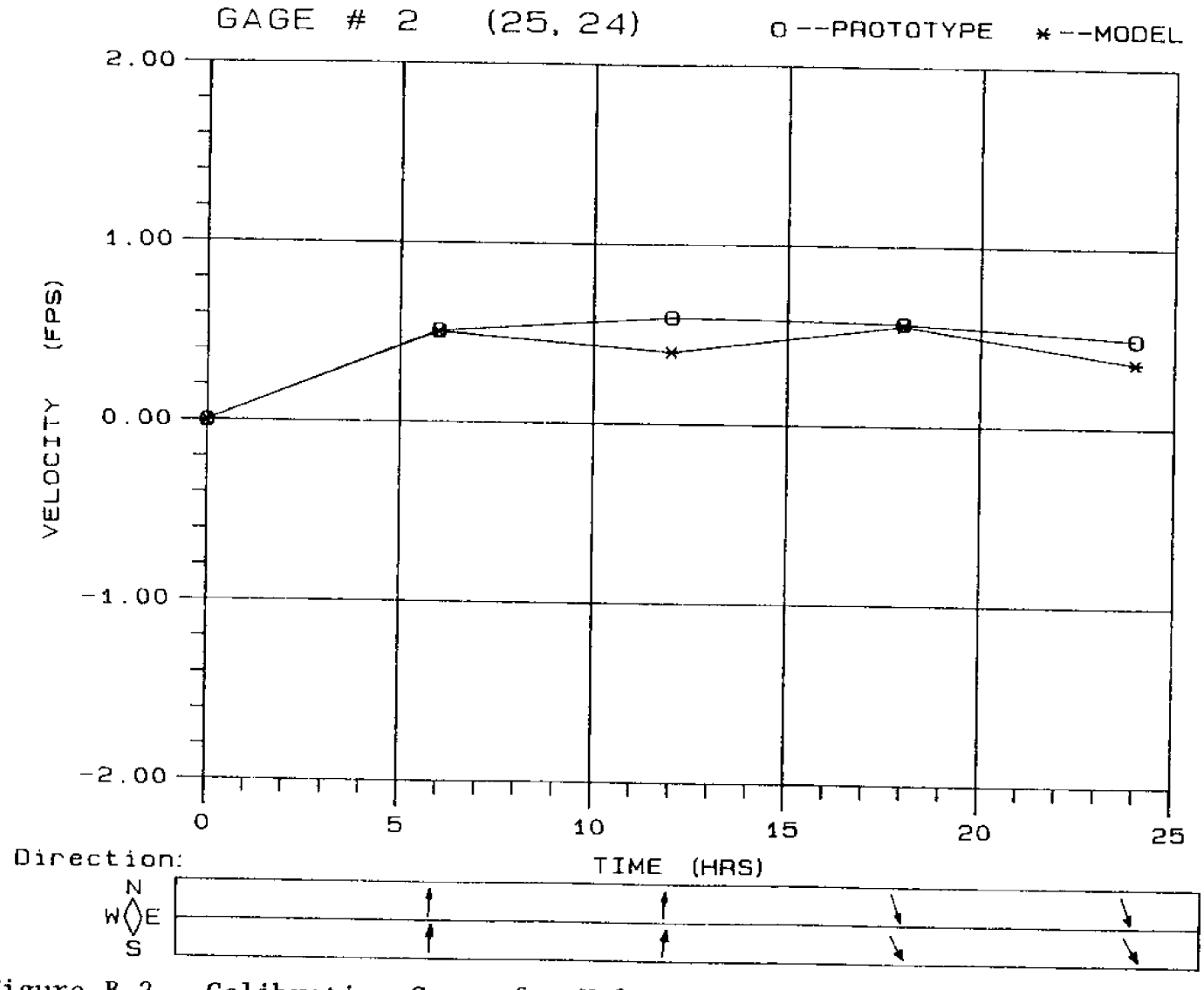

Figure B.2. Calibration Curve for Velocity at Gage #2 for Existing Conditions

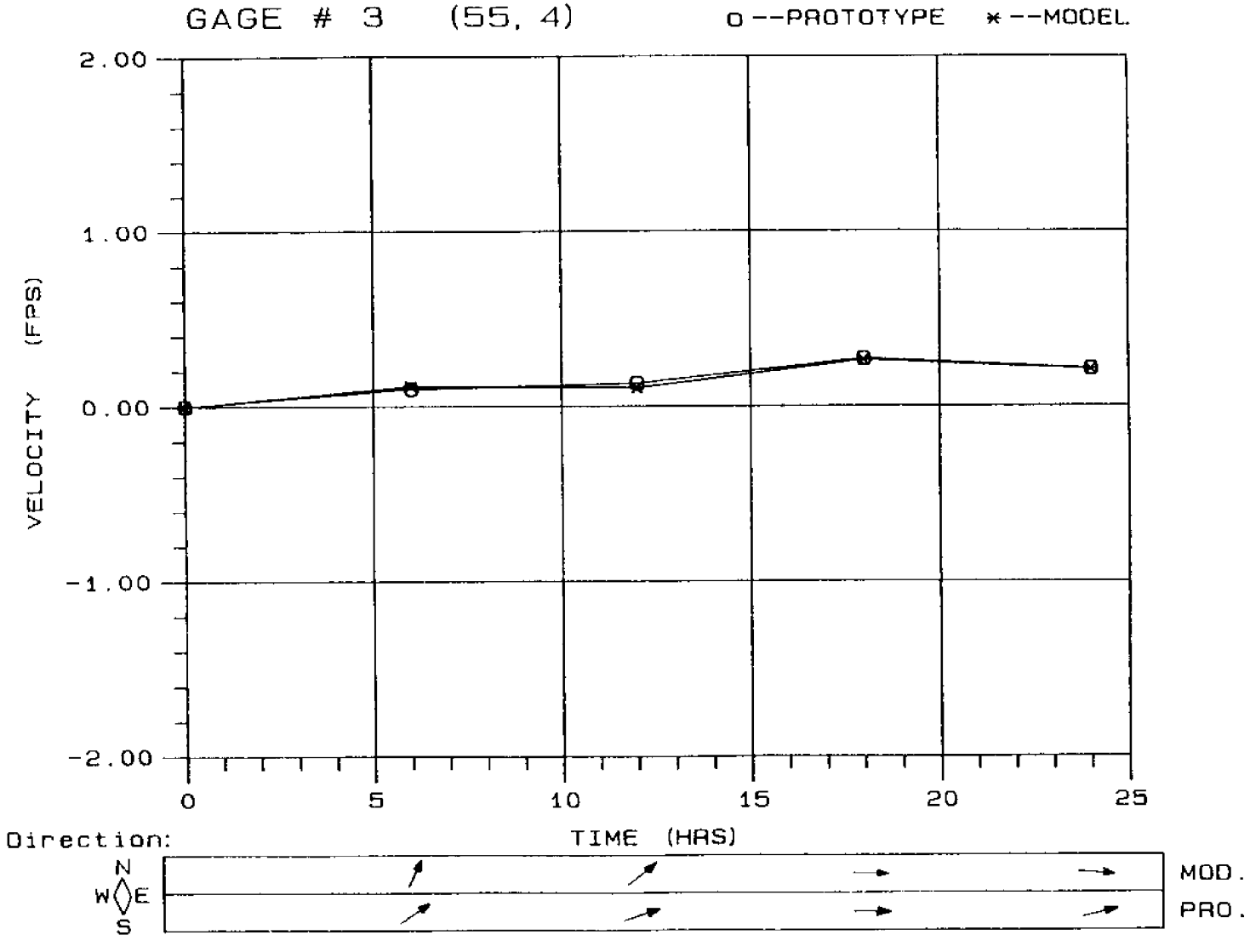

Figure B.3. Calibration Curve for Velocity at Gage #3 for Existing Conditions

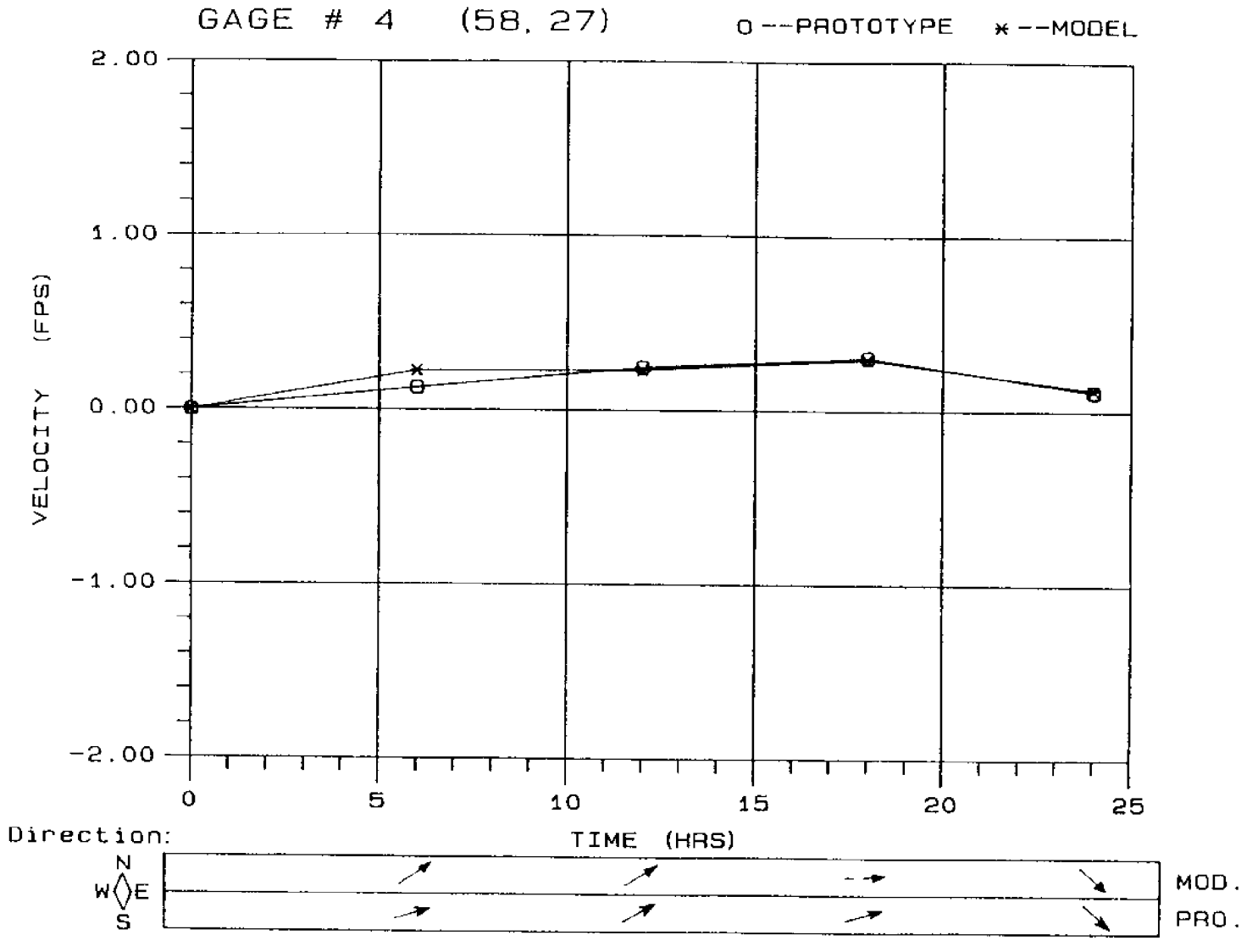

Figure B.4. Calibration Curve for Velocity at Gage #4 for Existing Conditions

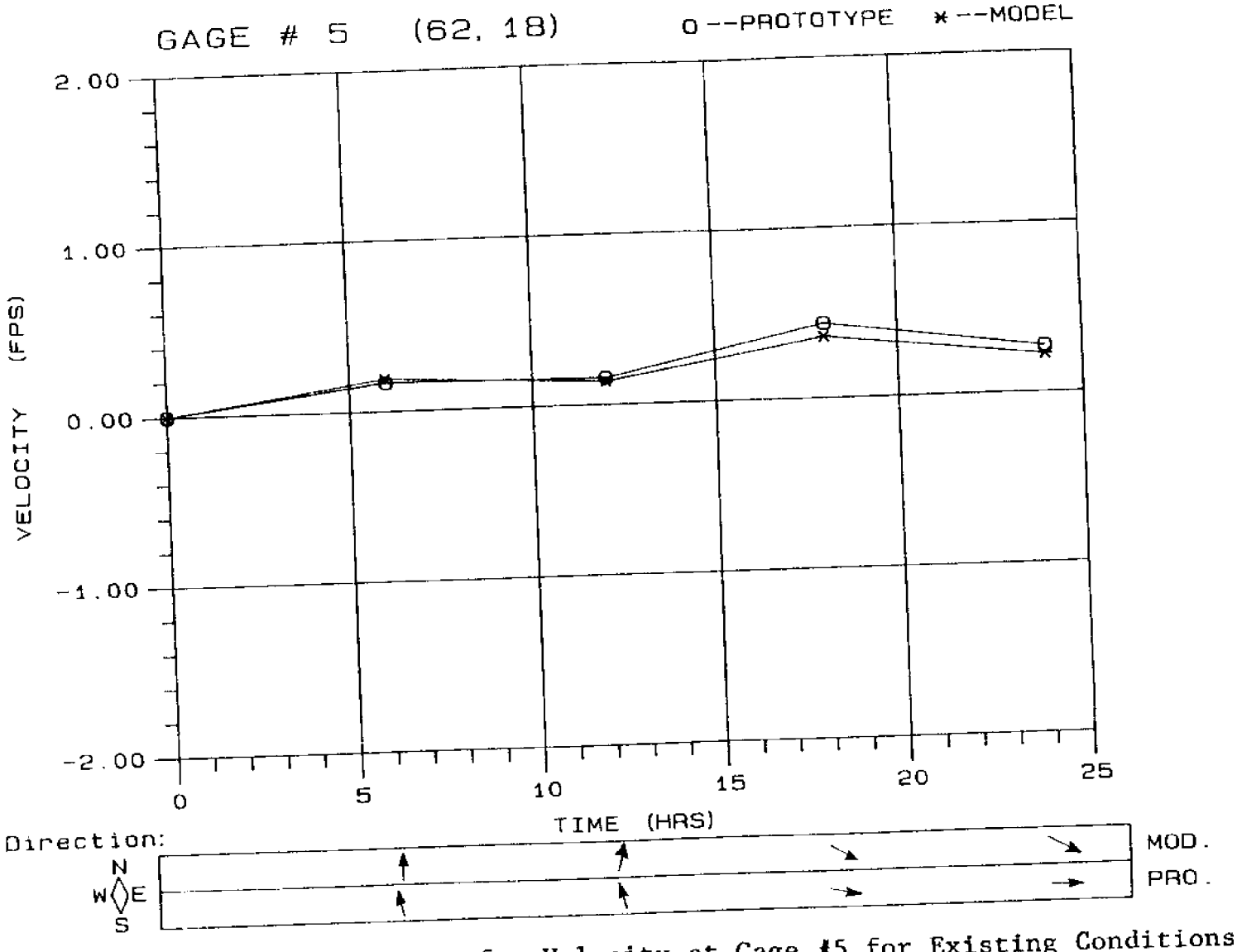

Figure B.5. Calibration Curve for Velocity at Gage #5 for Existing Conditions

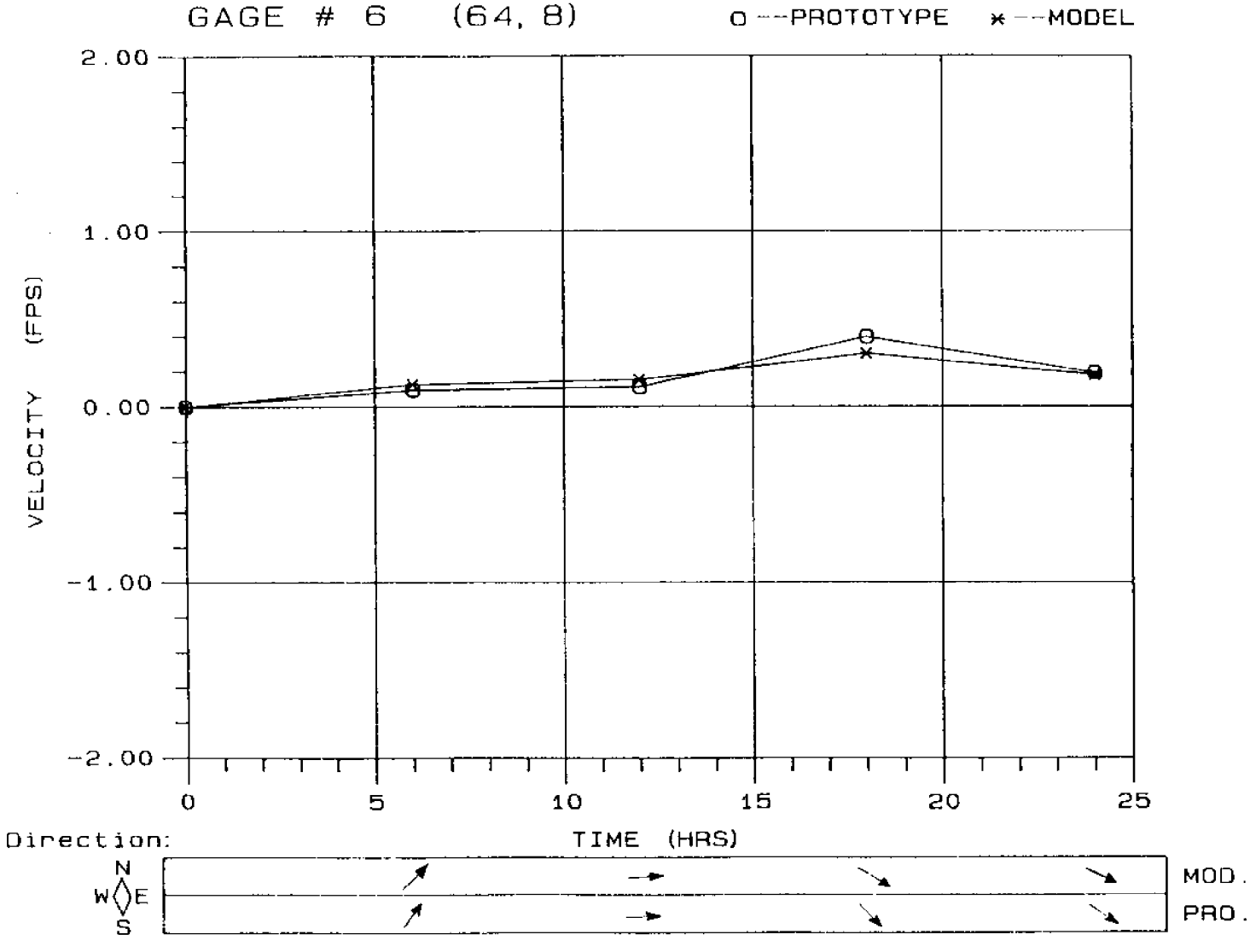

Figure B.6. Calibration Curve for Velocity at Gage #6 for Existing Conditions

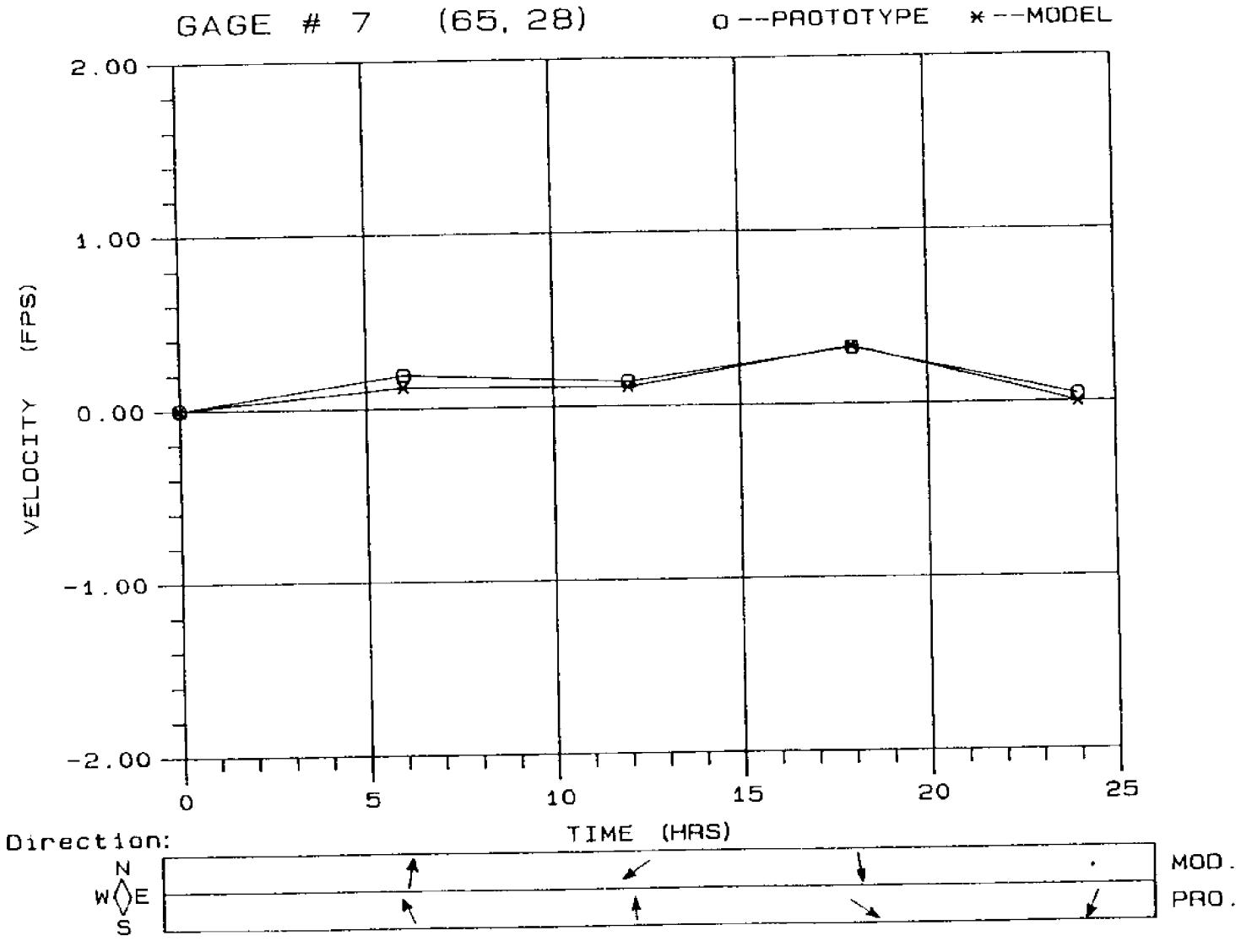

Figure B.7. Calibration Curve for Velocity at Gage #7 for Existing Conditions

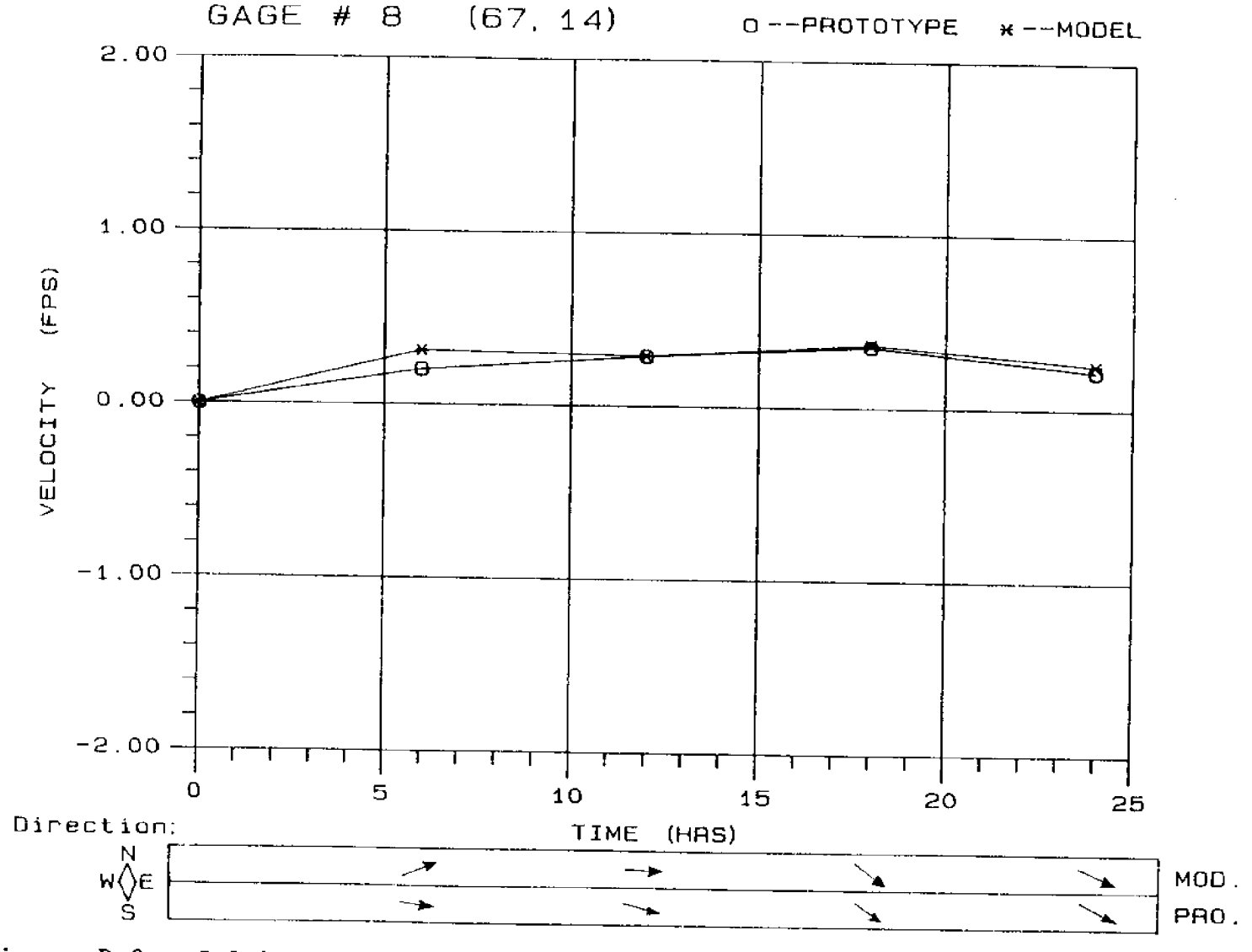

Figure B.8. Calibration Curve for Velocity at Gage #8 for Existing Conditions

APPENDIX C

Comparison of Water Surface Elevation for Existing Conditions and for a 45-Foot Channel

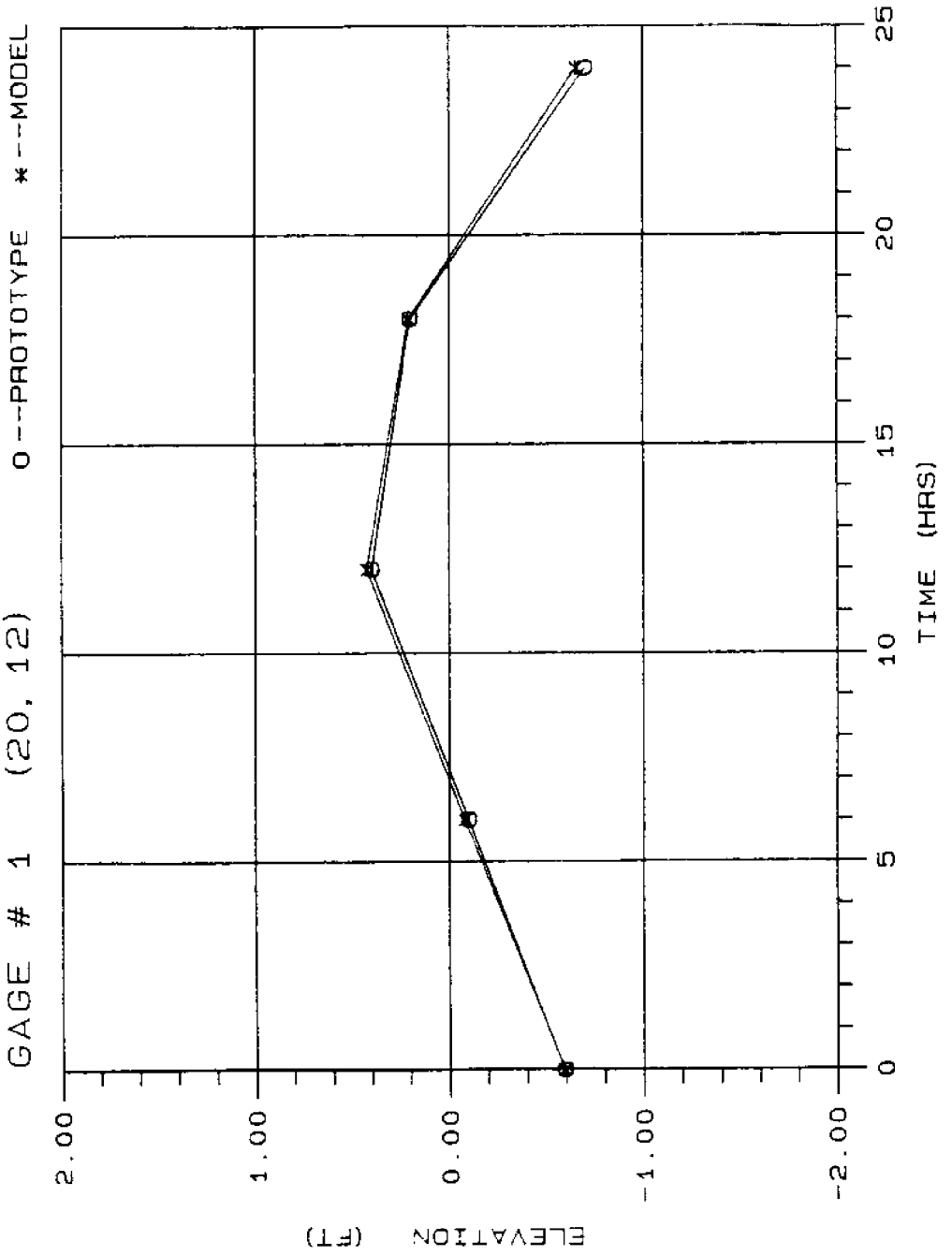

Figure C.1. Comparison Curve for Water Surface Elevation at Gage #1 for Channel Deepened to 45 Feet

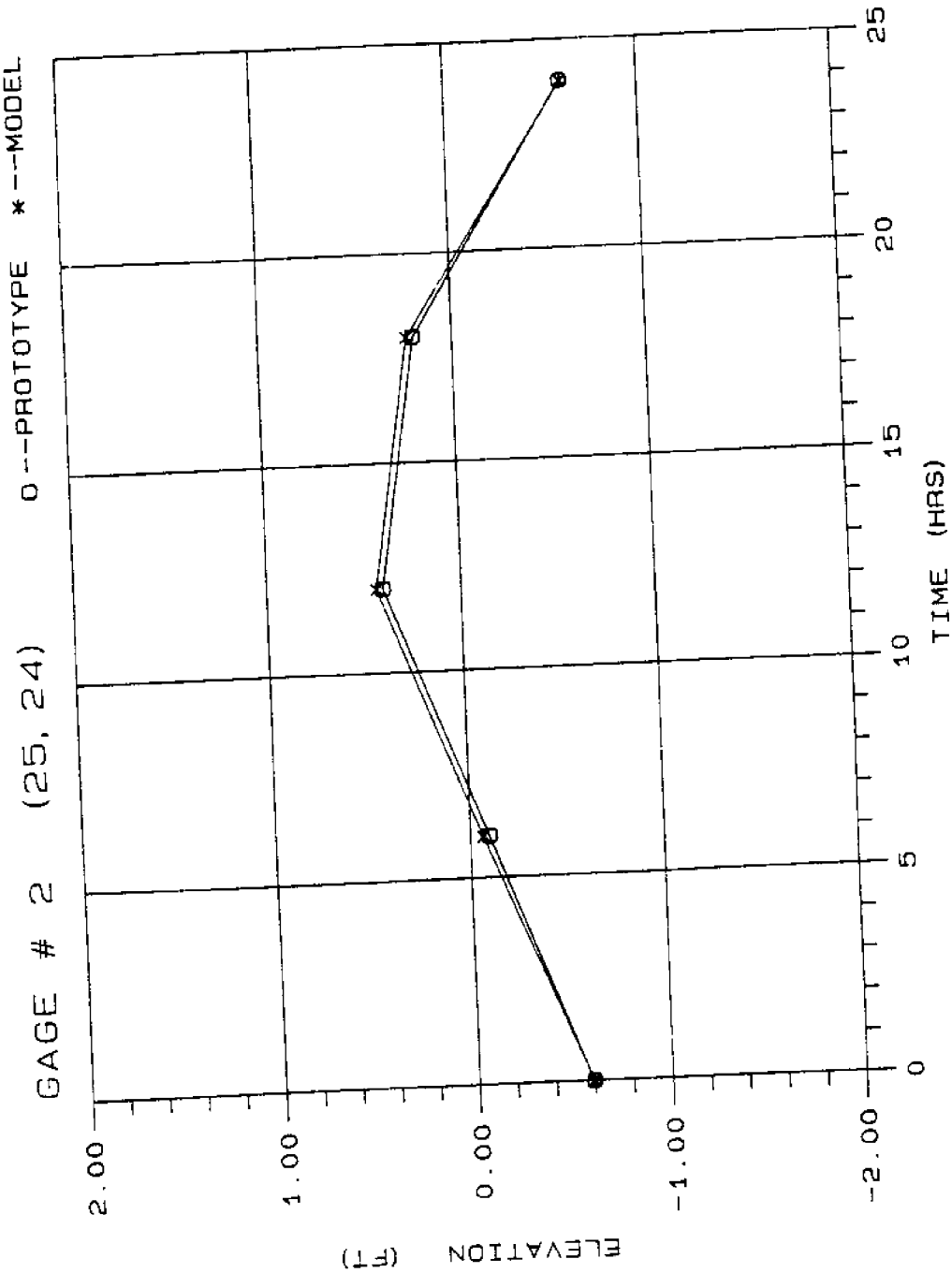

Figure C.2. Comparison Curve for Water Surface Elevation at Gage #2 for Channel Deepened to 45 Feet

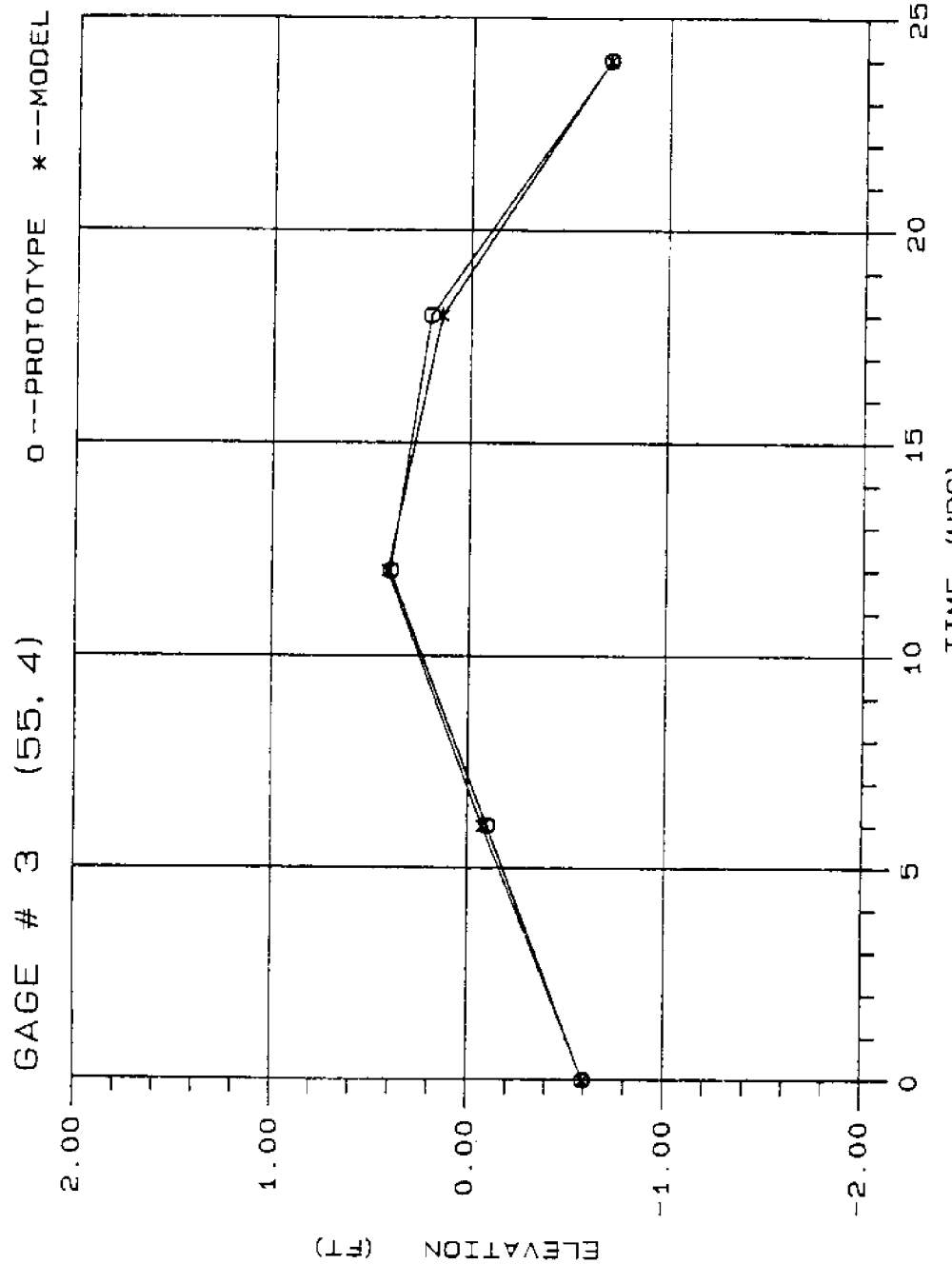

Figure C.3. Comparison Curve for Water Surface Elevation at Gage #3 for Channel Deepened to 45 Feet

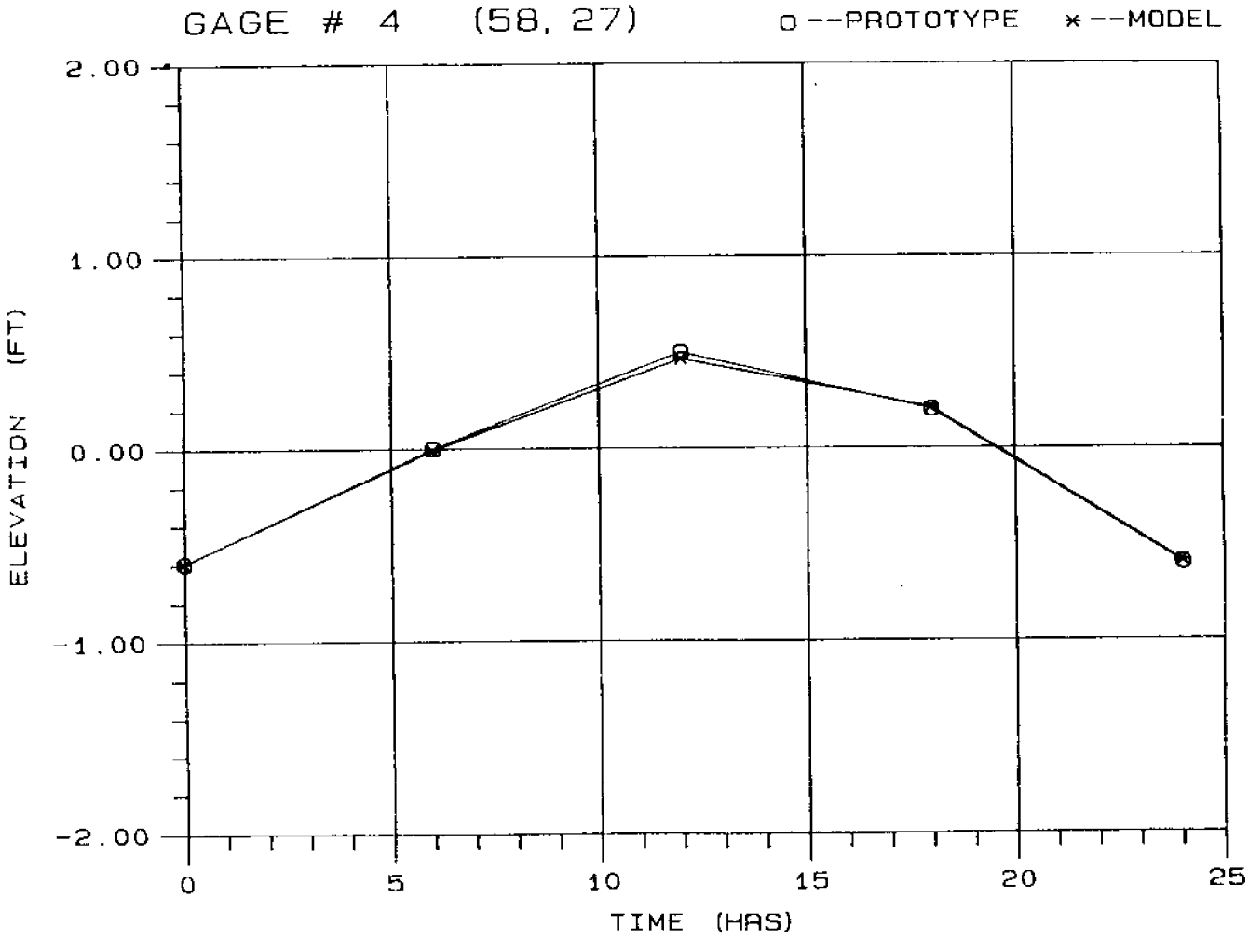

Figure C.4. Comparison Curve for Water Surface Elevation at Gage #4 for Channel Deepened to 45 Feet

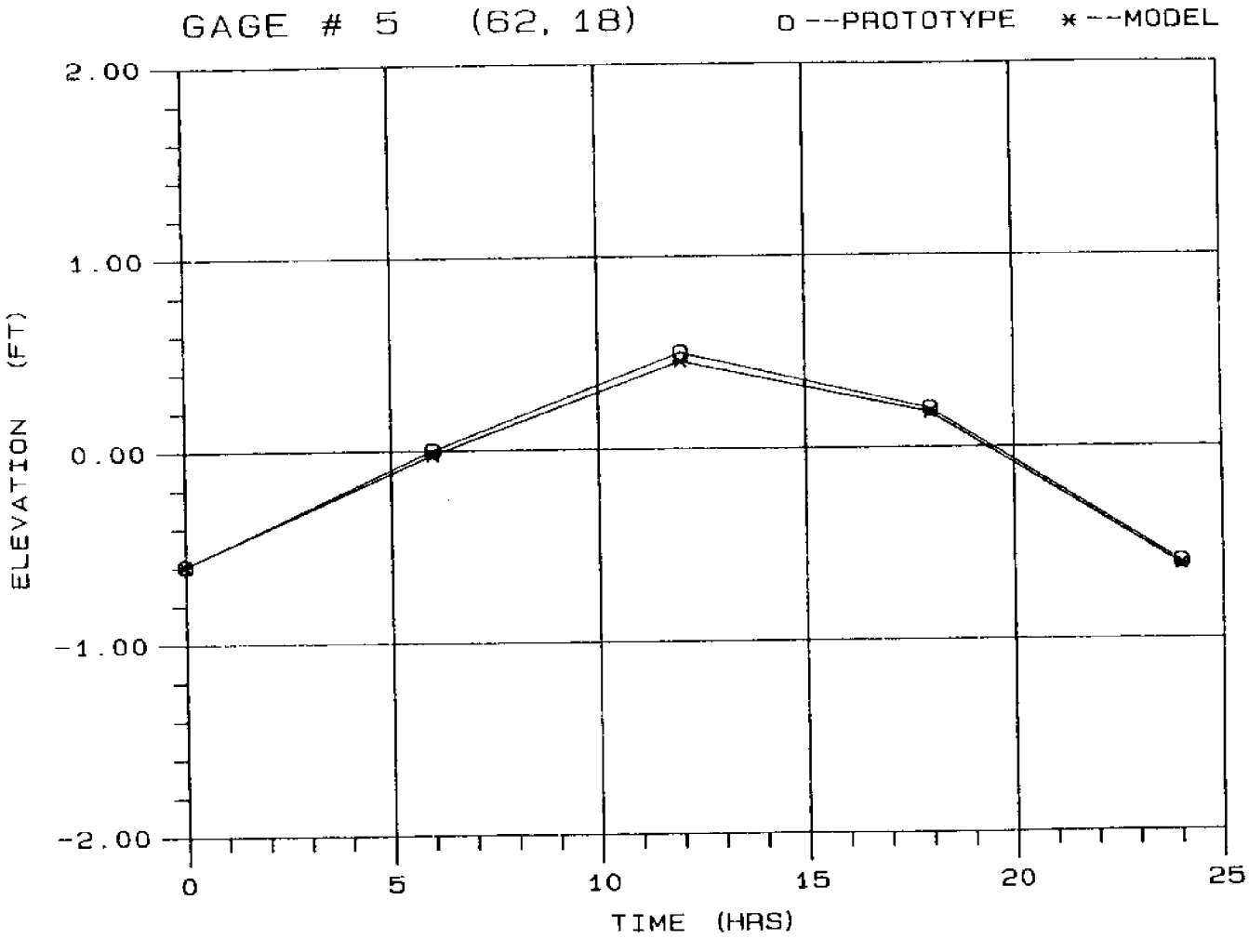

Figure C.5. Comparison Curve for Water Surface Elevation at Gage #5 for Channel Deepened to 45 Feet

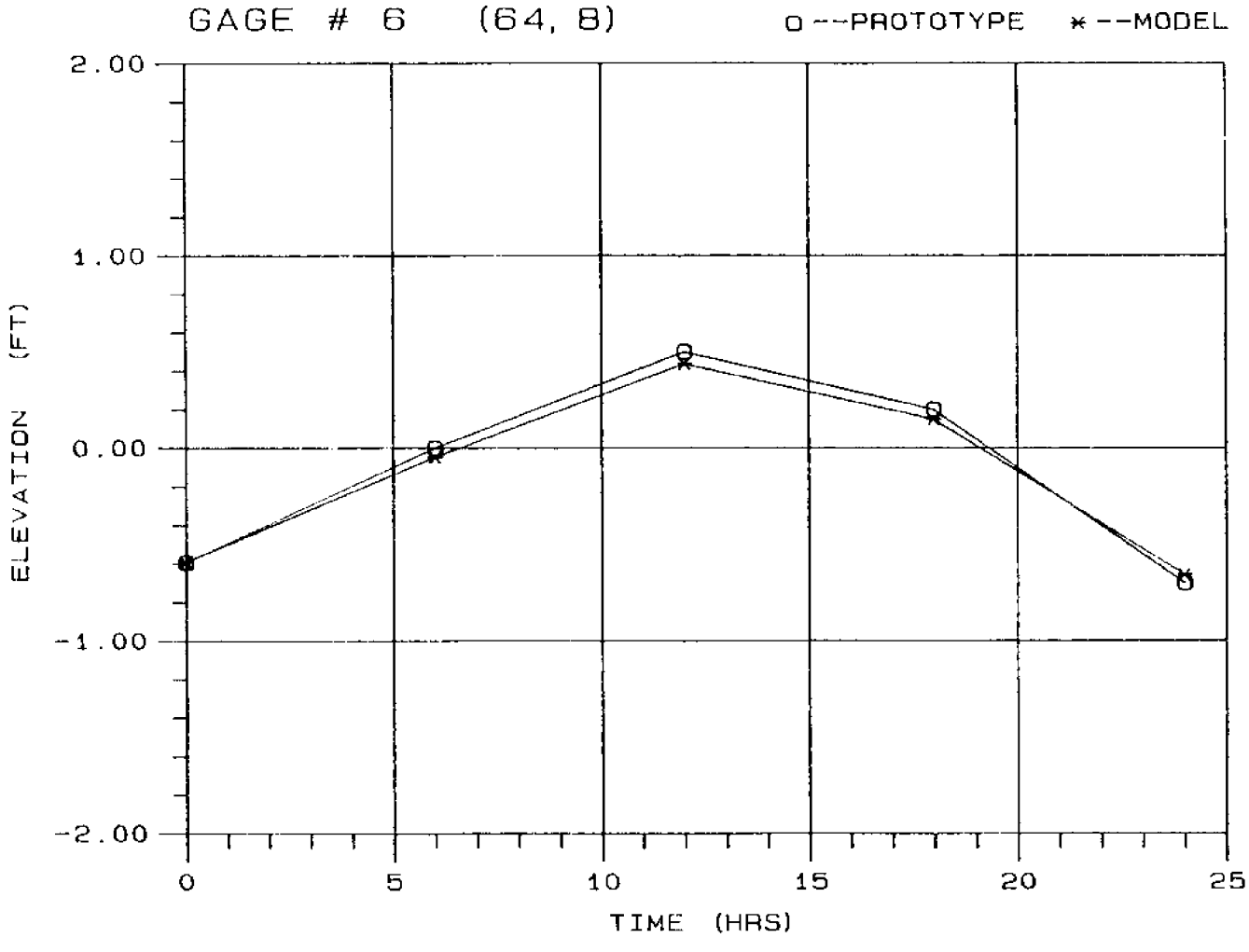

Figure C.6. Comparison Curve for Water Surface Elevation at Gage #6 for Channel Deepened to 45 Feet

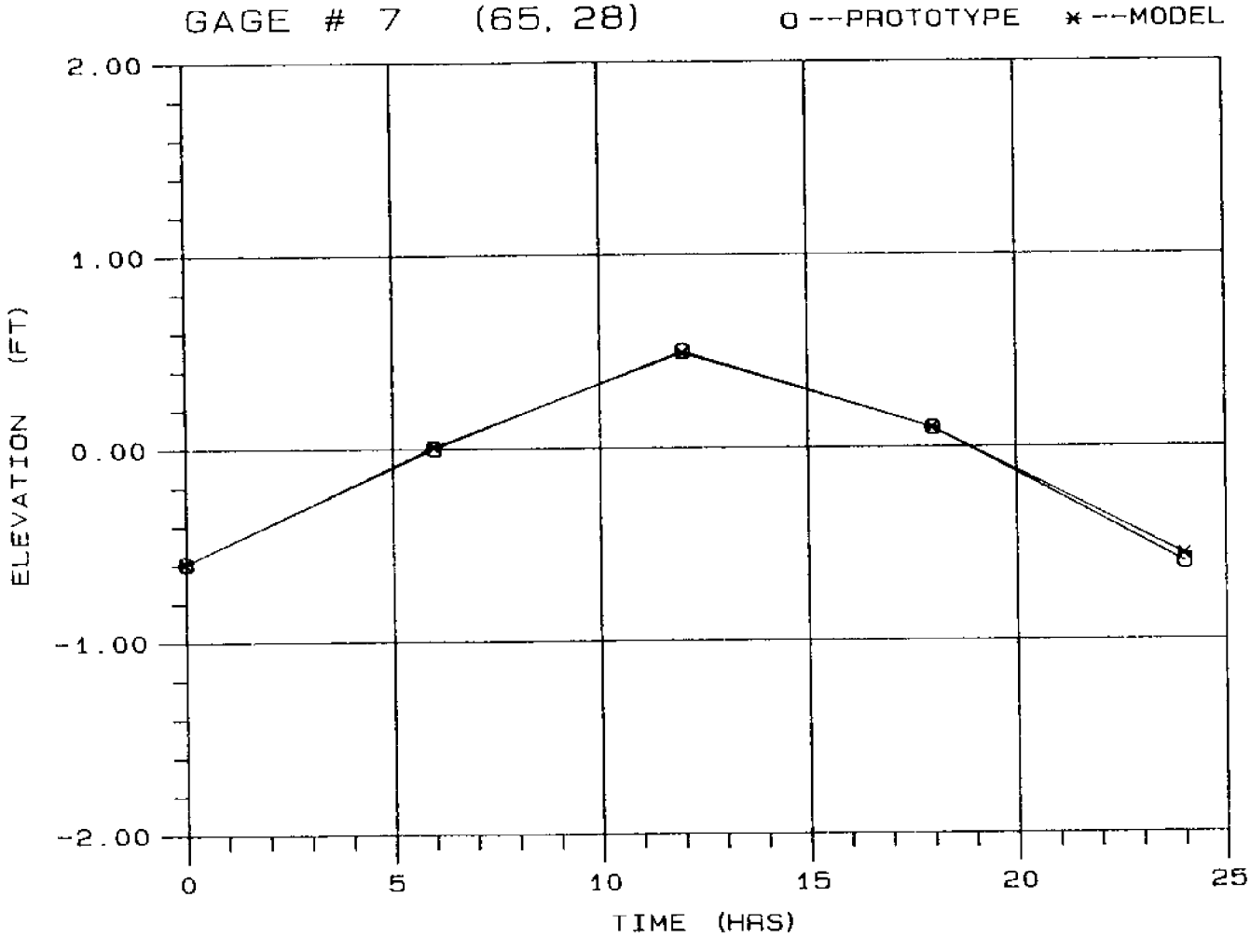

Figure C.7. Comparison Curve for Water Surface Elevation at Gage #7 for Channel Deepened to 45 Feet

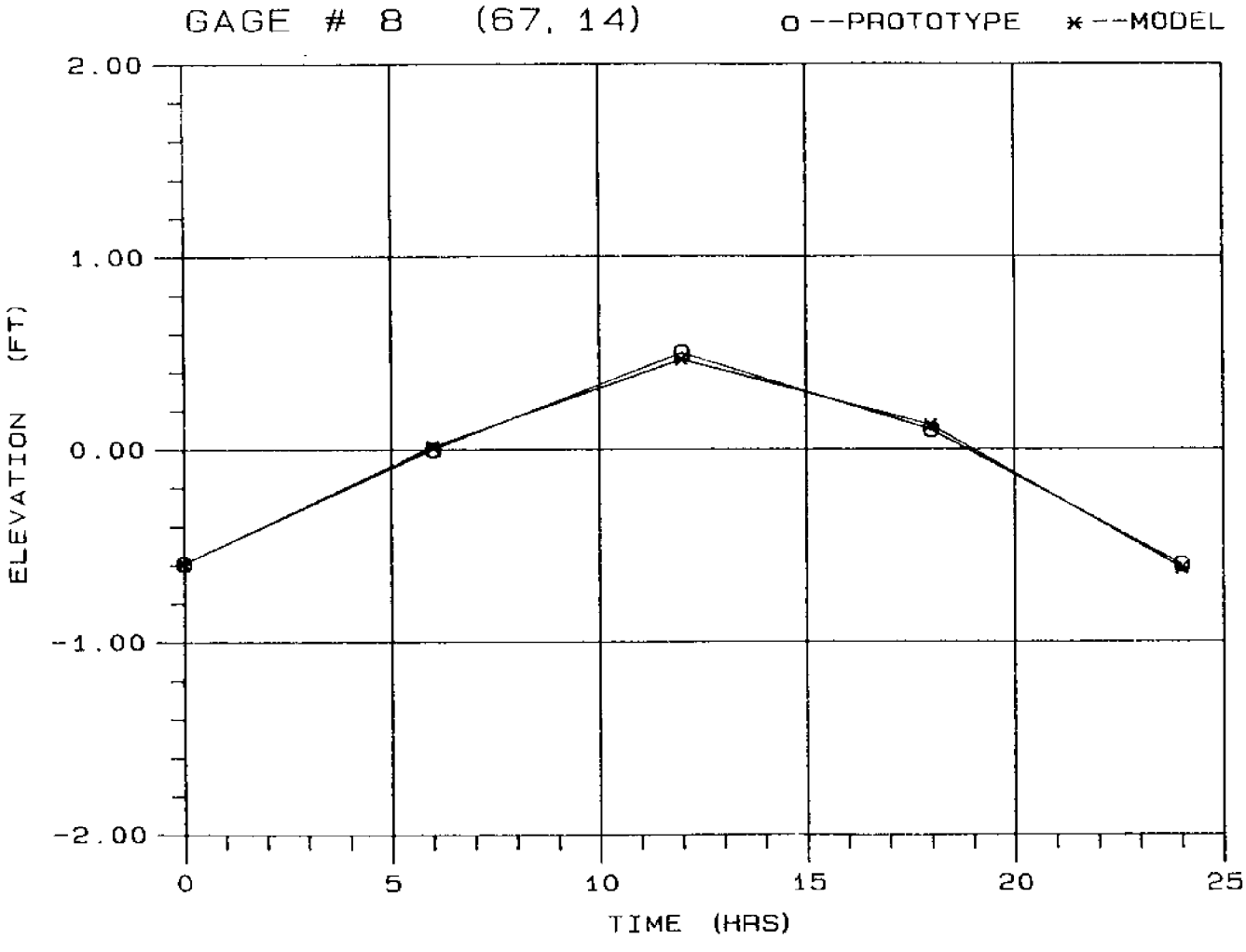

Figure C.8. Comparison Curve for Water Surface Elevation at Gage #8 for Channel Deepened to 45 Feet

APPENDIX D

Comparison of Velocity for Existing Conditions and for a 45-Foot Channel

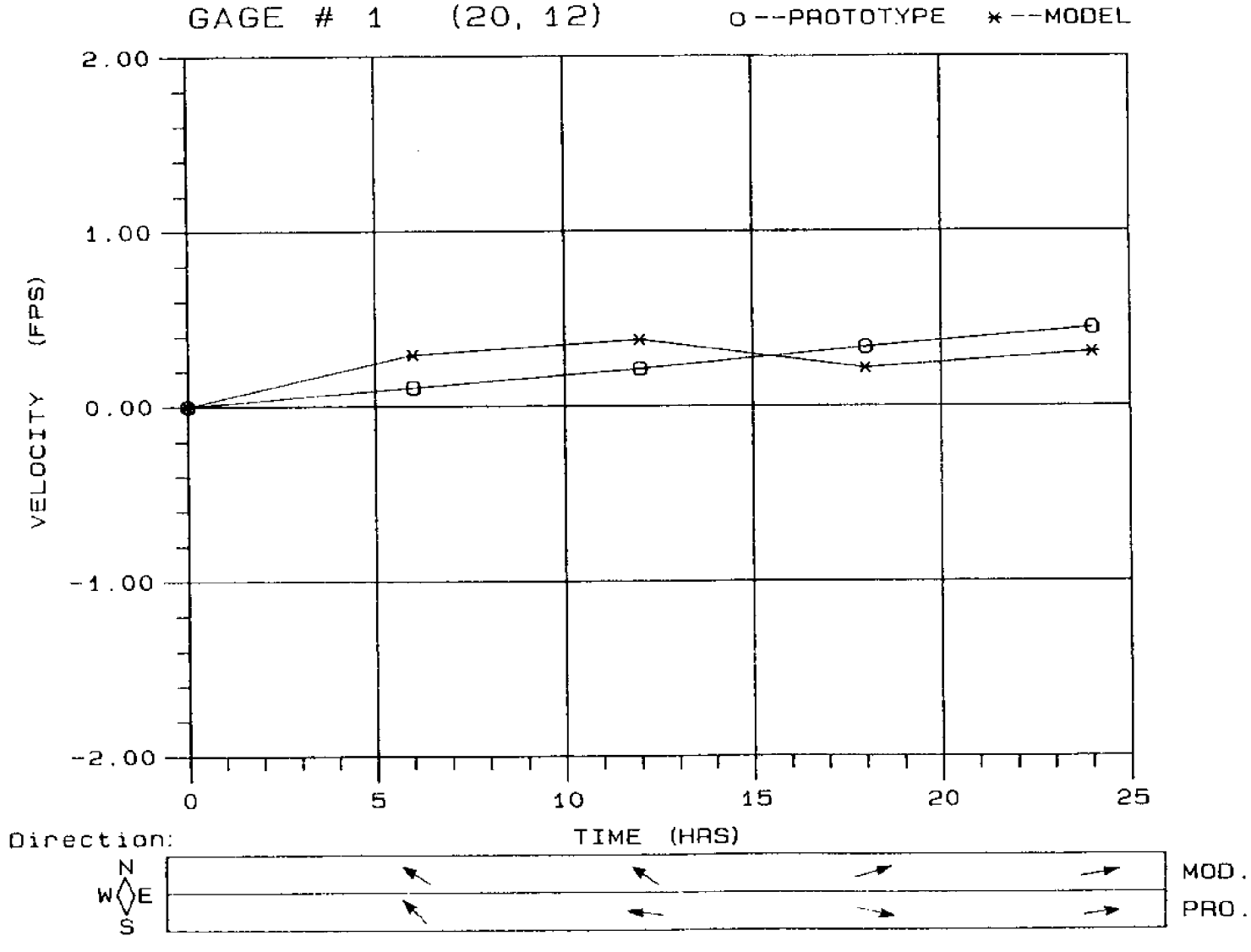

Figure D.1. Comparison Curve for Velocity at Gage #1 for Channel Deepened to 45 Feet

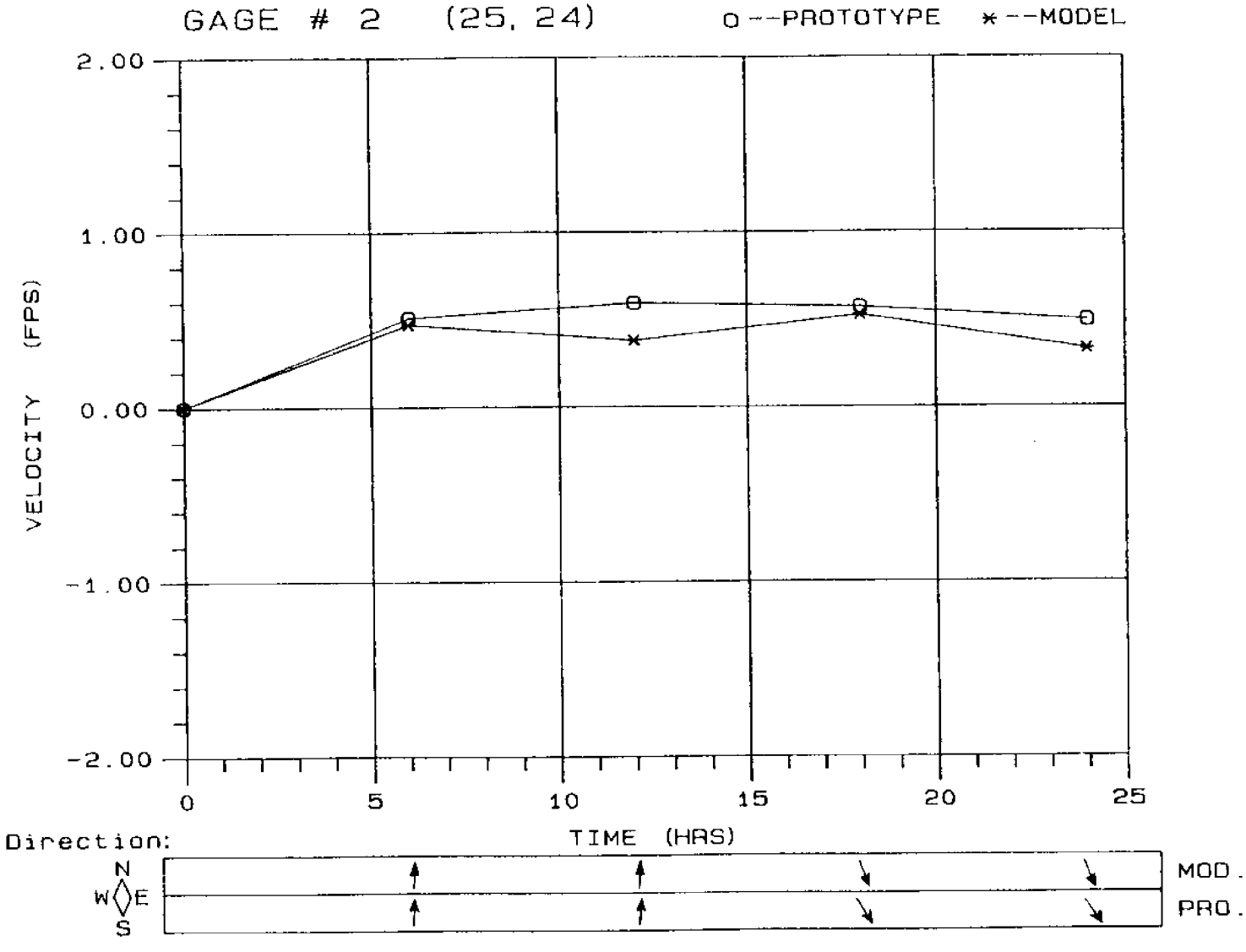

Figure D.2. Comparison Curve for Velocity at Gage #2 for Channel Deepened to 45 Feet

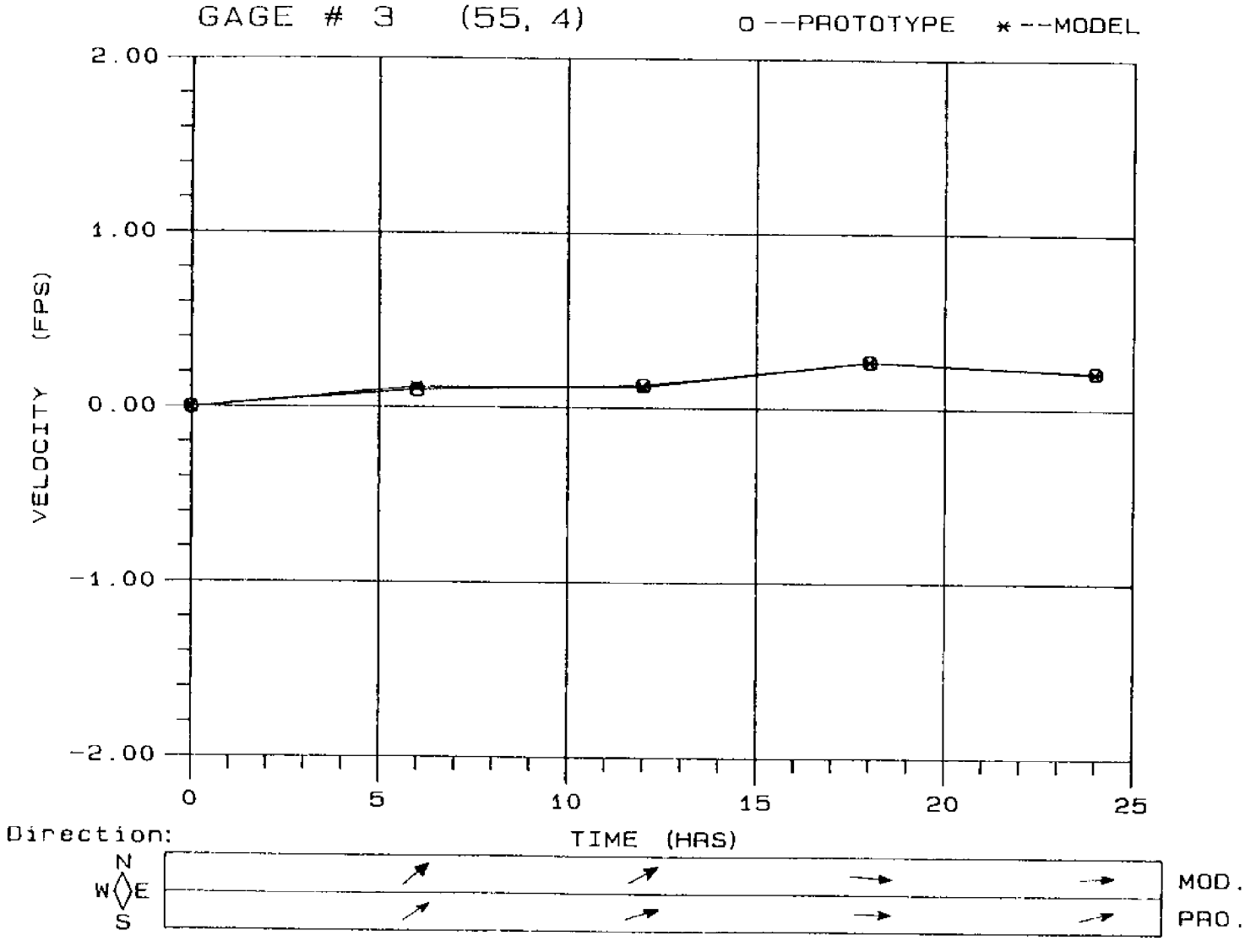

Figure D.3. Comparison Curve for Velocity at Gage #3 for Channel Deepened to 45 Feet

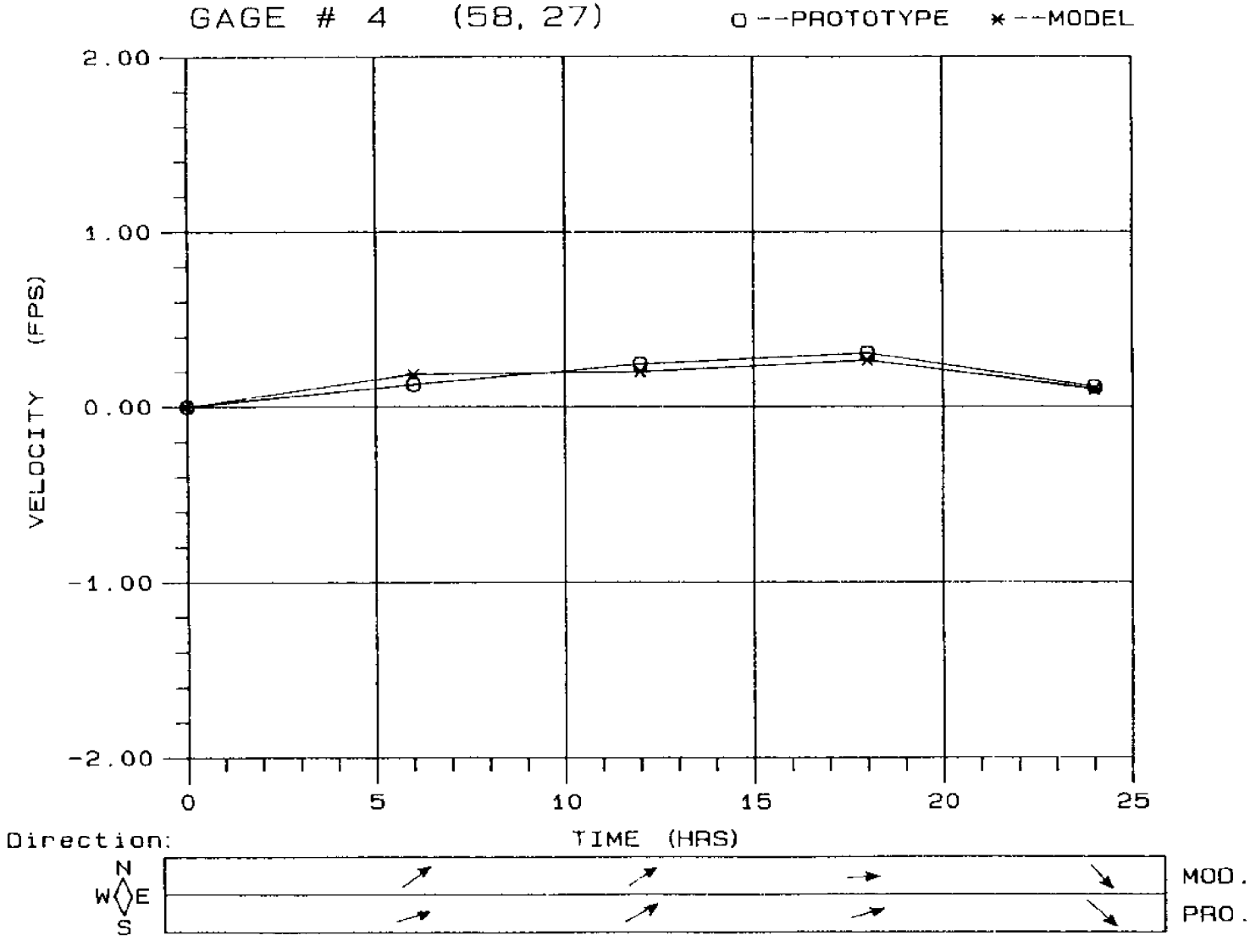

Figure D.4. Comparison Curve for Velocity at Gage #4 for Channel Deepened to 45 Feet

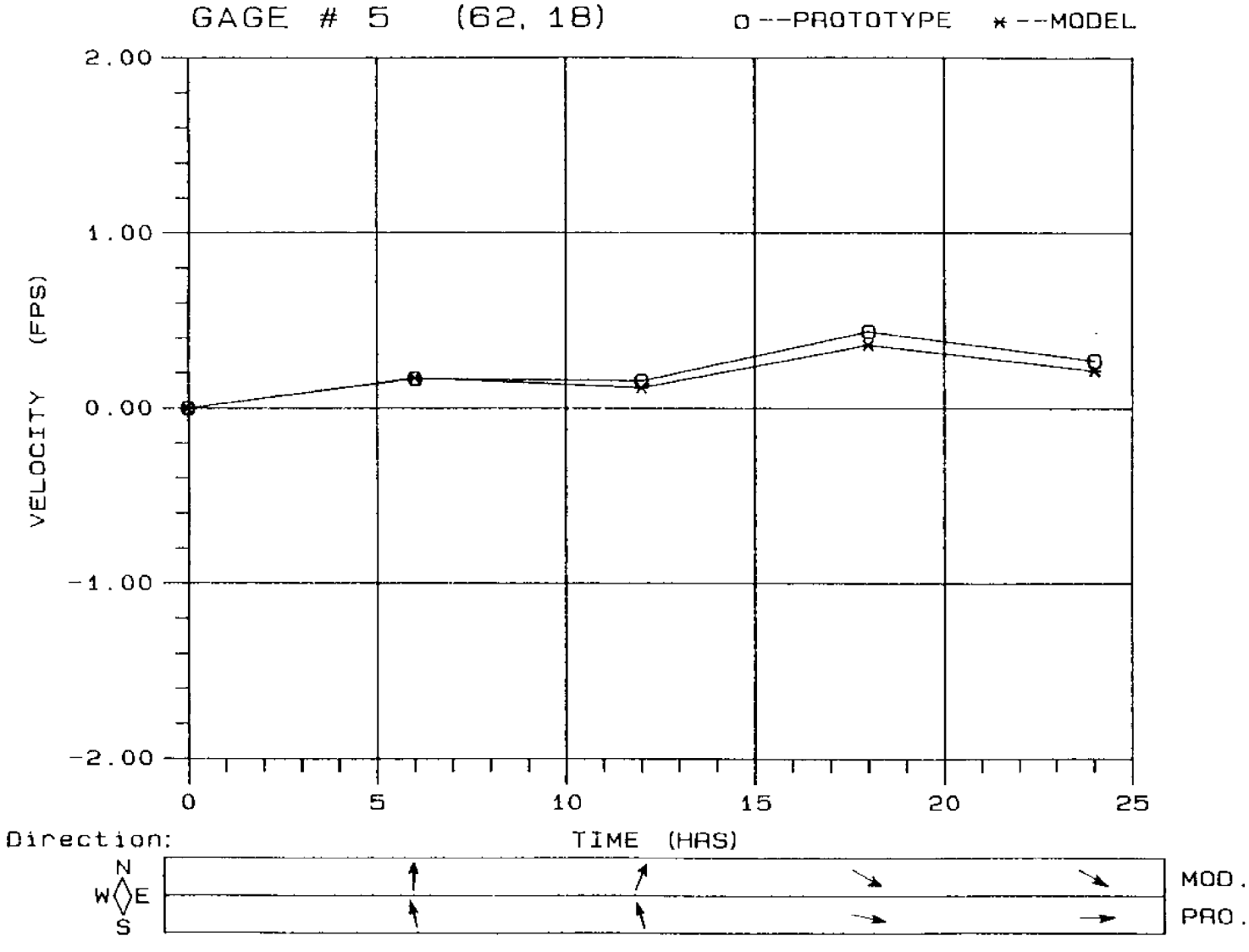

Figure D.5. Comparison Curve for Velocity at Gage #5 for Channel Deepened to 45 Feet

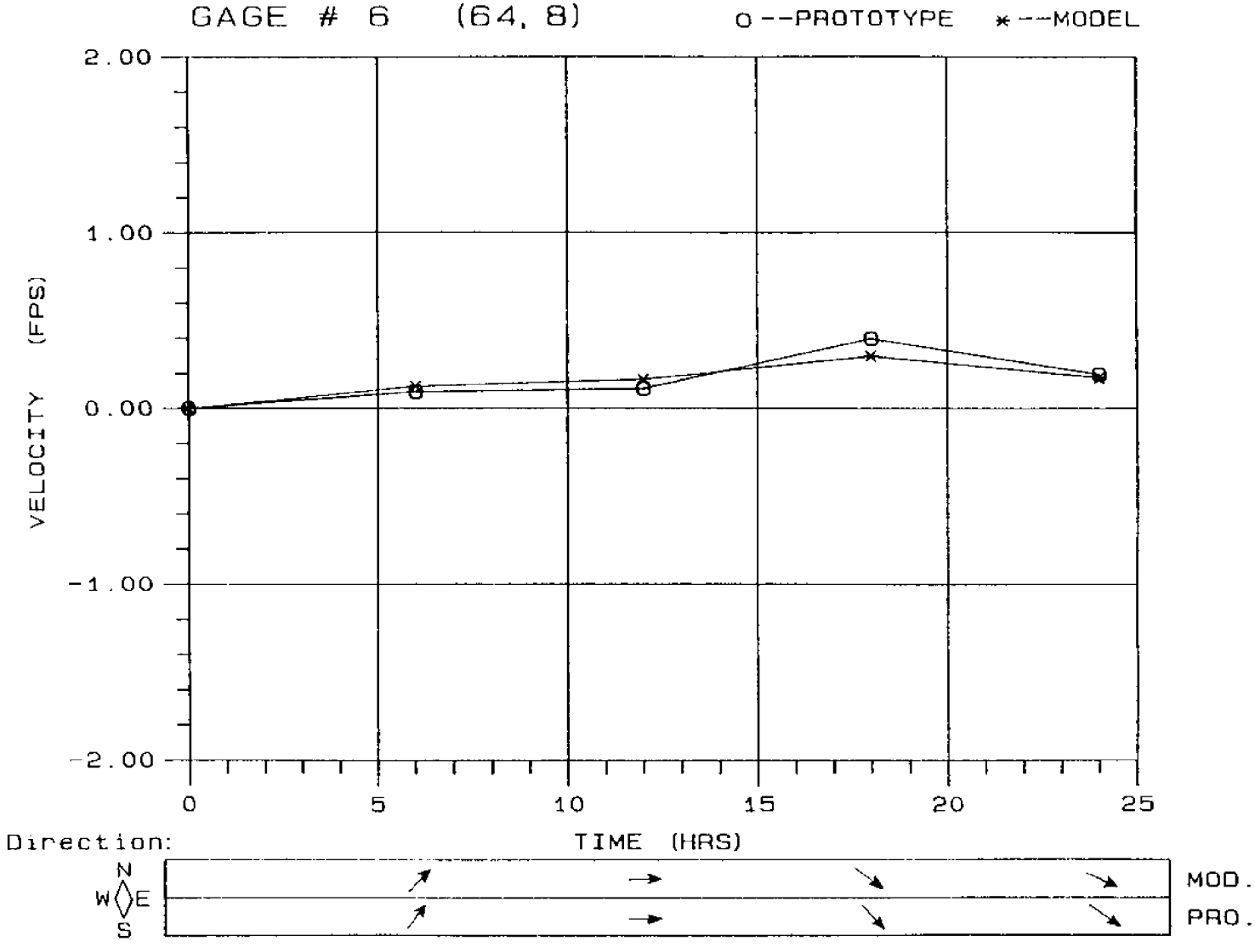

Figure D.6. Comparison Curve for Velocity at Gage #6 for Channel Deepened to 45 Feet

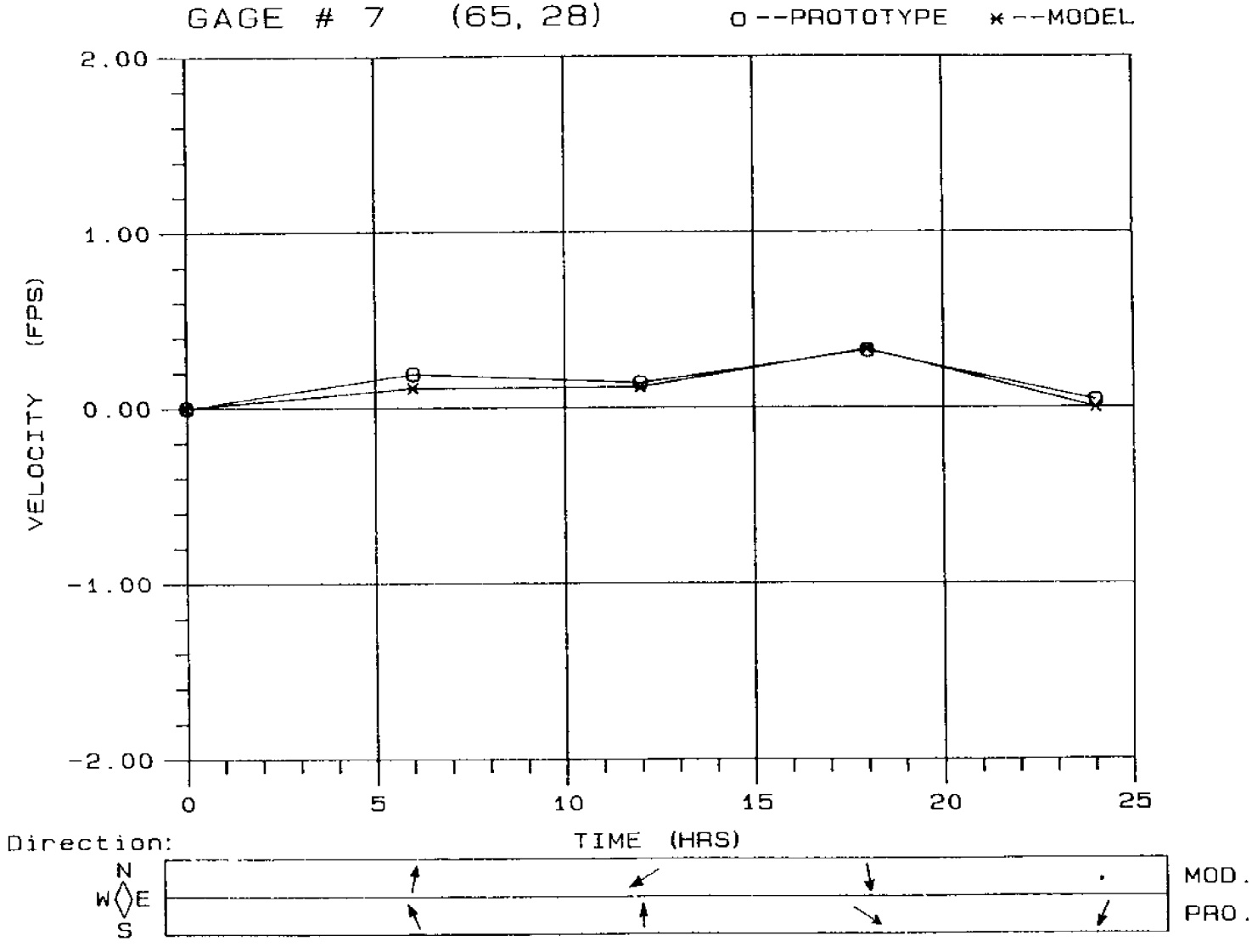

Figure D.7. Comparison Curve for Velocity at Gage #7 for Channel Deepened to 45 Feet

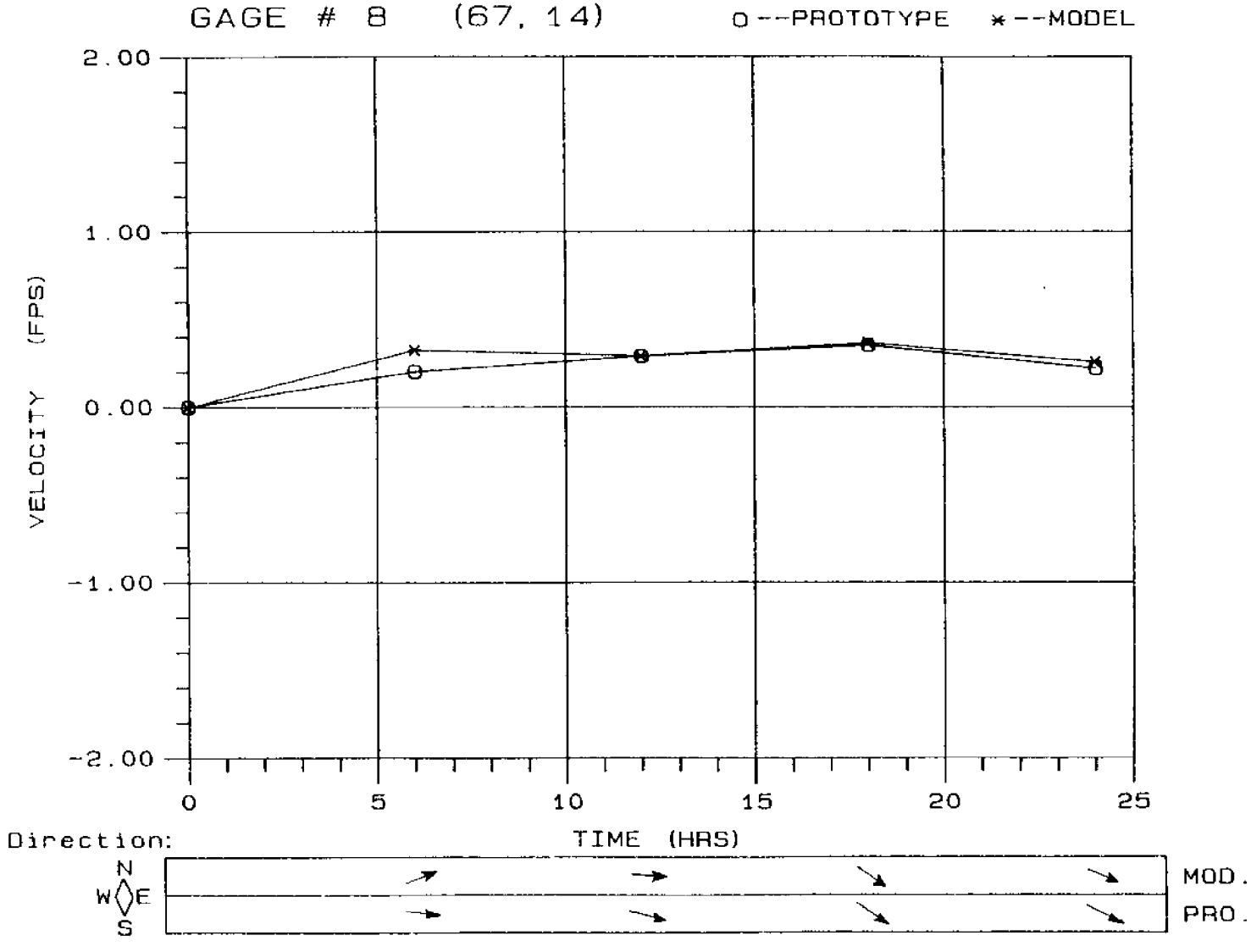

Figure D.8. Comparison Curve for Velocity at Gage #8 for Channel Deepened to 45 Feet

APPENDIX E

General Circulation Patterns

for Existing Conditions

(26 Foot Channel, 9 Knots N-W Wind)

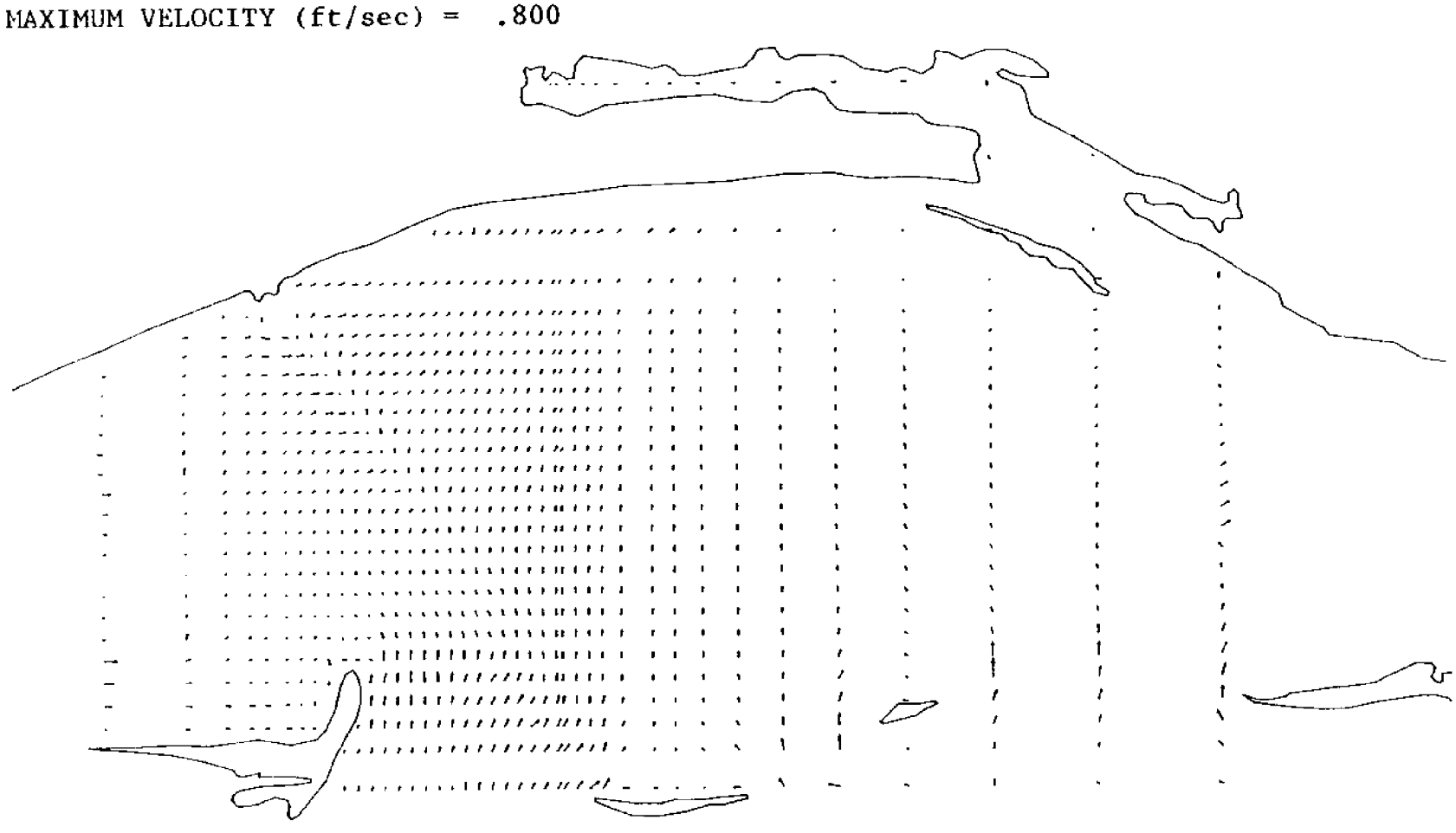

Figure E.1. Circulation Pattern for Existing Conditions at T = 2 Hours

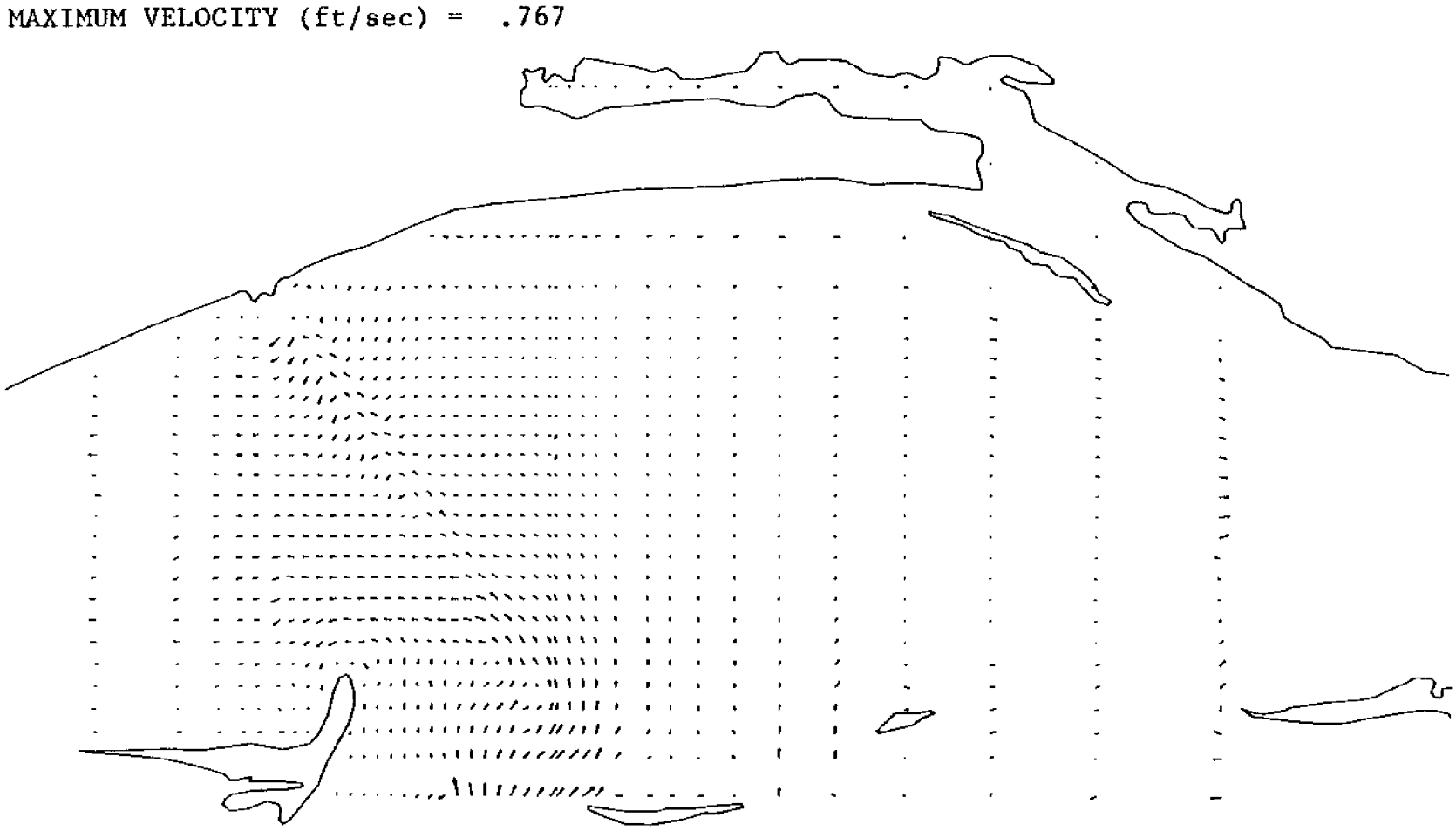

Figure E.2. Circulation Pattern for Existing Conditions at T = 4 Hours

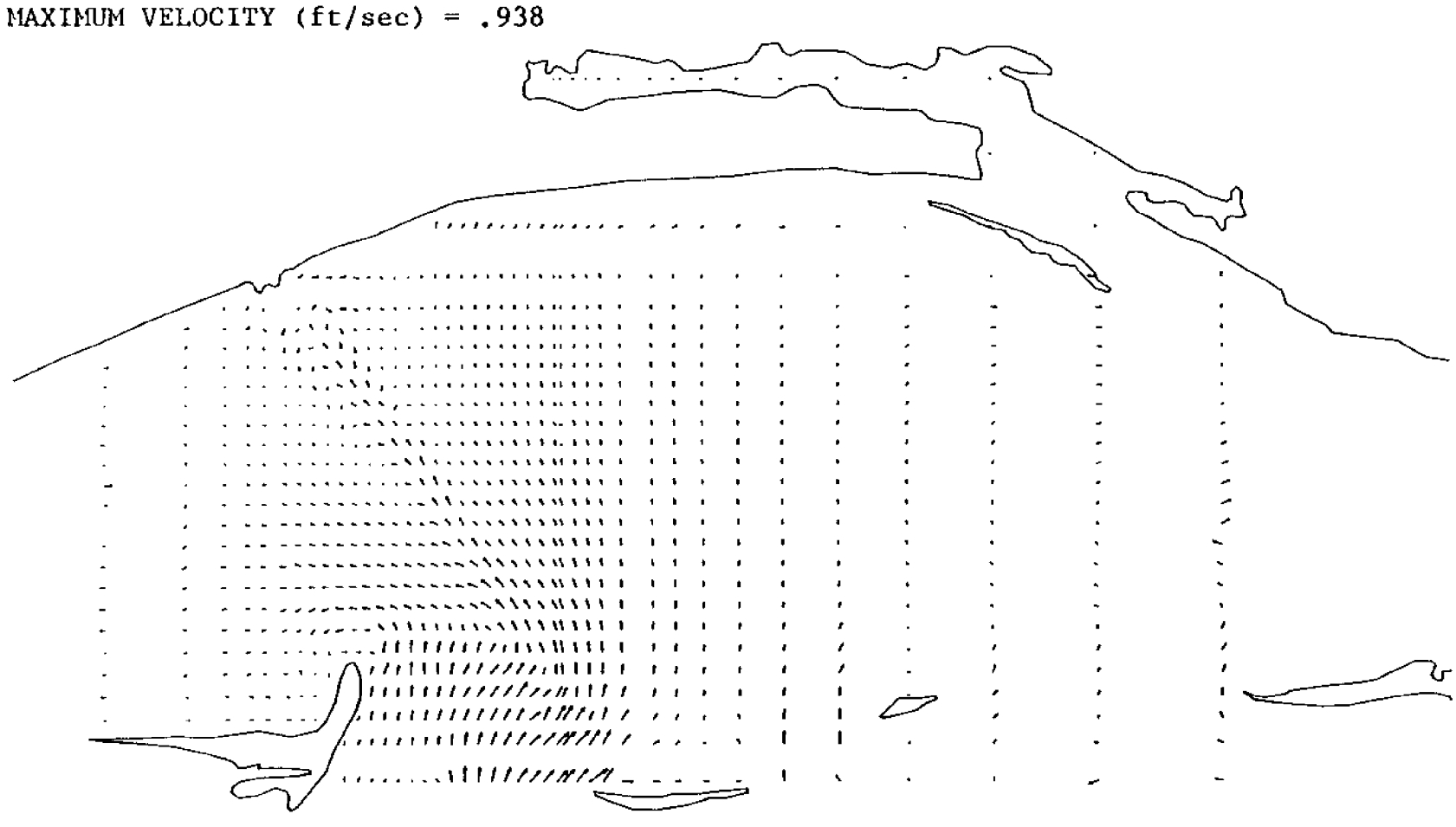

Figure E.3. Circulation Pattern for Existing Conditions at T = 6 Hours

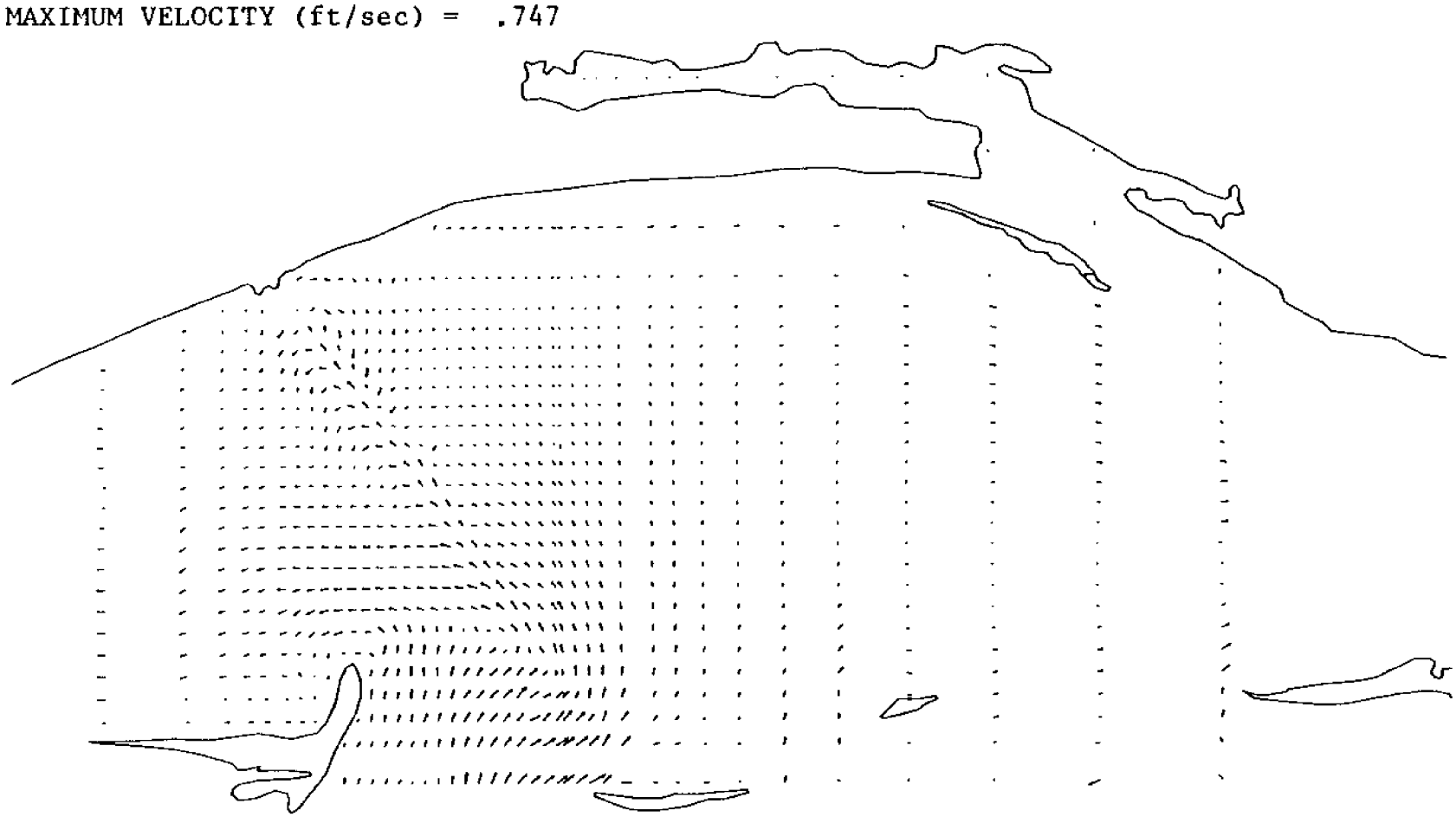

Figure E.4. Circulation Pattern for Existing Conditions at T = 8 Hours

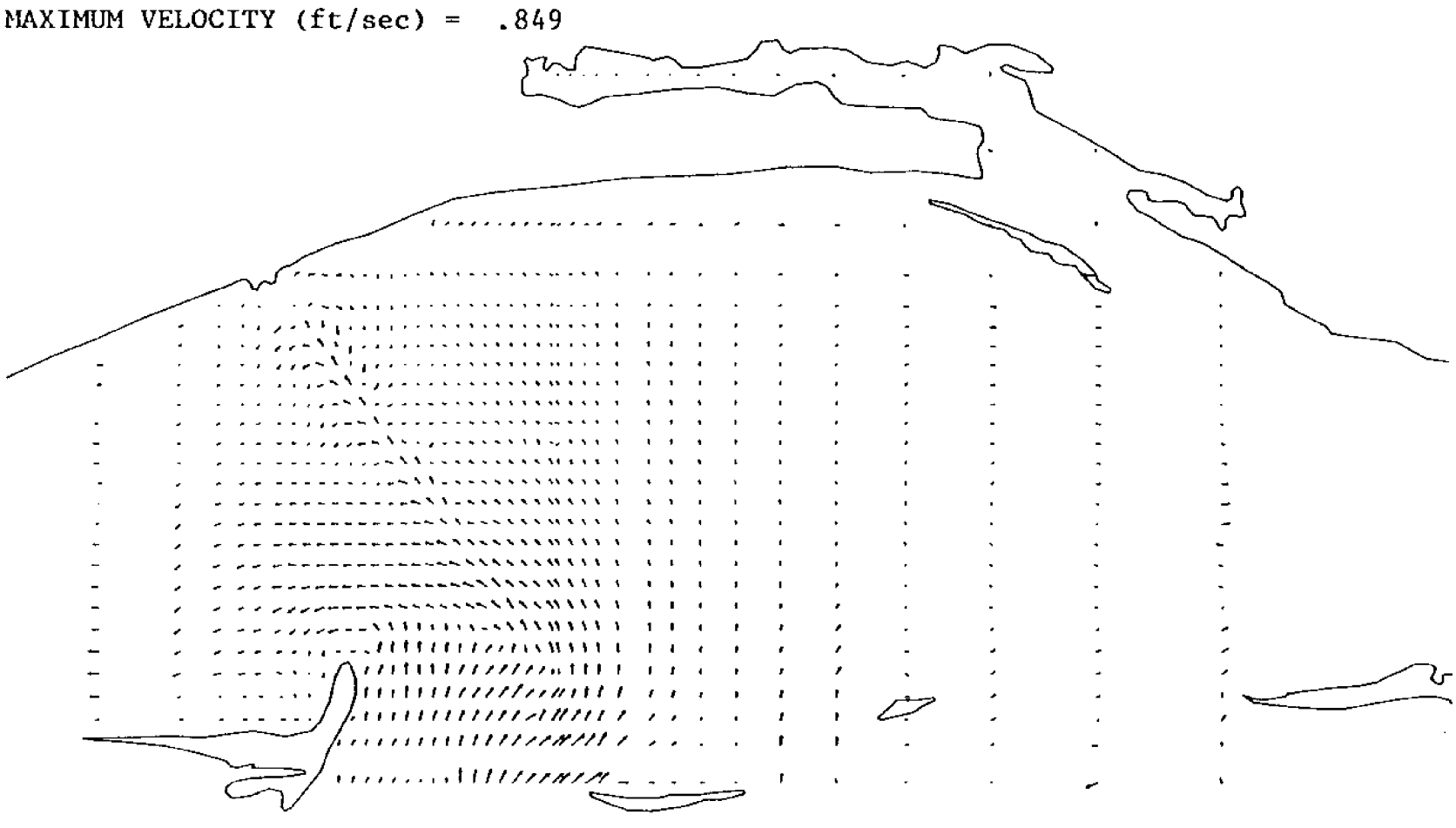

Figure E.5. Circulation Pattern for Existing Conditions at T = 10 Hours

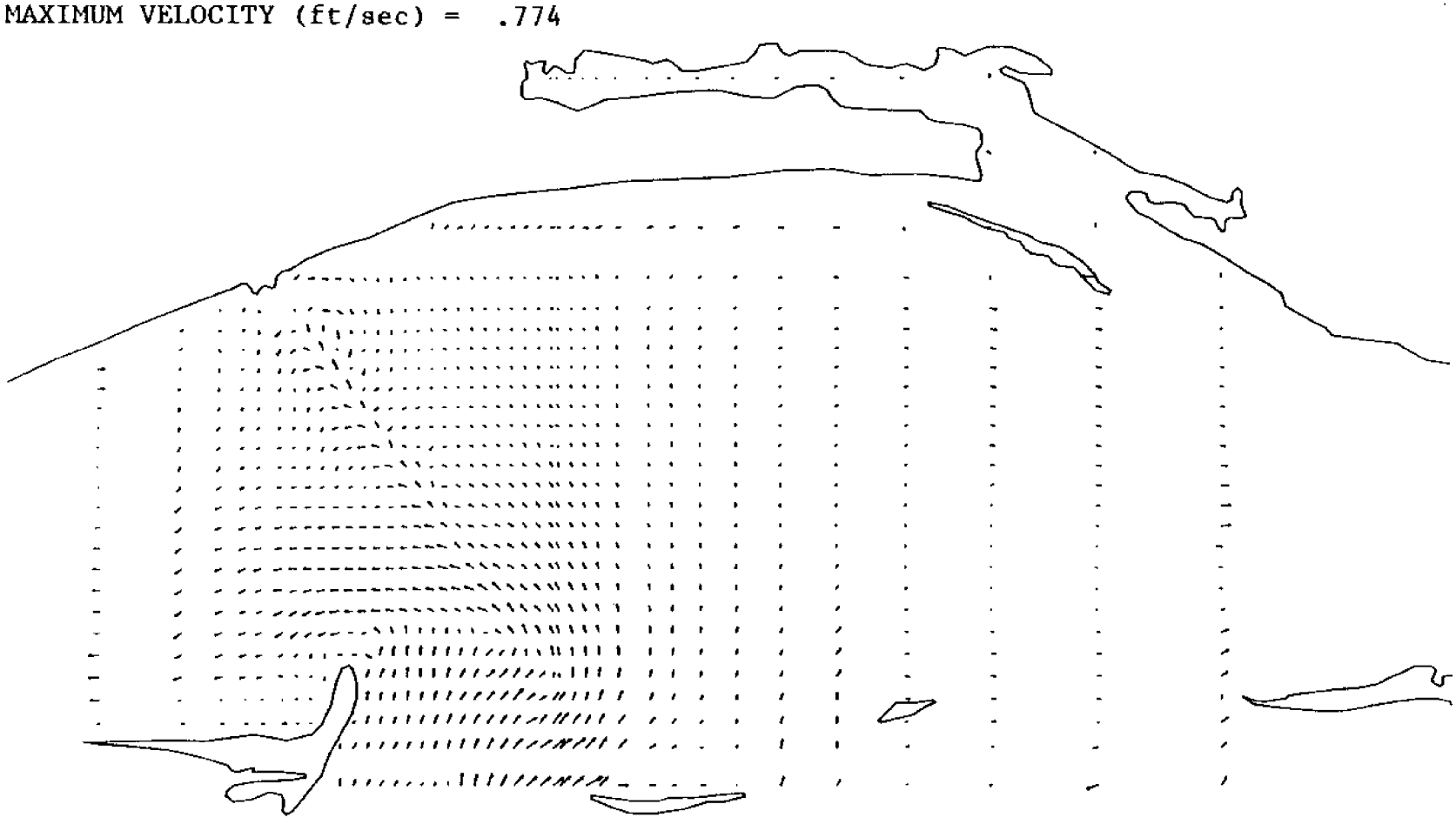

Figure E.6. Circulation Pattern for Existing Conditions at T = 12 Hours

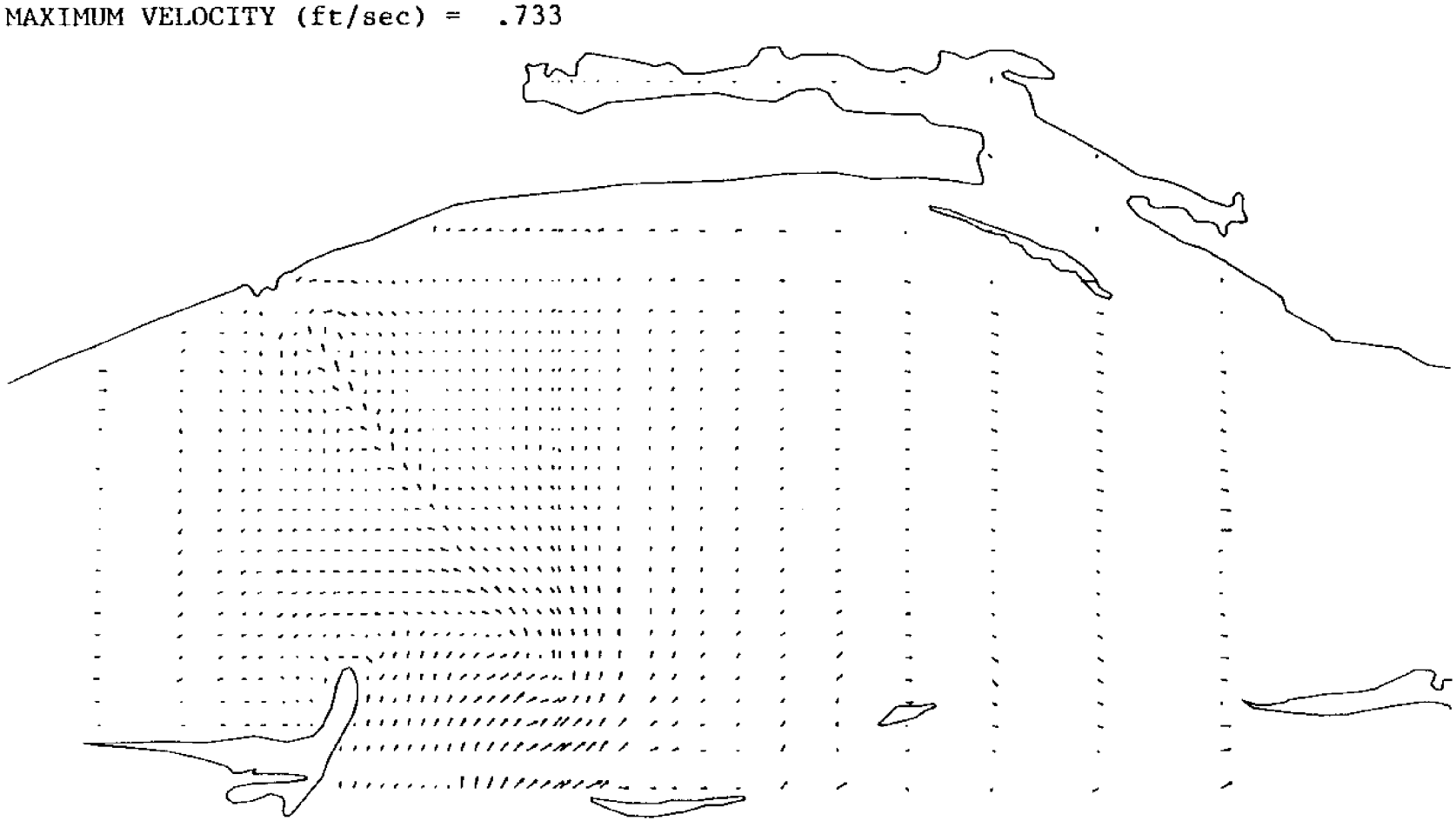

Figure E.7. Circulation Pattern for Existing Conditions at T = 14 Hours

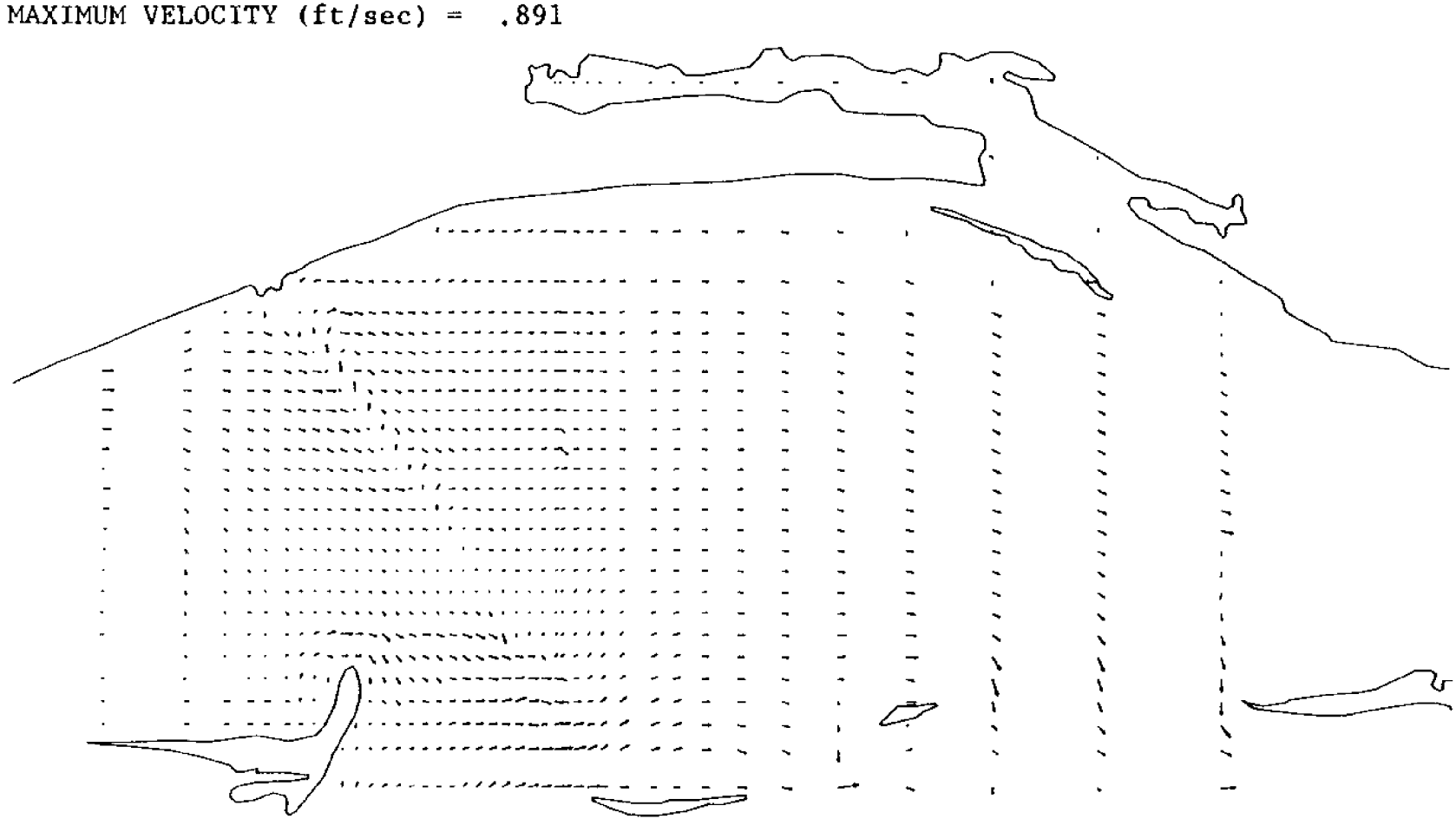

Figure E.8. Circulation Pattern for Existing Conditions at T = 16 Hours

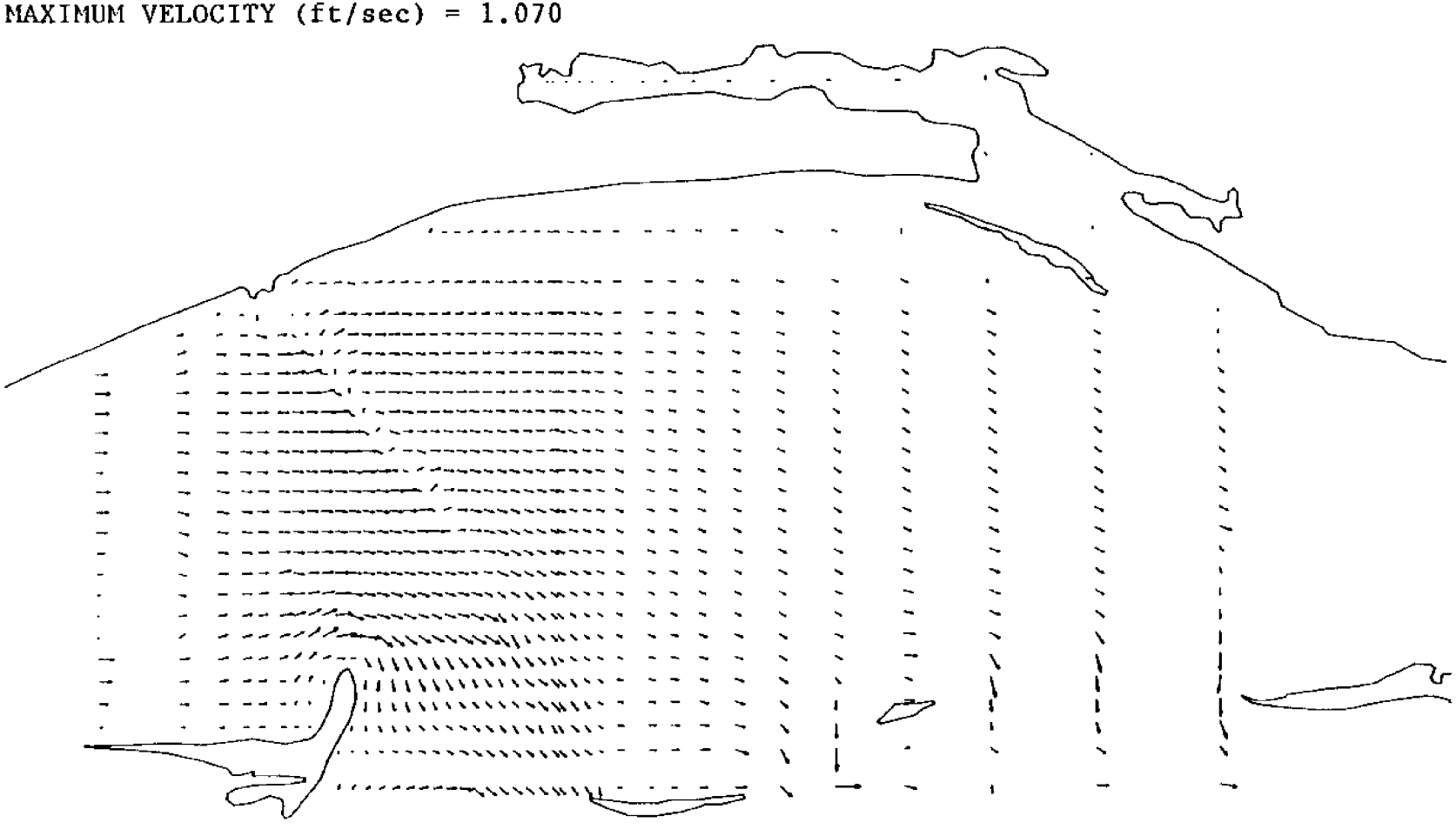

Figure E.9. Circulation Pattern for Existing Conditions at T = 18 Hours

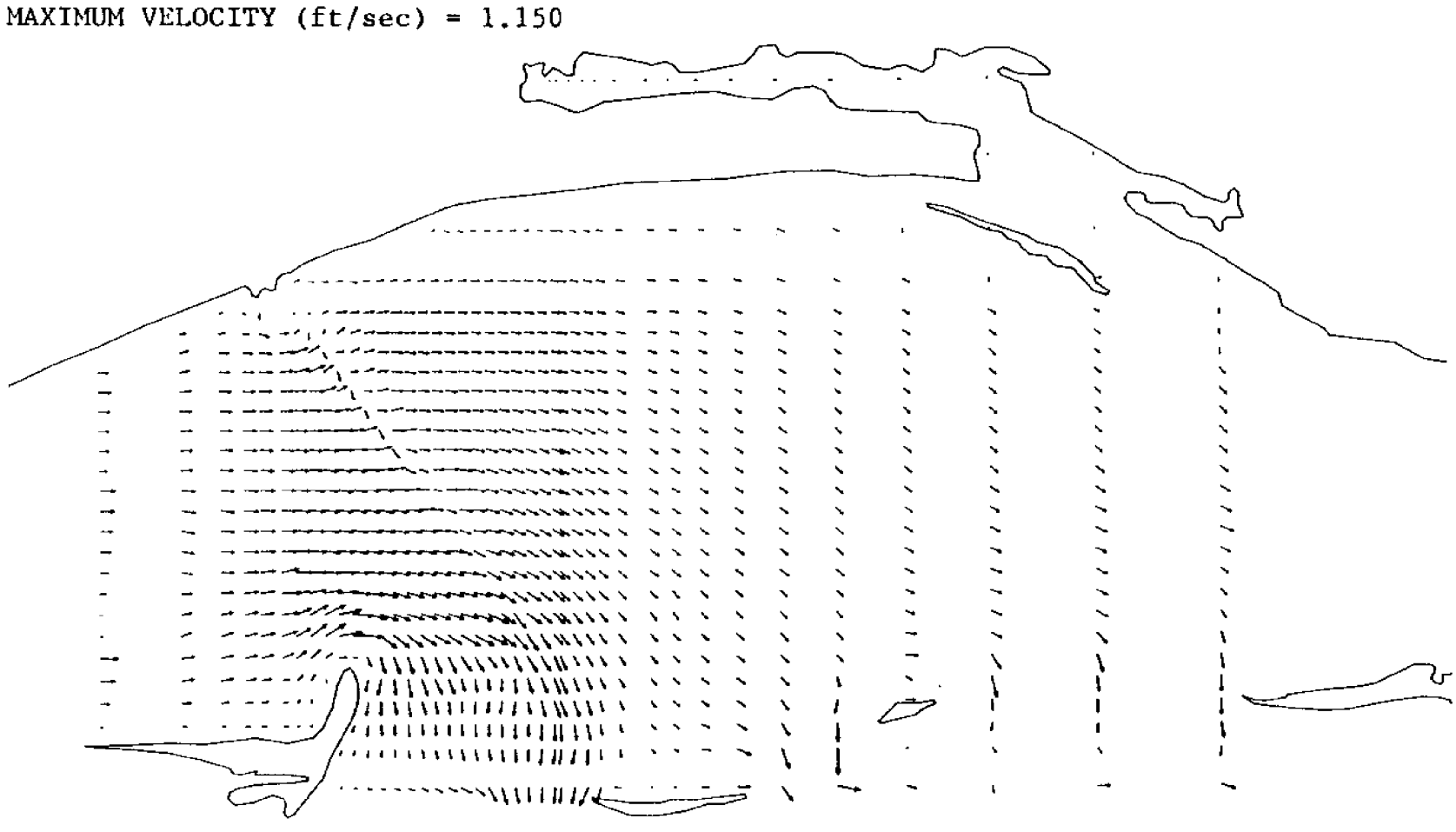

Figure E.10. Circulation Pattern for Existing Conditions at T = 20 Hours

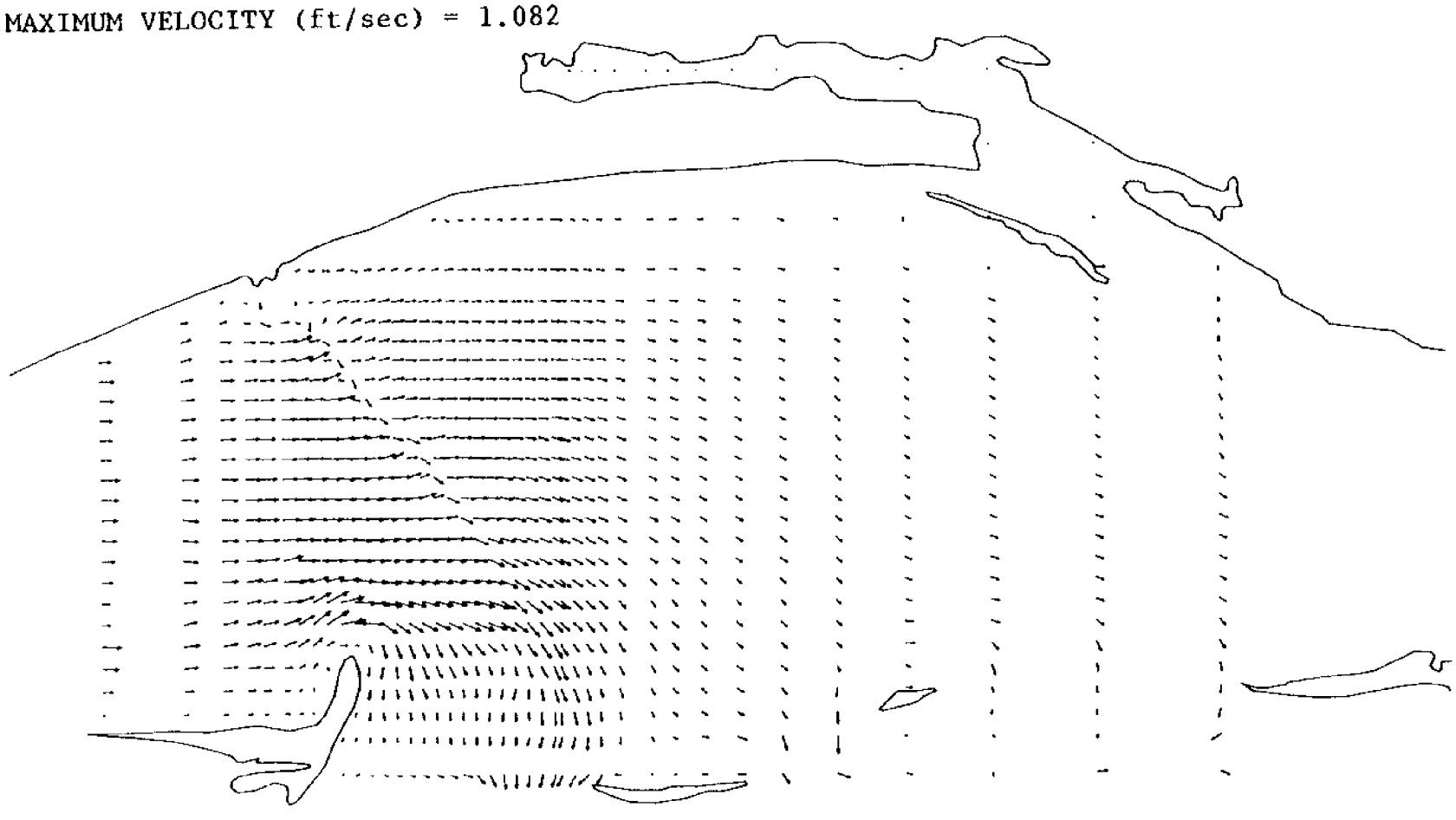

Figure E.11. Circulation Pattern for Existing Conditions at T = 22 Hours

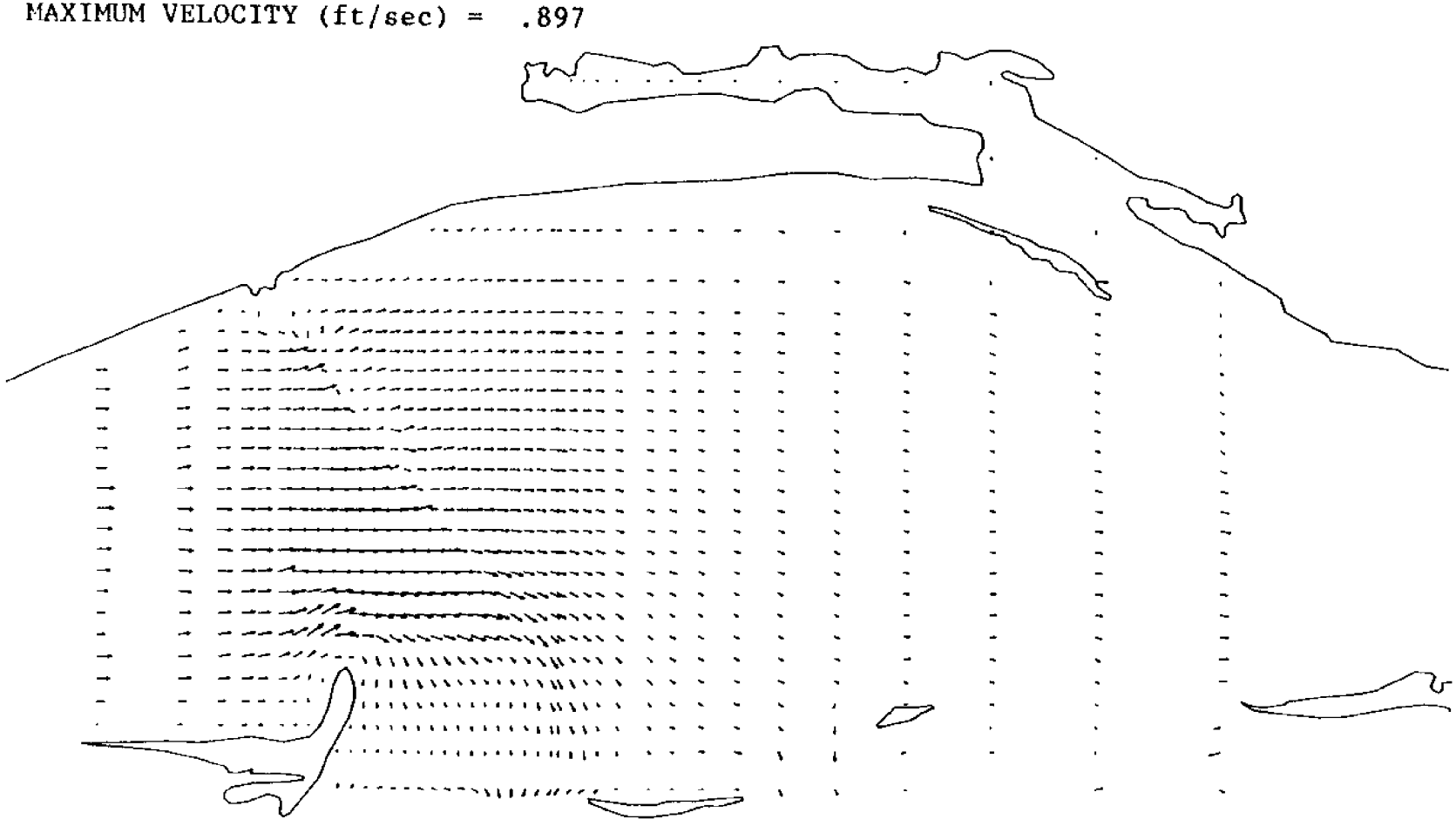

Figure E.12. Circulation Pattern for Existing Conditions at T = 24 Hours

APPENDIX F

General Circulation Patterns
with Channel Deepened to 45 Feet
(9 Knots N-W Wind)

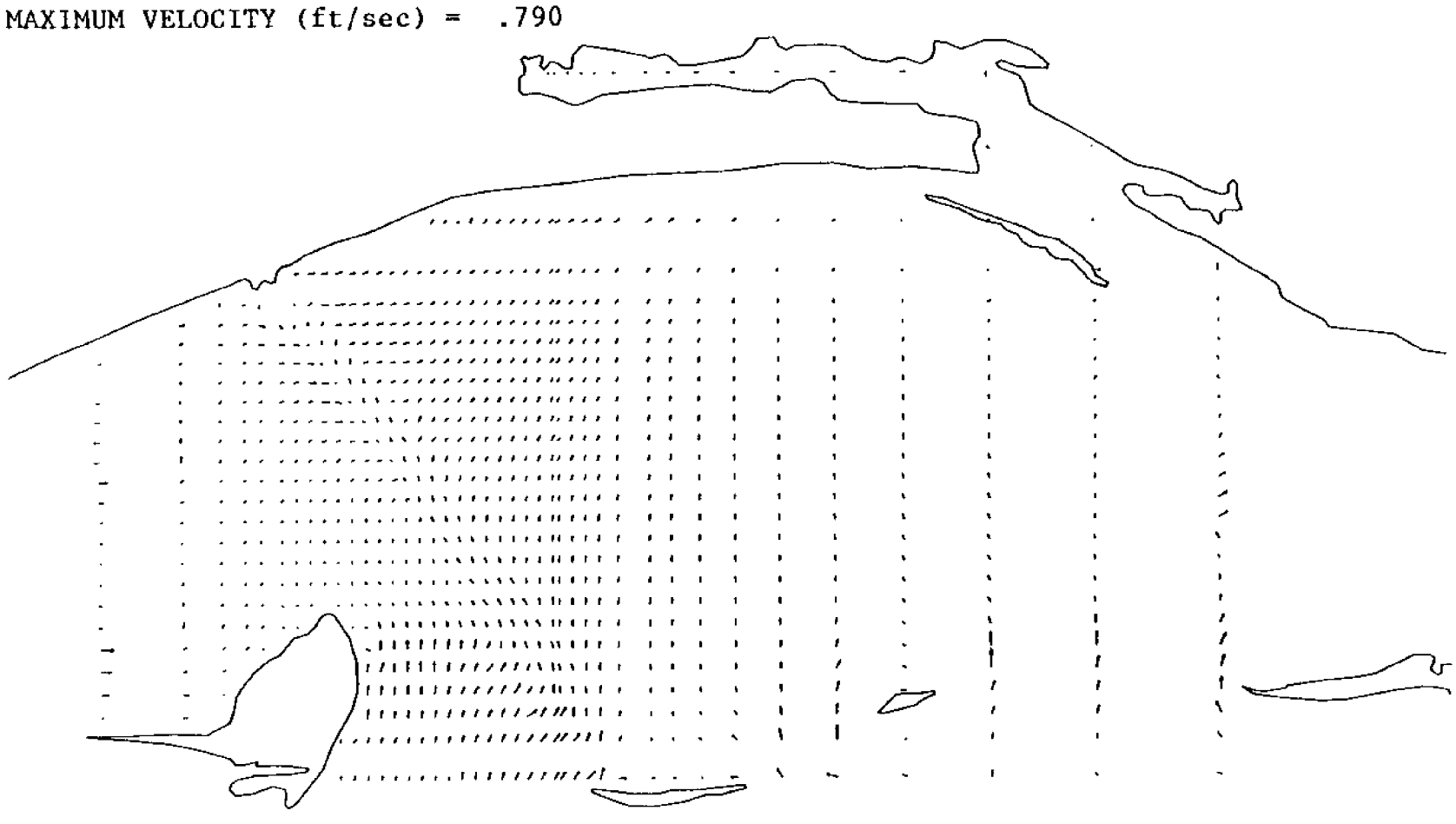

Figure F.1. Circulation Pattern for Channel Deepened to 45 Feet at T = 2 Hours

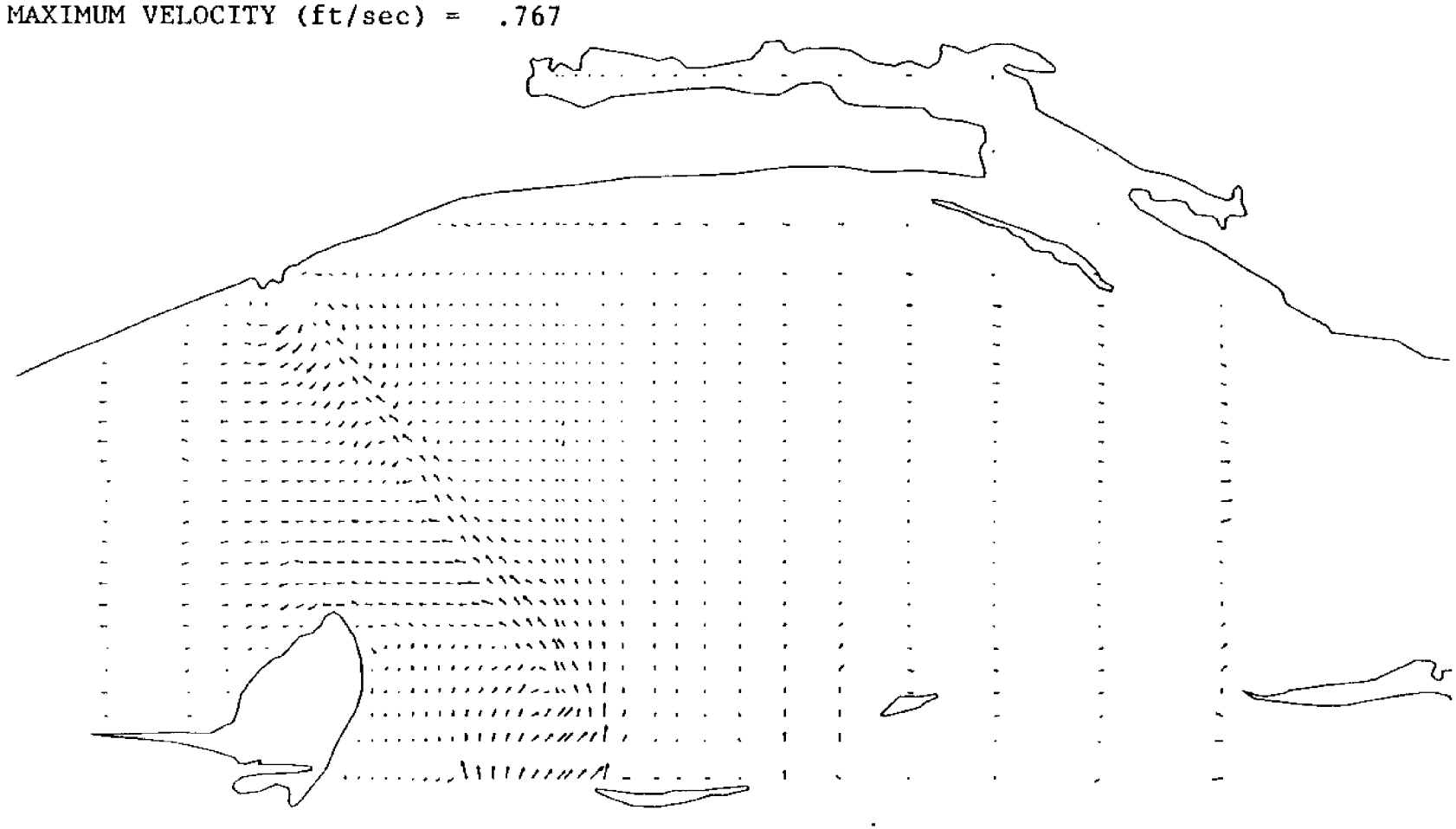

Figure F.2. Circulation Pattern for Channel Deepened to 45 Feet at T = 4 Hours

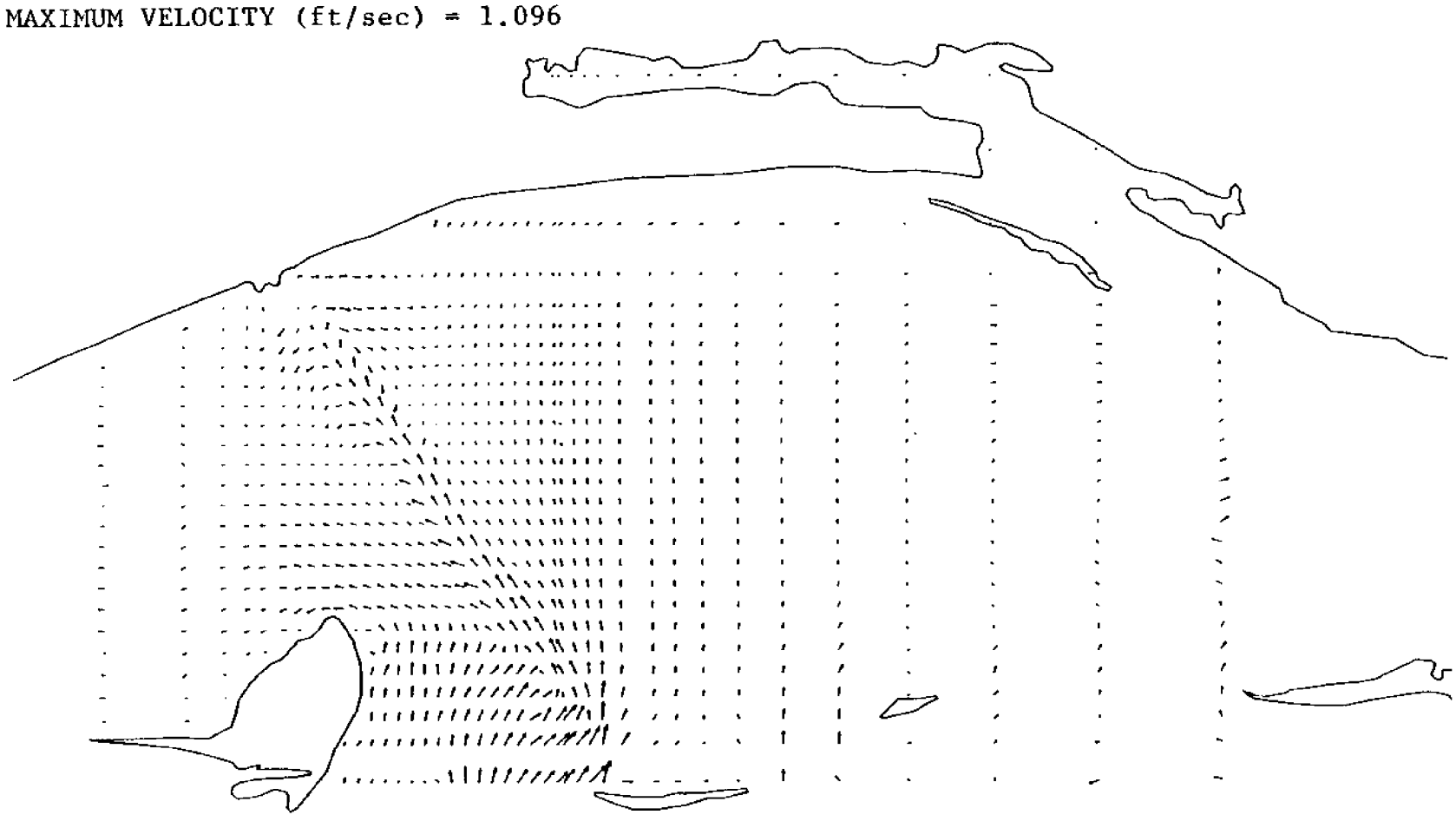

Figure F.3. Circulation Pattern for Channel Deepened to 45 Feet at T = 6 Hours

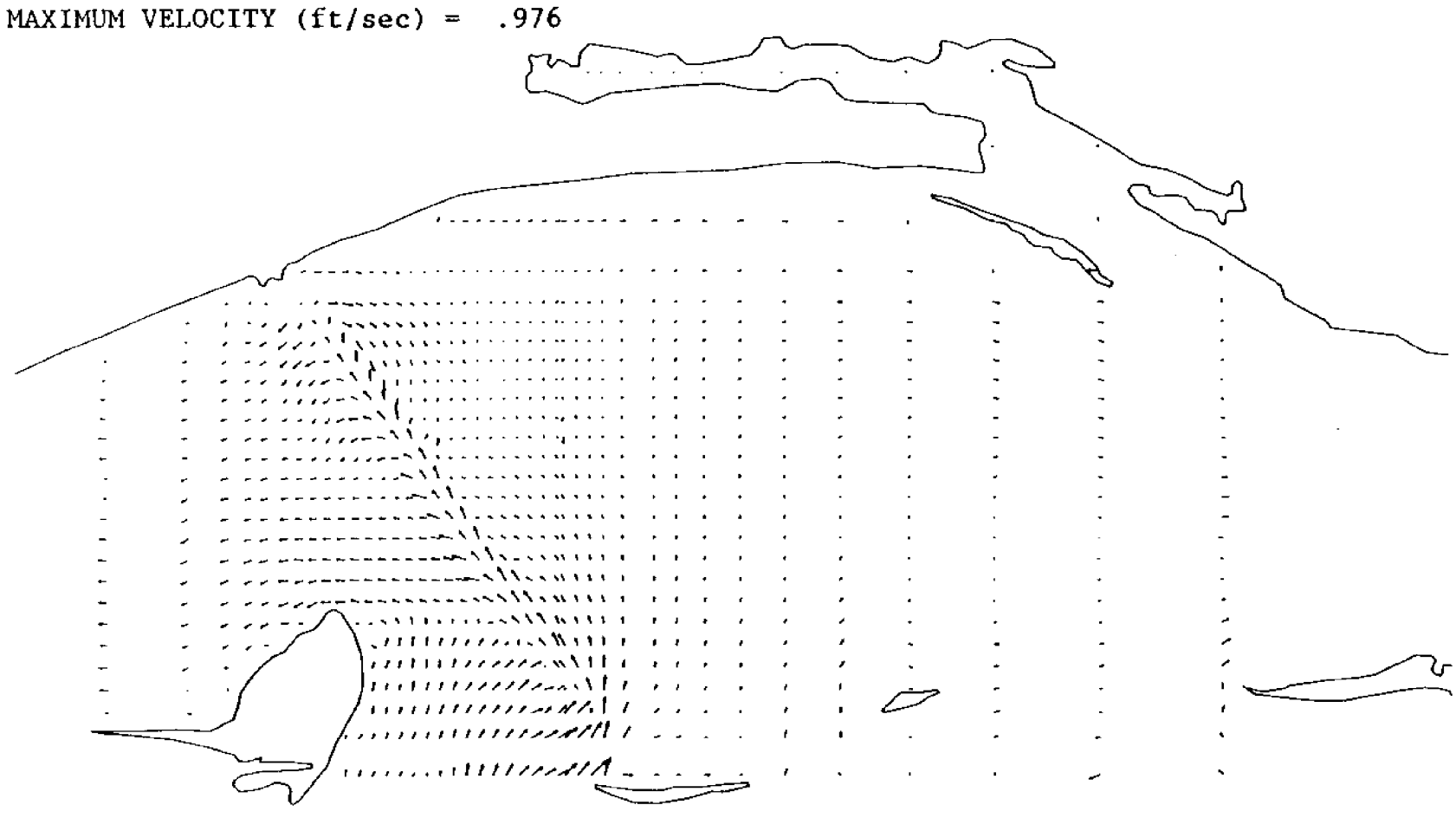

Figure F.4. Circulation Pattern for Channel Deepened to 45 Feet at T = 8 Hours

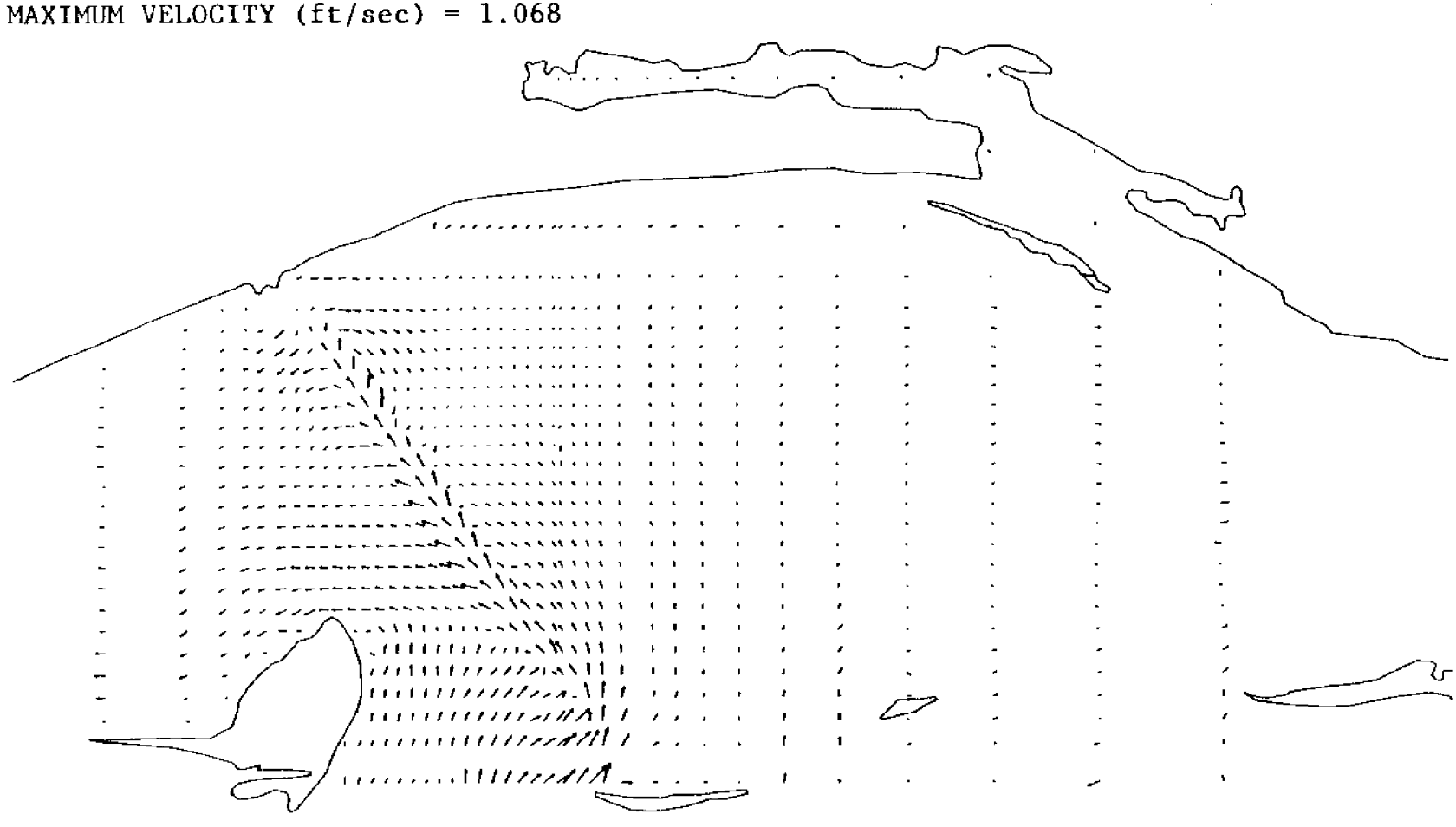

Figure F.5. Circulation Pattern for Channel Deepened to 45 Feet at T = 10 Hours

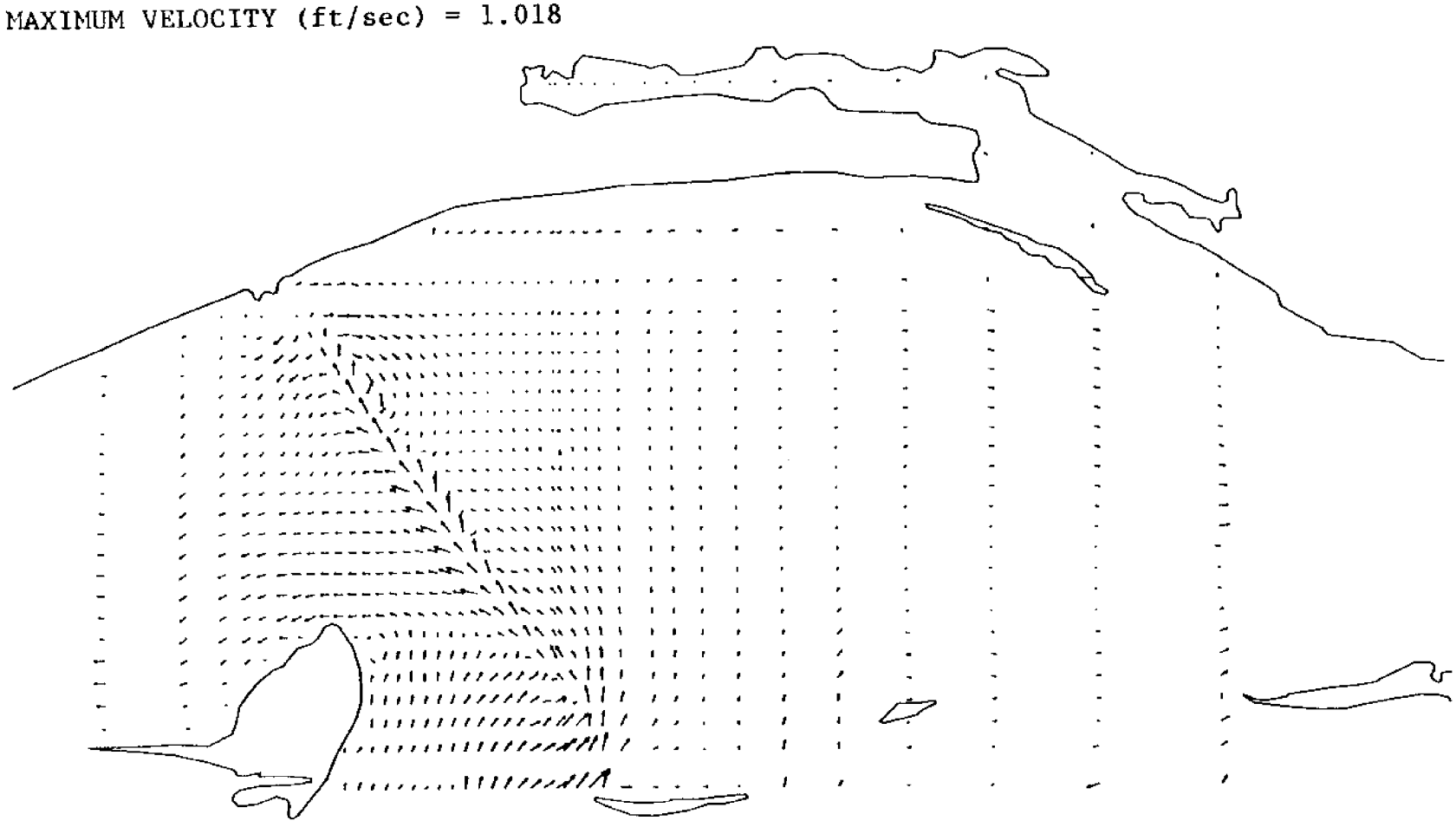

Figure F.6. Circulation Pattern for Channel Deepened to 45 Feet at T = 12 Hours

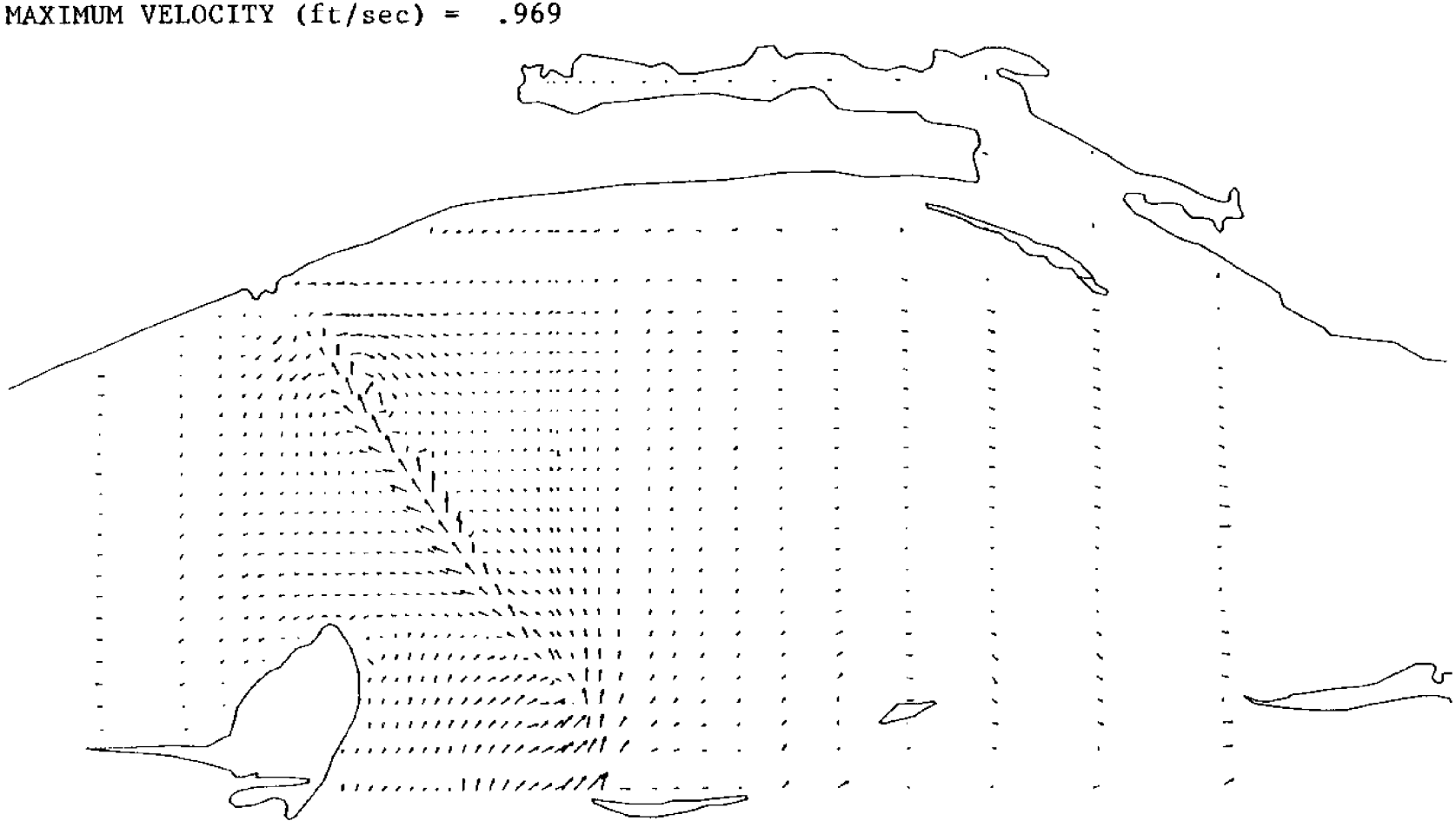

Figure F.7. Circulation Pattern for Channel Deepened to 45 Feet at T = 14 Hours

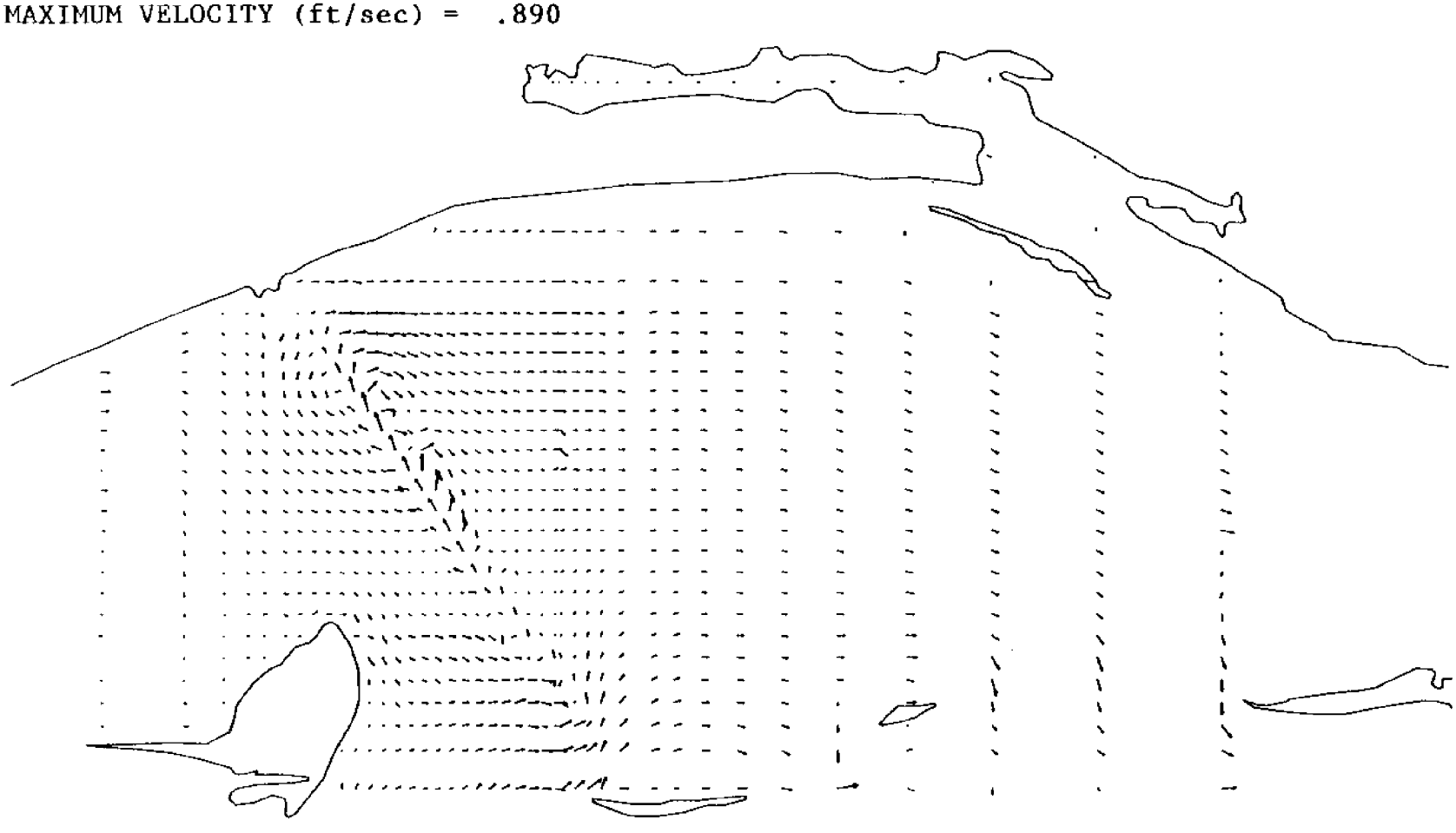

Figure F.8. Circulation Pattern for Channel Deepened to 45 Feet at T = 16 Hours

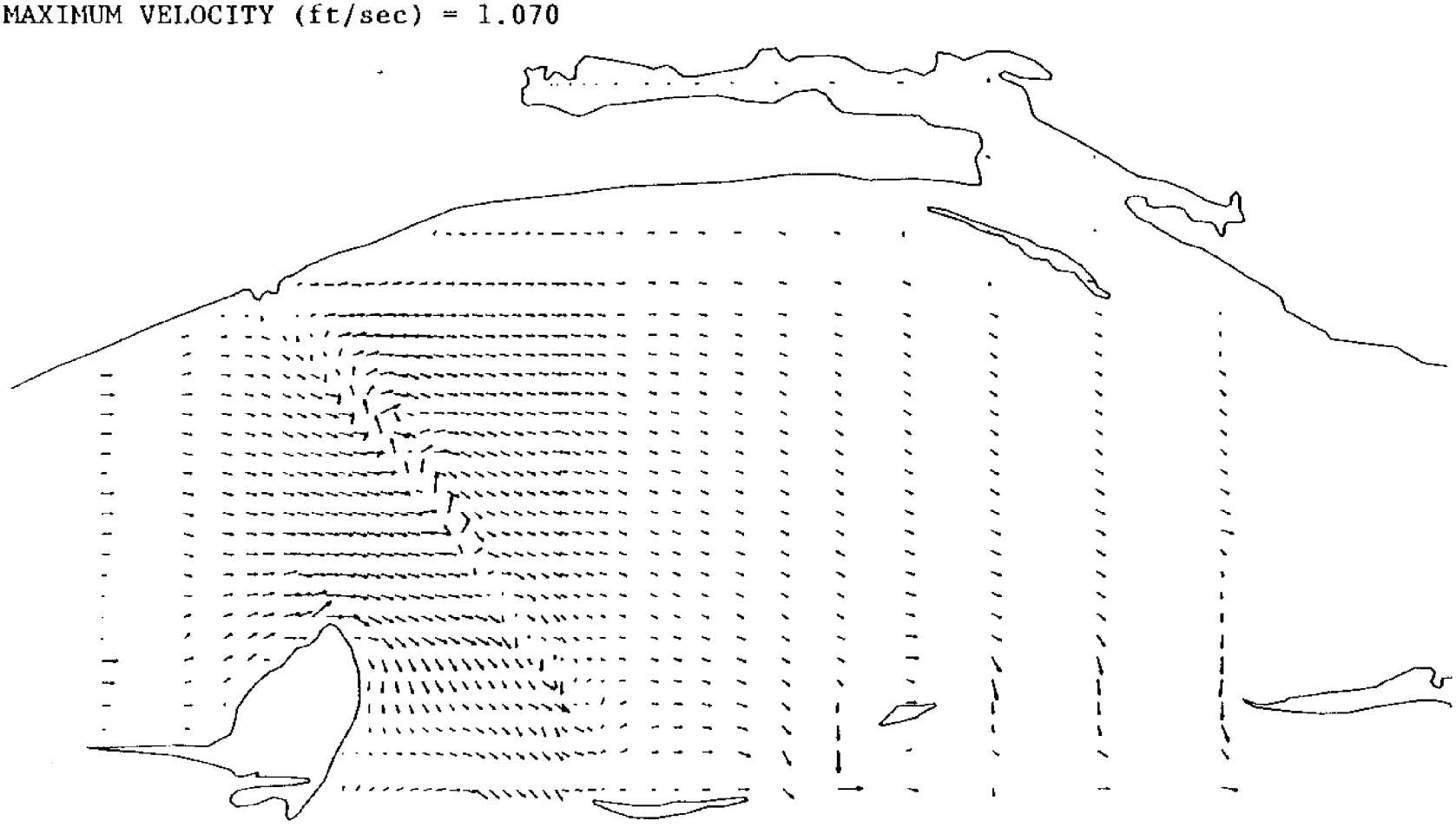

Figure F.9. Circulation Pattern for Channel Deepened to 45 Feet at T = 18 Hours

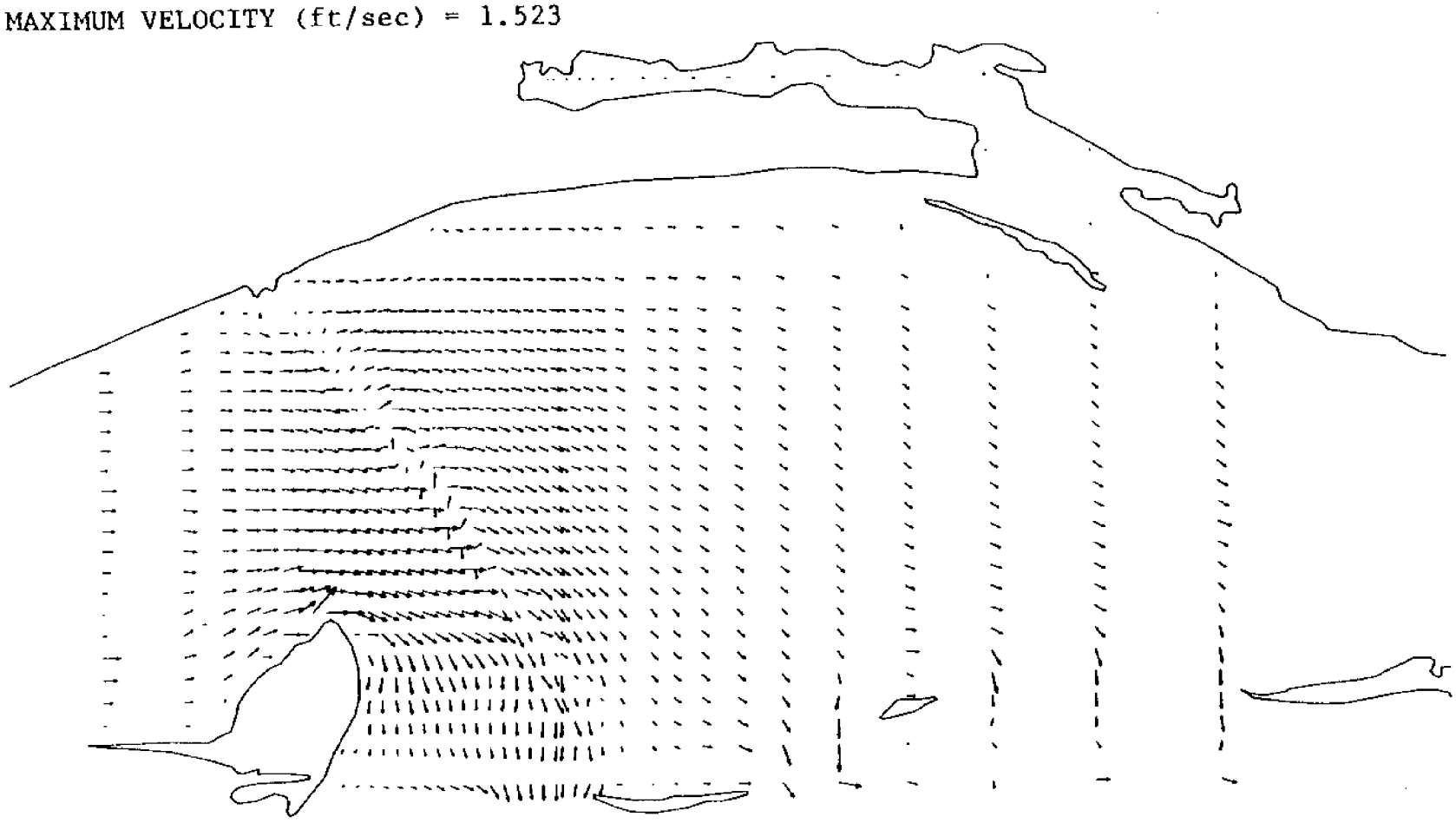

Figure F.10. Circulation Pattern for Channel Deepened to 45 Feet at T = 20 Hours

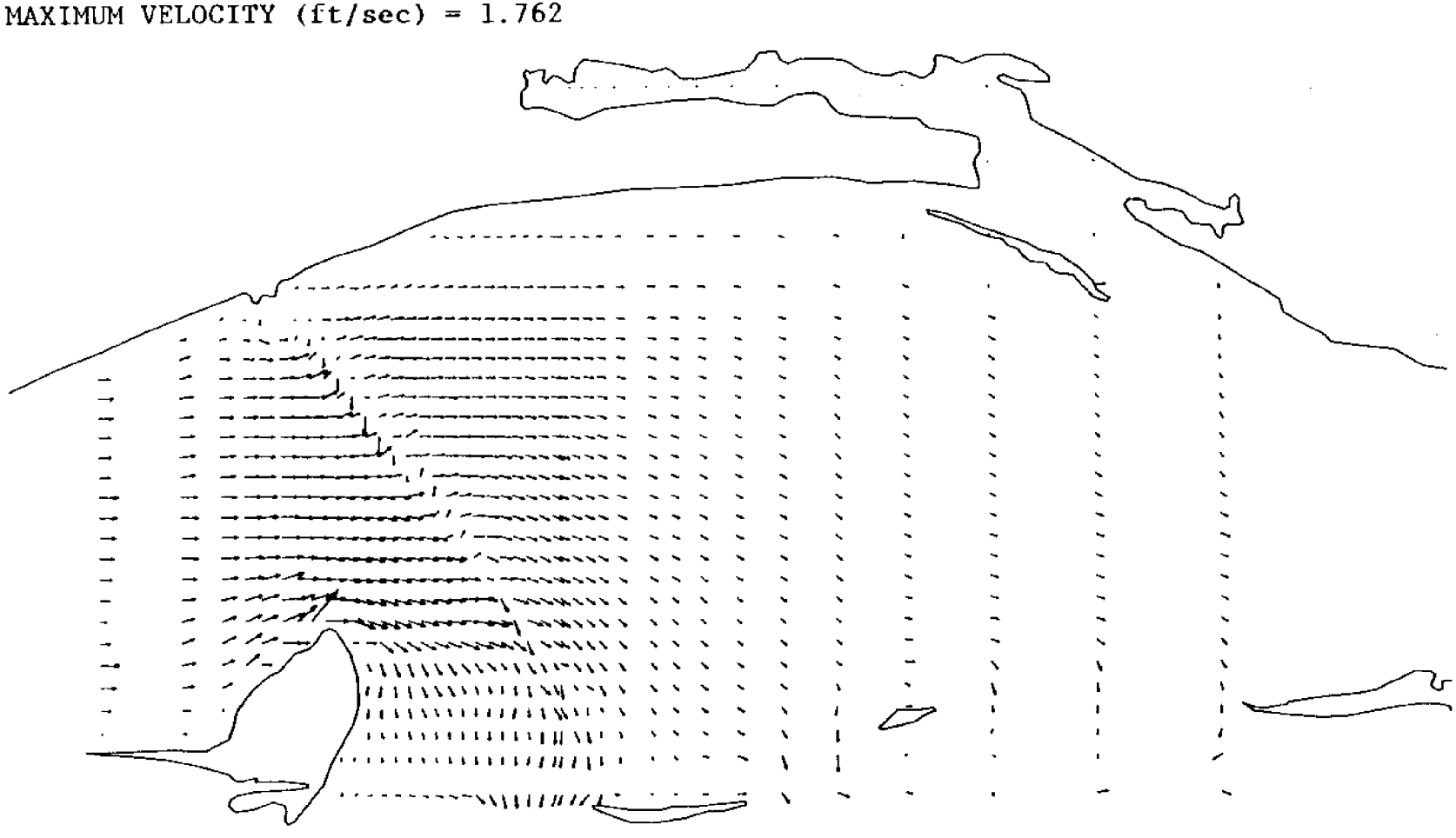

Figure F.11. Circulation Pattern for Channel Deepened to 45 Feet at T = 22 Hours

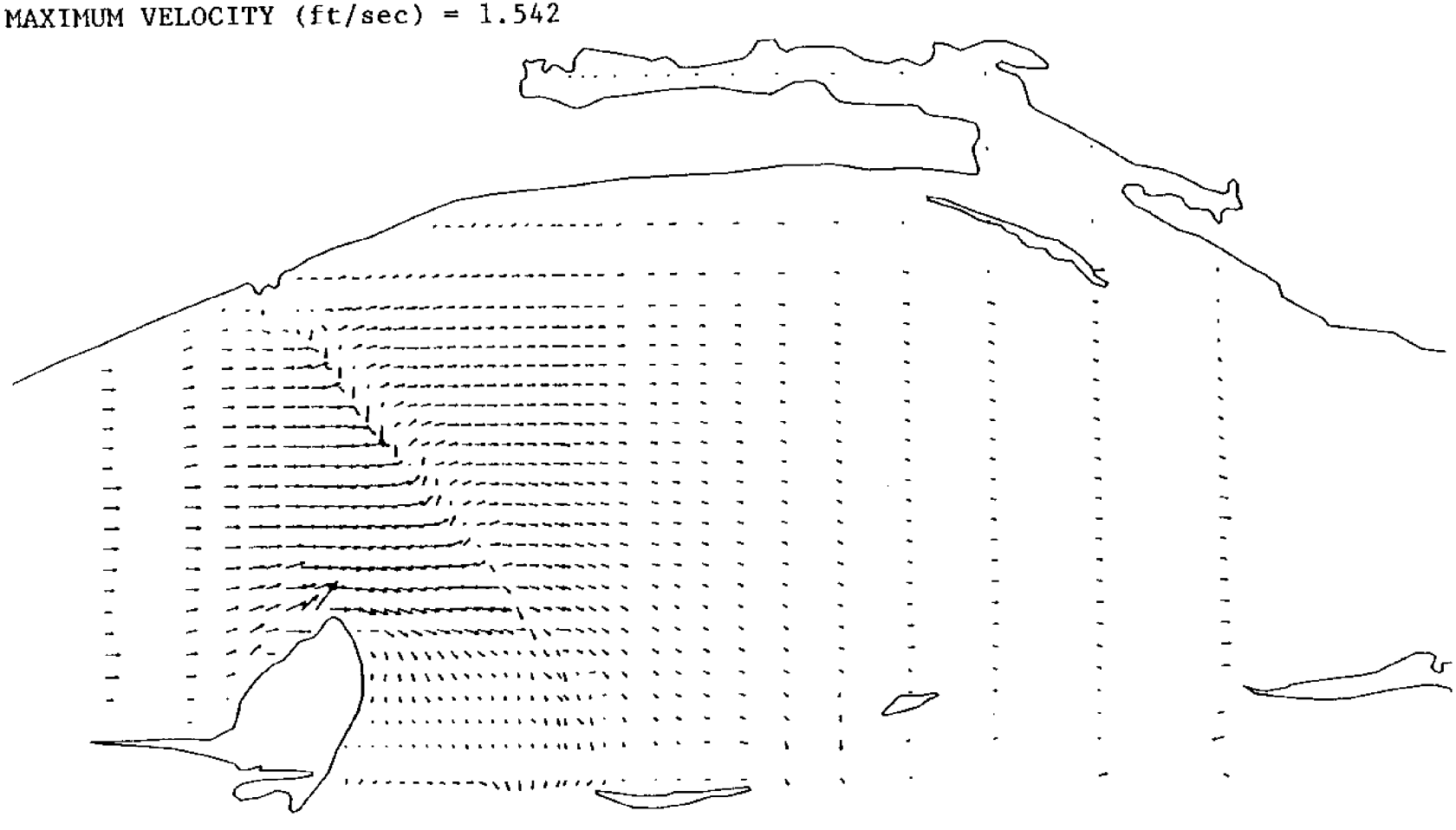

Figure F.12. Circulation Pattern for Channel Deepened to 45 Feet at T = 24 Hours

APPENDIX G

Change in Circulation Patterns
Produced by Deepening Channel to 45 Feet
(9 Knots N-W Wind)

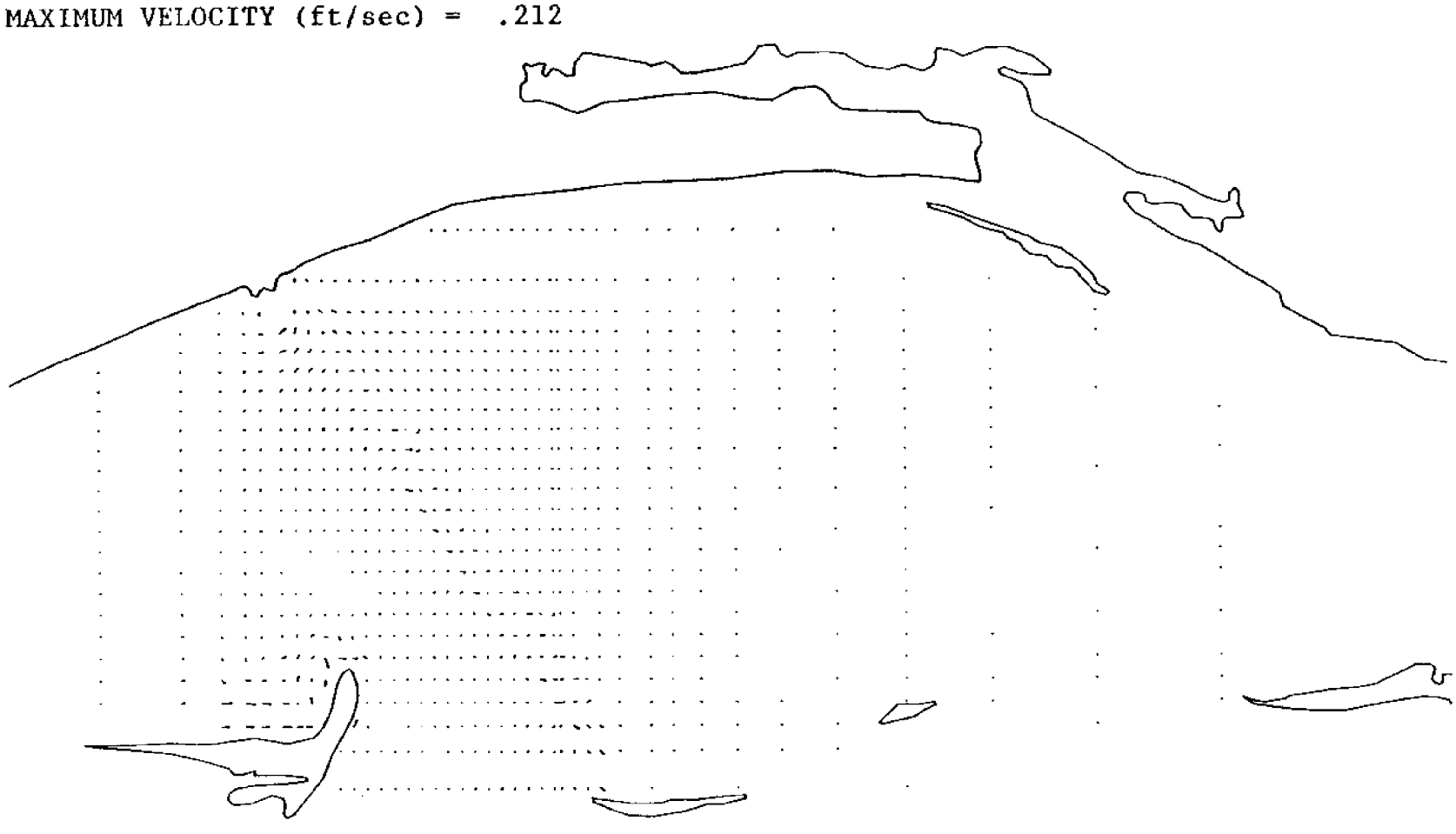

Figure G.1. Change in Circulation Due to 45 Foot Channel at T = 2 Hours

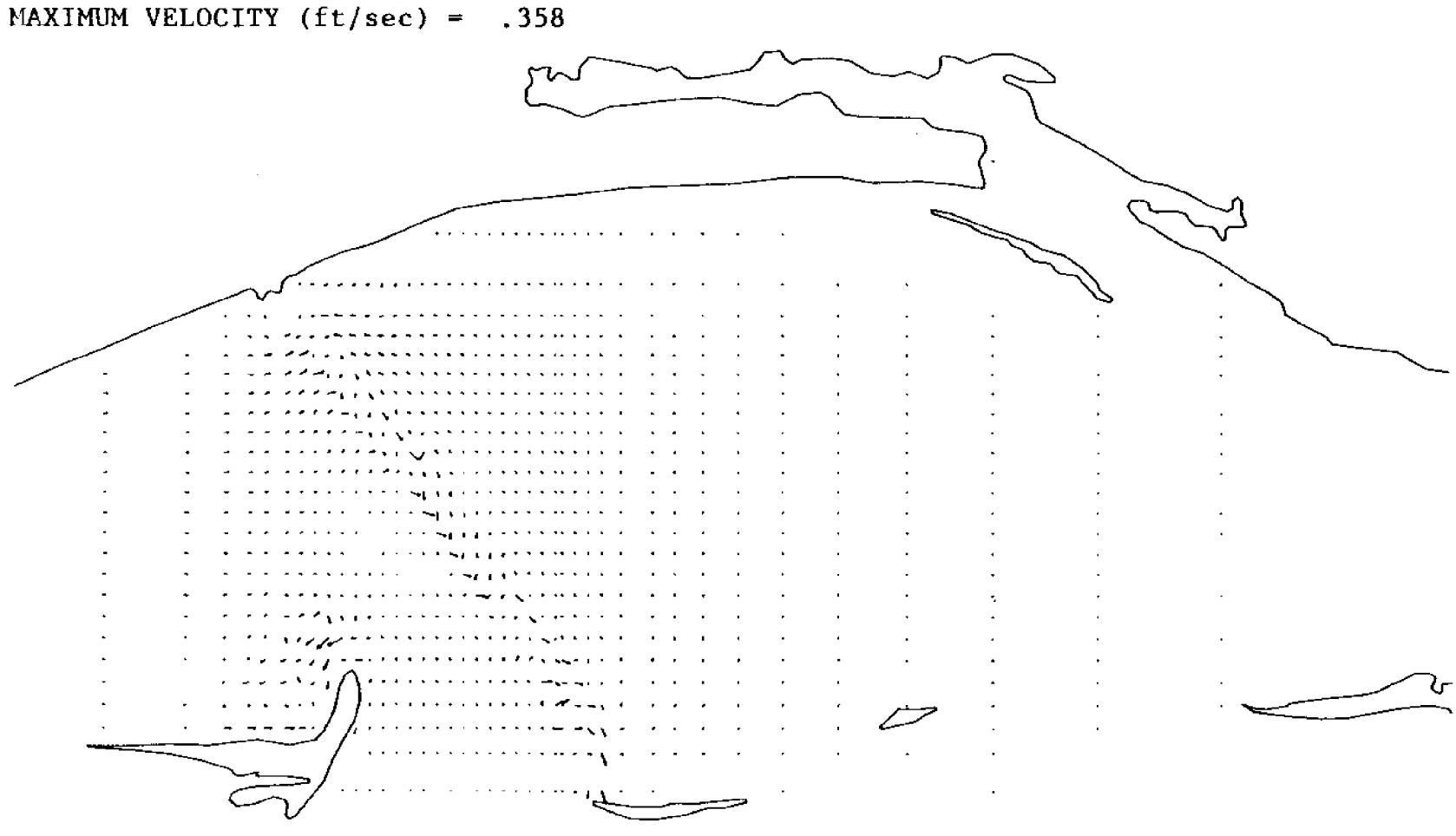

Figure G.2. Change in Circulation Due to 45 Foot Channel at T = 4 Hours

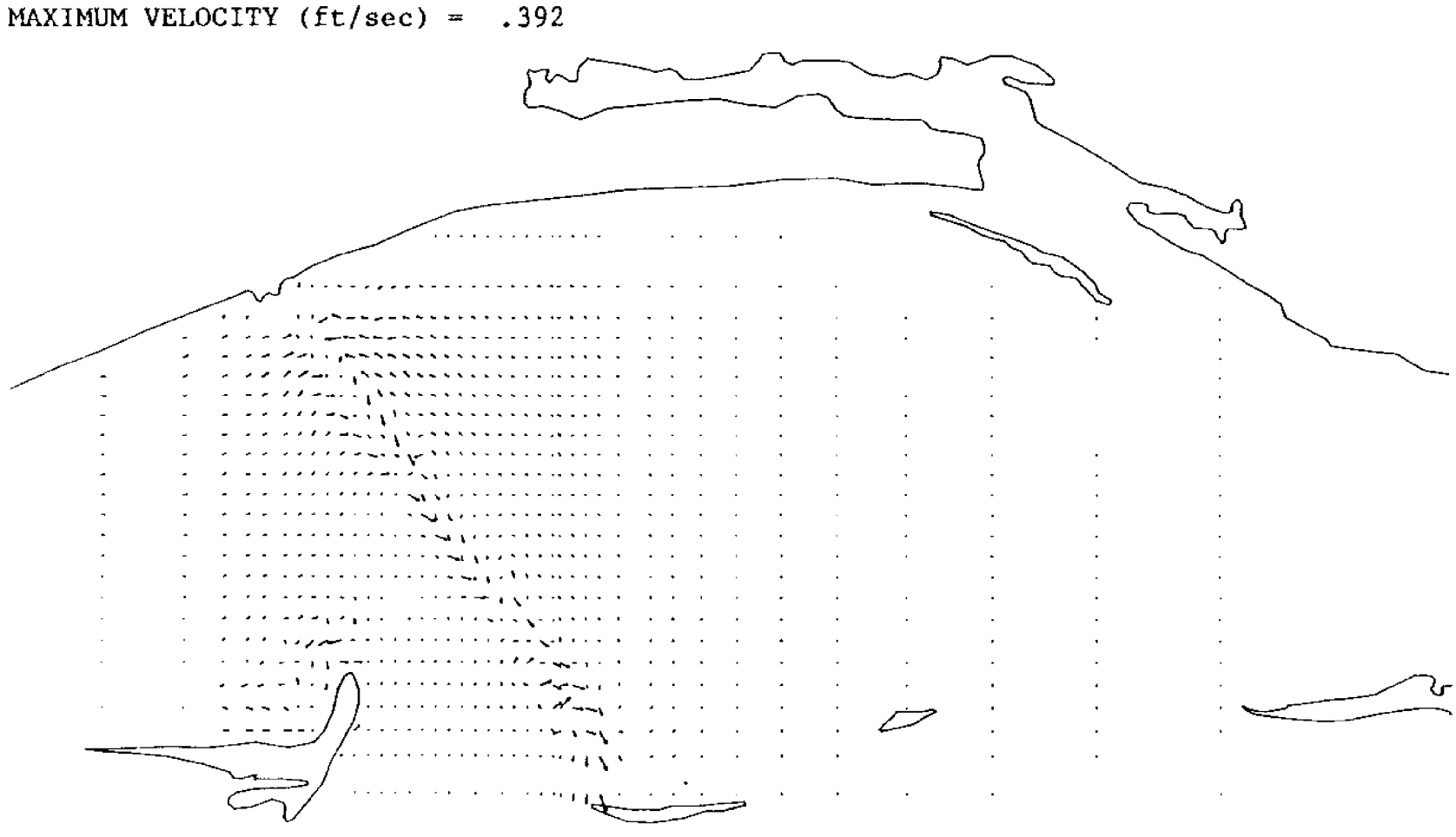

Figure G.3. Change in Circulation Due to 45 Foot Channel at T = 6 Hours

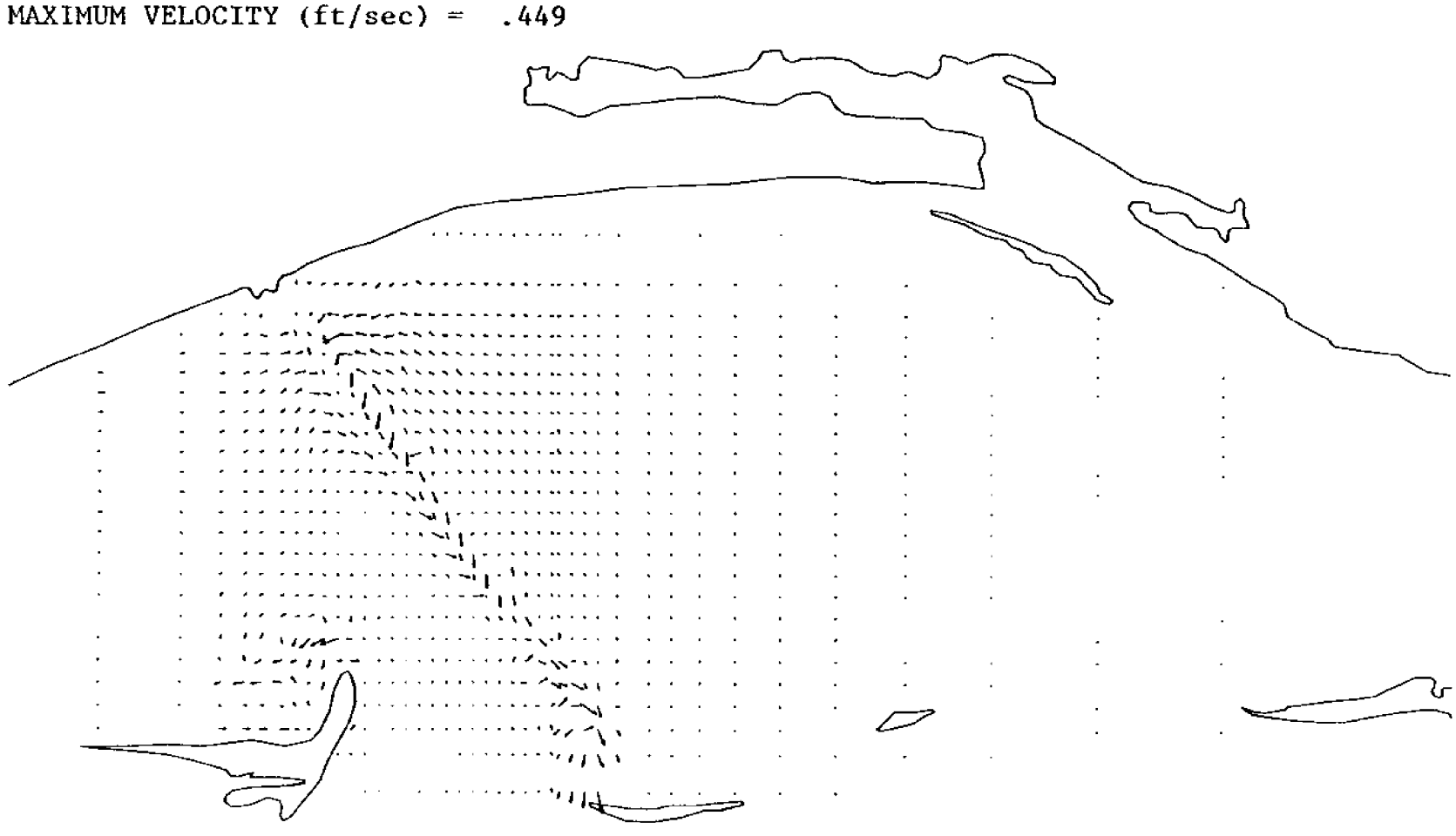

Figure G.4. Change in Circulation Due to 45 Foot Channel at T = 8 Hours

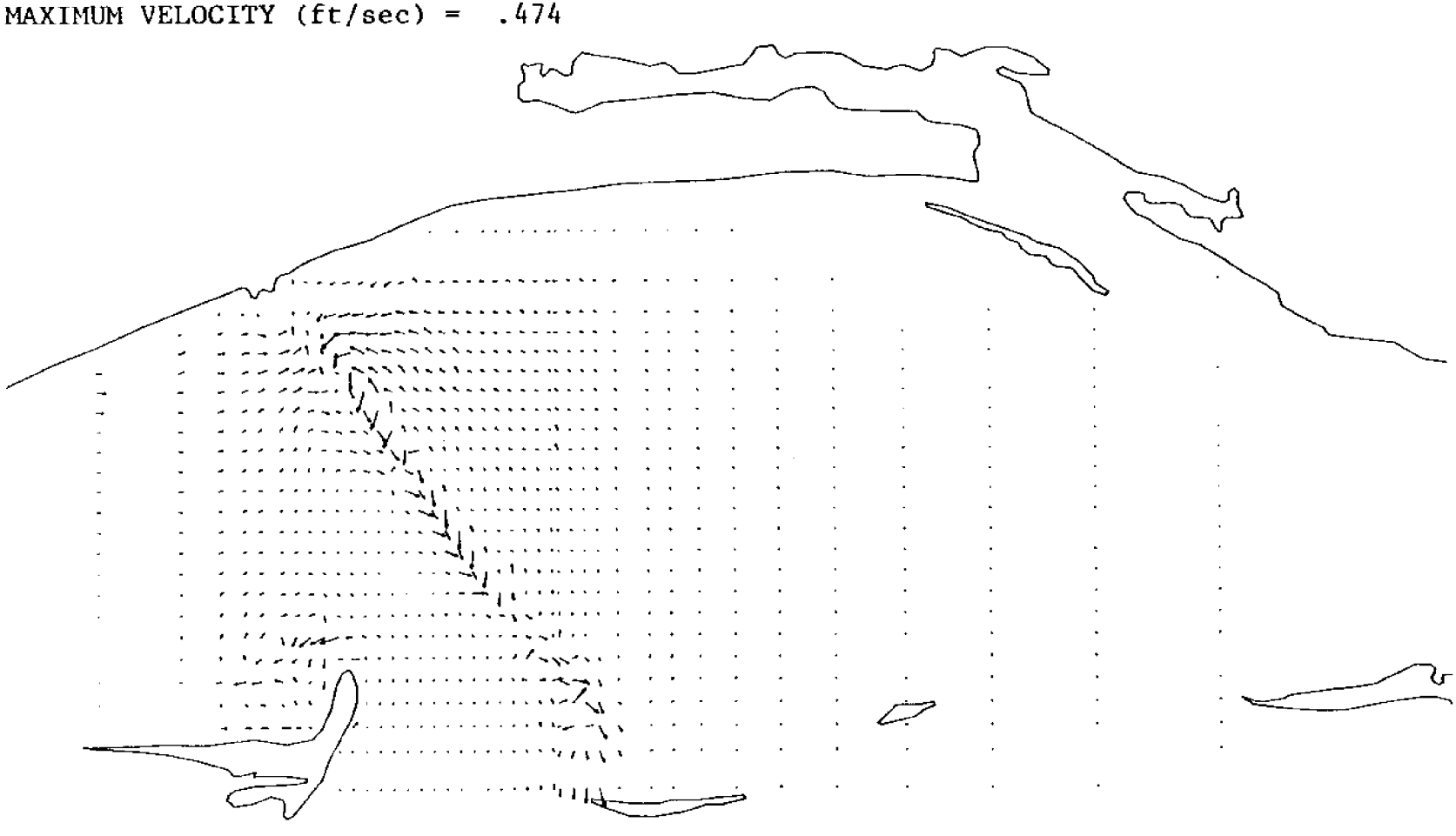

Figure G.5. Change in Circulation Due to 45 Foot Channel at T = 10 Hours

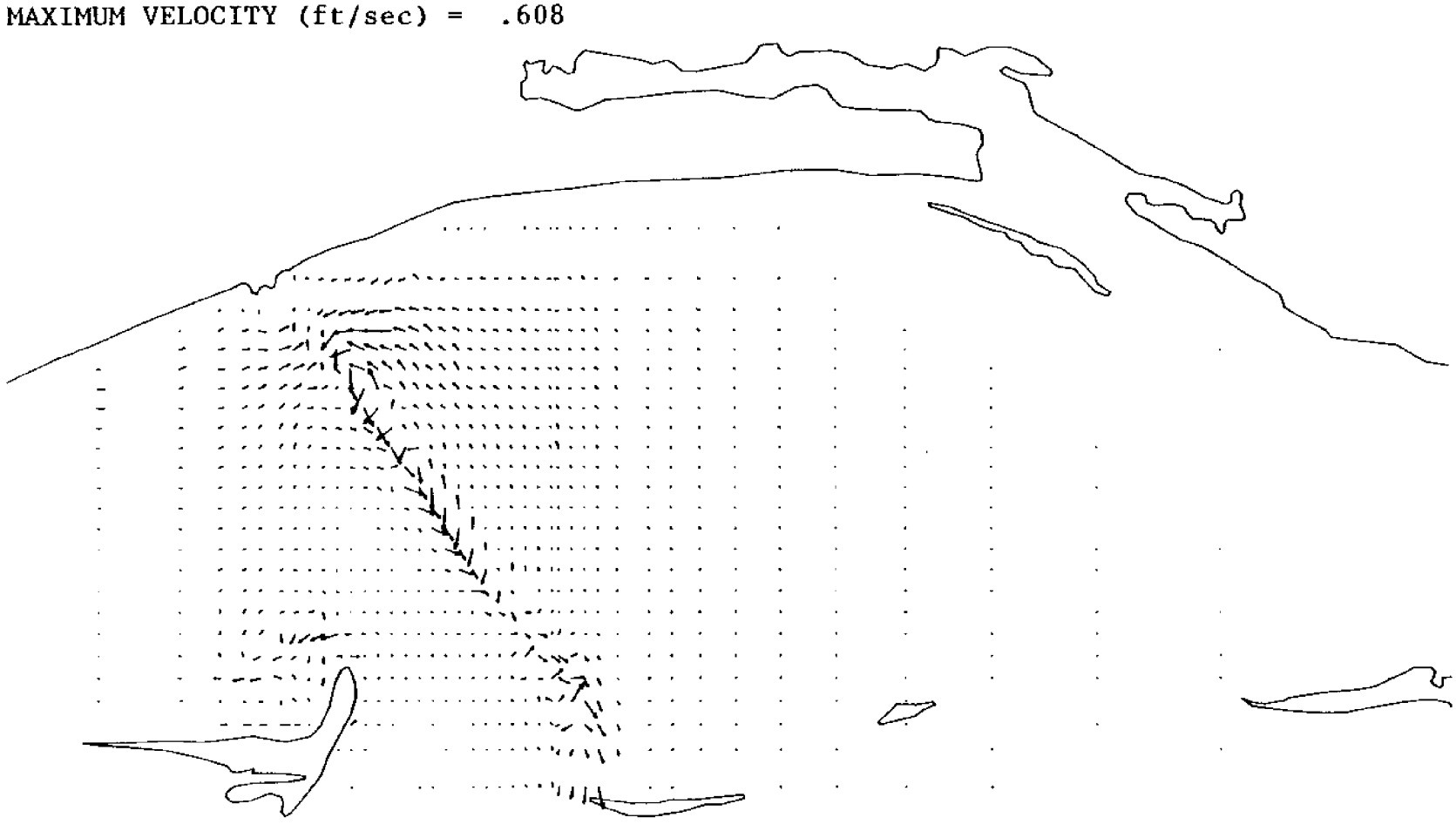

Figure G.6. Change in Circulation Due to 45 Foot Channel at T = 12 Hours

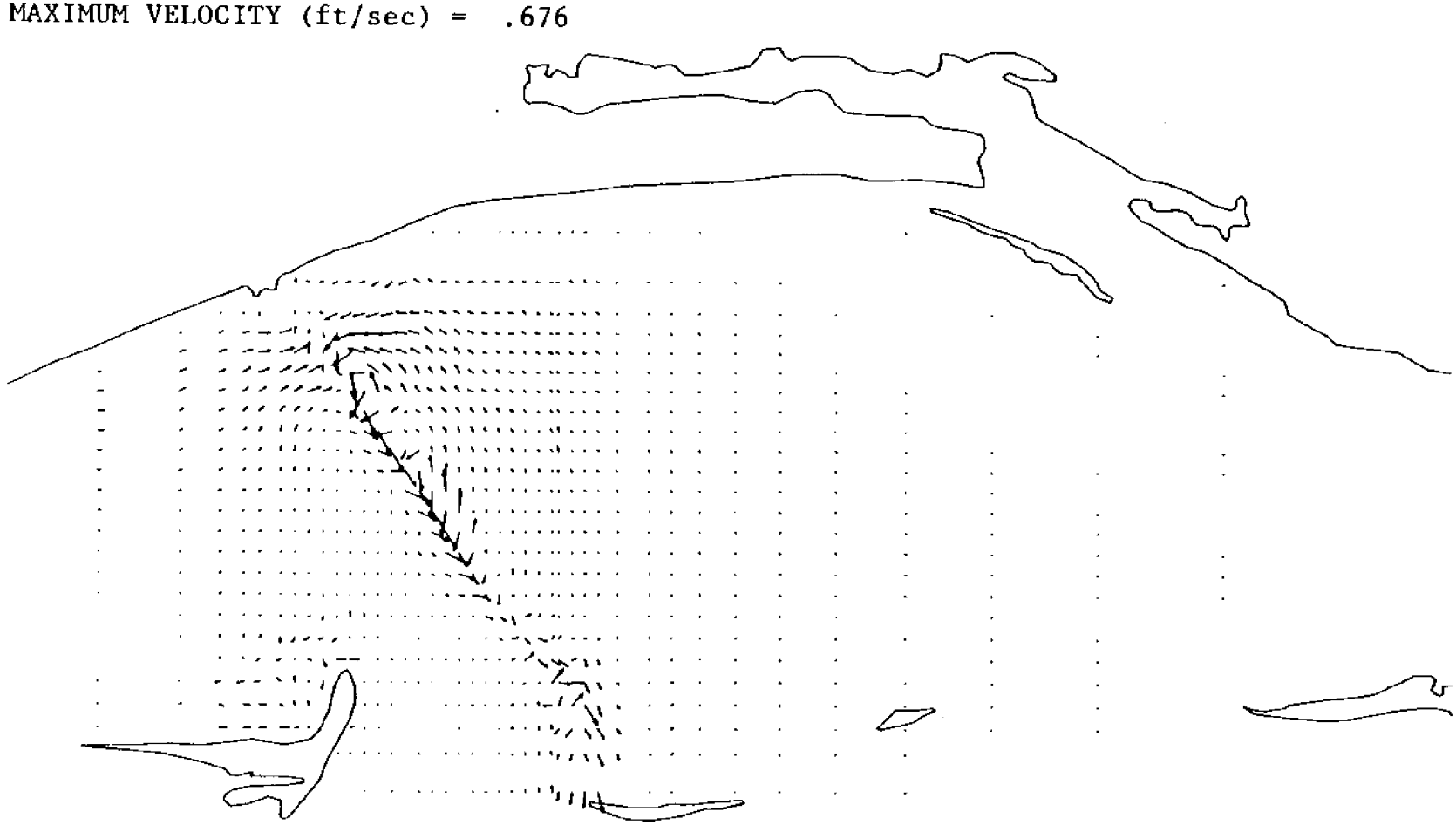

Figure G.7. Change in Circulation Due to 45 Foot Channel at T = 14 Hours

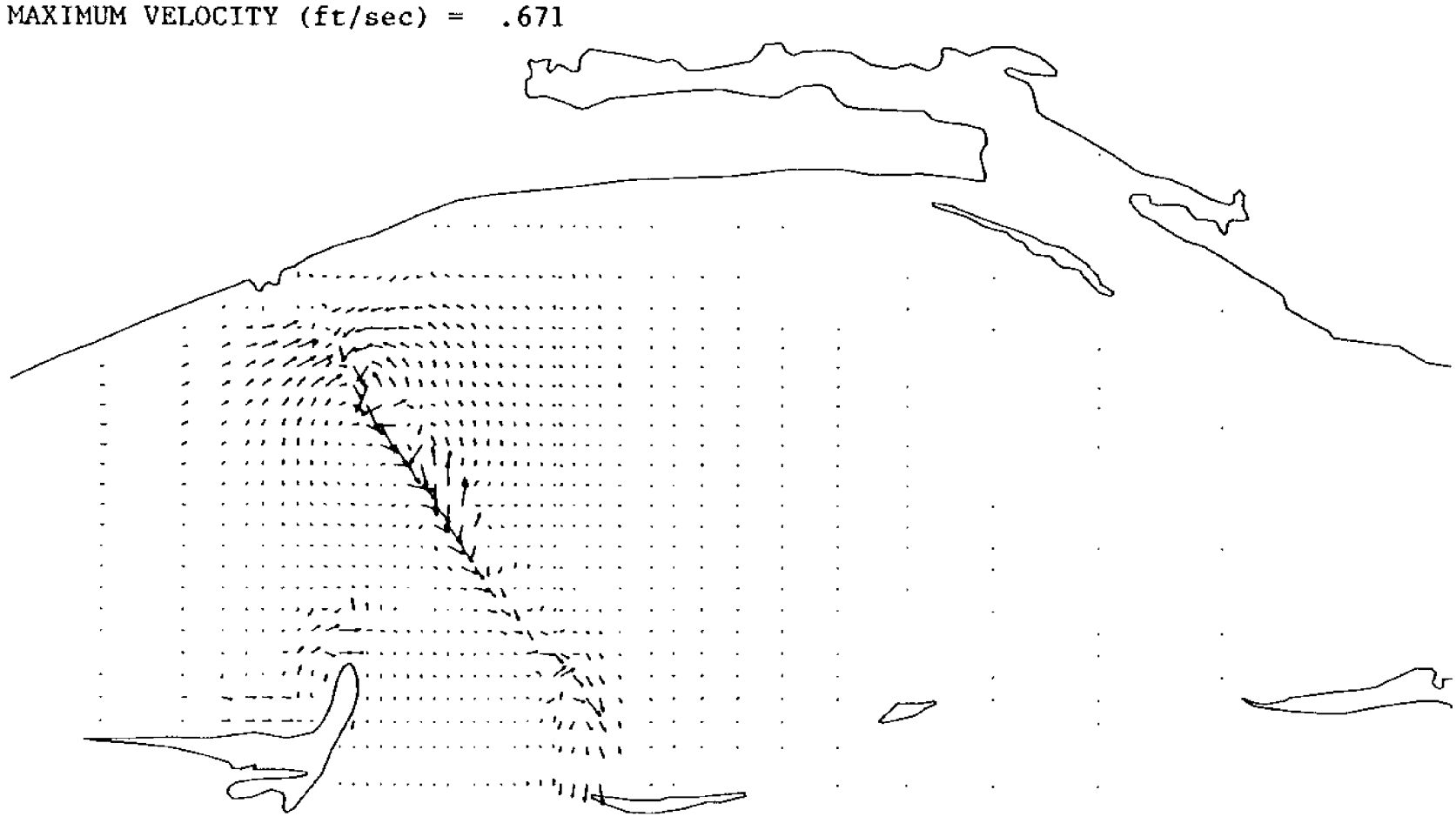

Figure G.8. Change in Circulation Due to 45 Foot Channel at T = 16 Hours

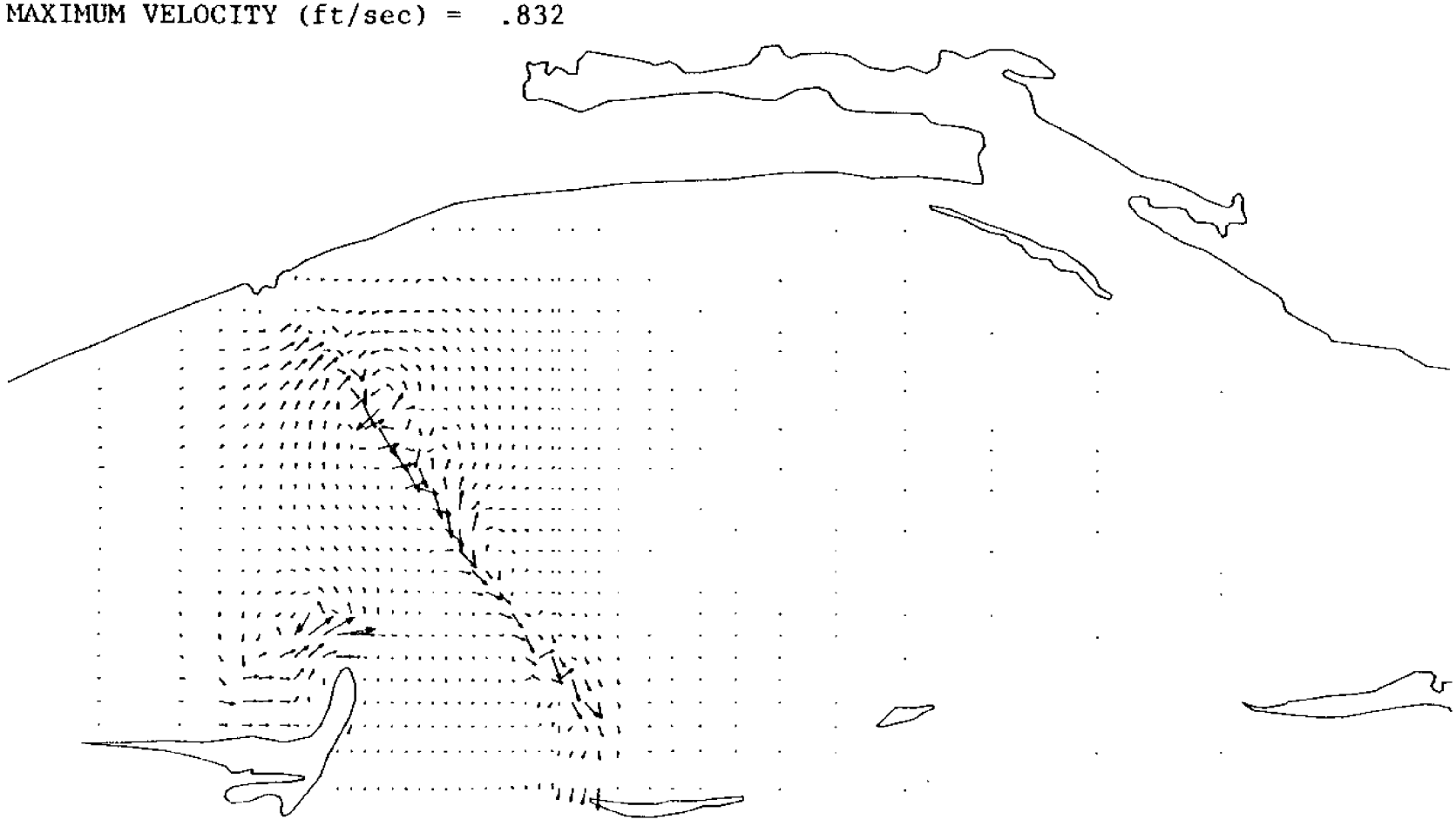

Figure G.9. Change in Circulation Due to 45 Foot Channel at T = 18 Hours

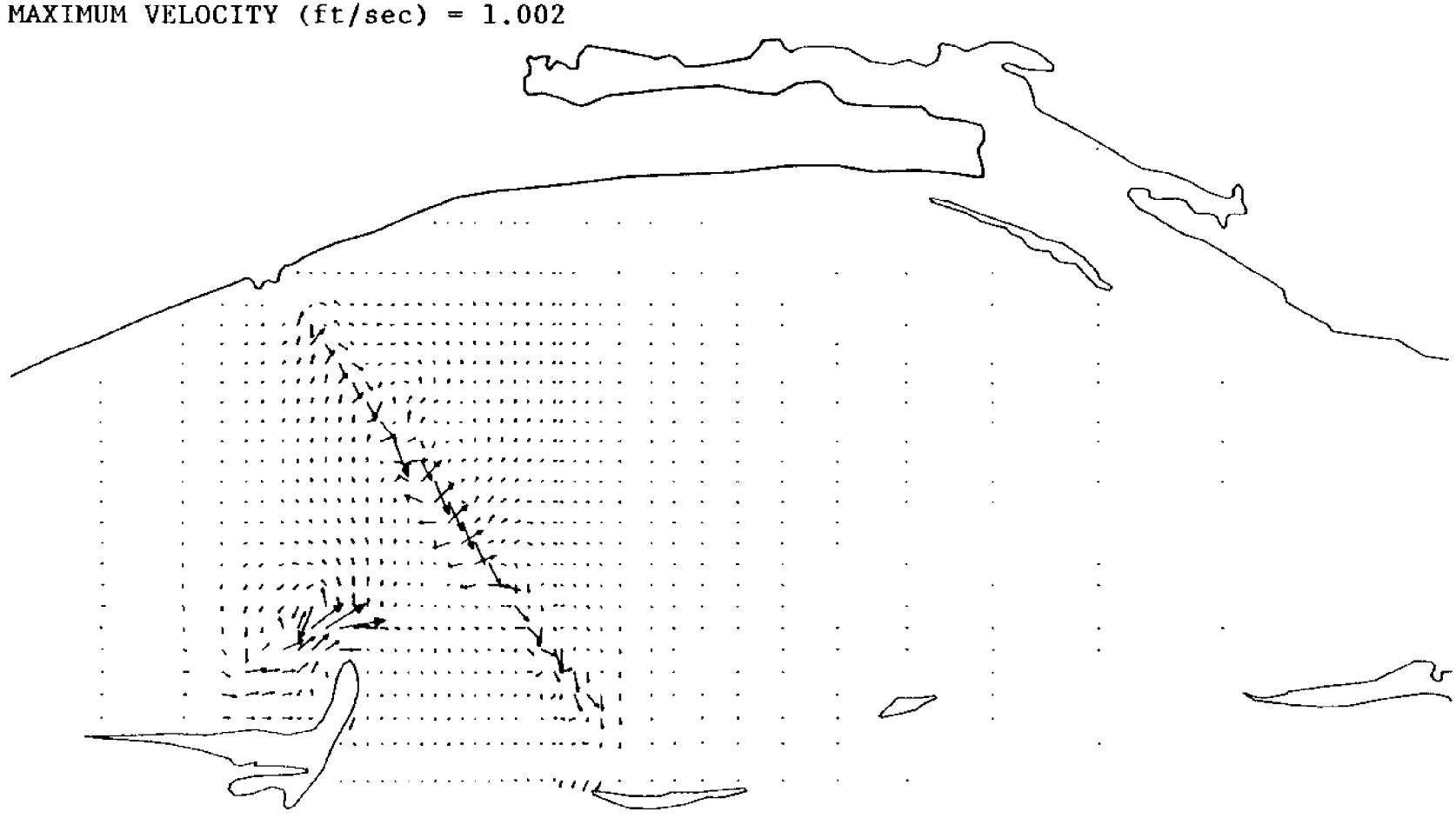

Figure G.10. Change in Circulation Due to 45 Foot Channel at T = 20 Hours

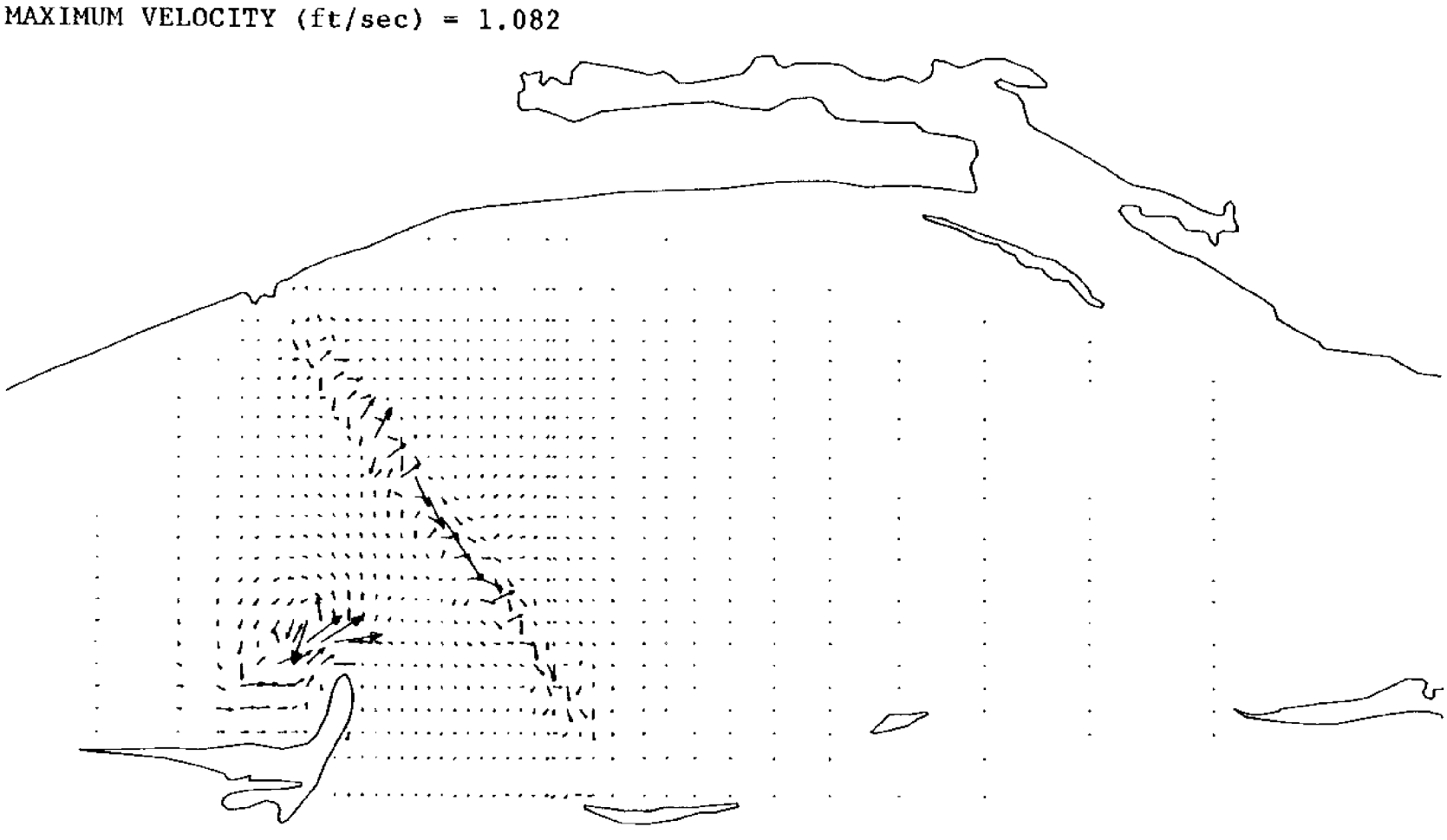

Figure G.11. Change in Circulation Due to 45 Foot Channel at T = 22 Hours

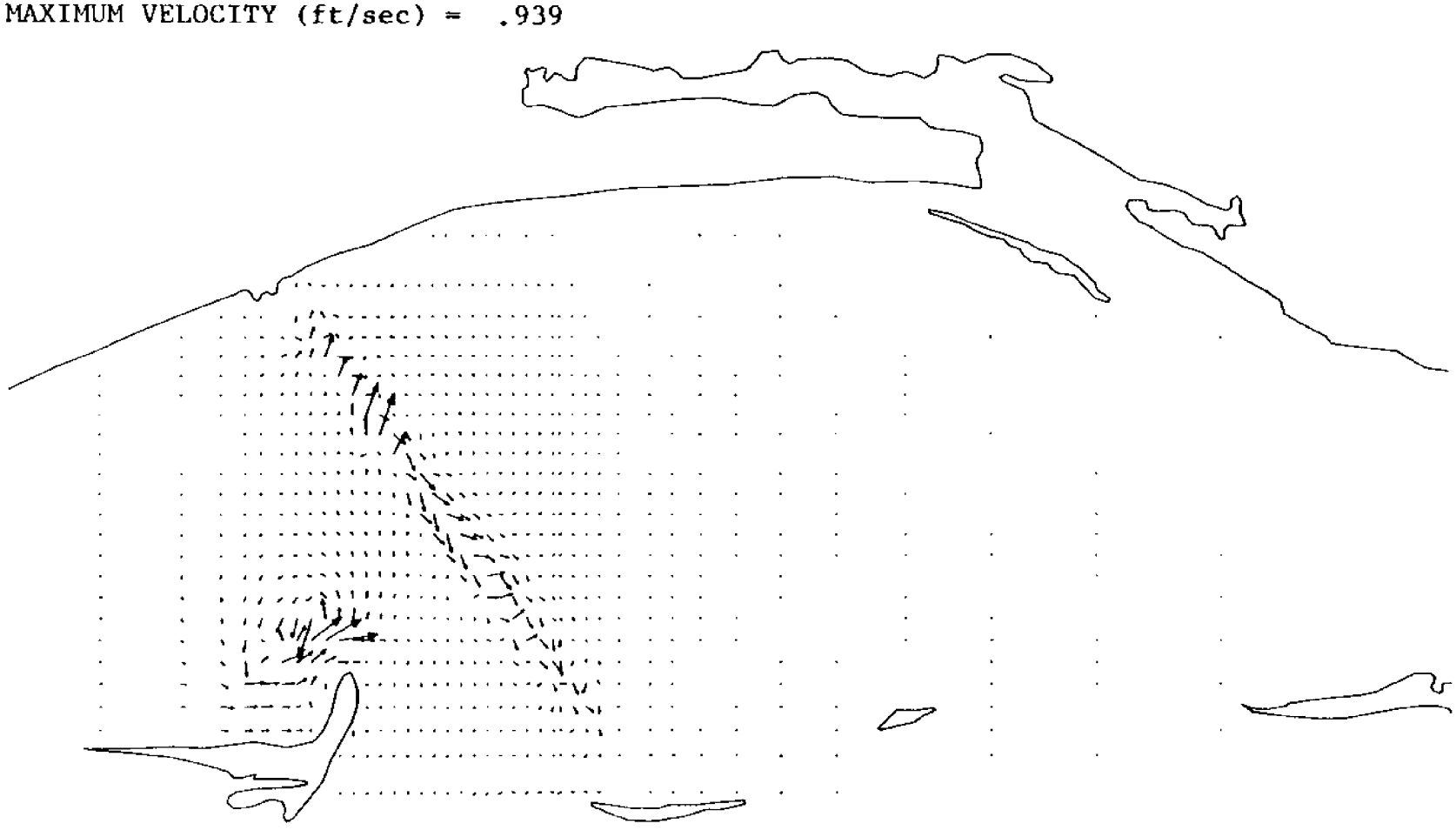

Figure G.12. Change in Circulation Due to 45 Foot Channel at T = 24 Hours